Nonlinear kinetic transport in high-temperature plasmas due to turbulence and vortices in phase-space

Alejandro Guillevic

Nonlinear kinetic transport in high-temperature plasmas due to turbulence and vortices in phase-space

THÈSE

présentée et soutenue publiquement le 4 décembre 2023

pour l'obtention du

Doctorat de l'Université de Lorraine

Spécialité: Physique des plasmas

par

Alejandro Guillevic

Composition du jury

Rapporteurs :	M. Raul Sanchez	Professeur, Department of Physics, University Carlos III of Madrid
	M. Giovanni Manfredi	Directeur de Recherche CNRS, IPCMS, Université de Strasbourg
Examinateurs :	M. Nicolas Dubuit	Maitre-de-Conférences, PIIM, Aix-Marseille Université
	M. Thierry Belmonte	Directeur de Recherche CNRS, IJL, Université de Lorraine
Directeur :	M. Maxime Lesur	Maitre-de-Conférences HDR, IJL, Université de Lorraine

Institut Jean Lamour | UMR CNRS 7198, Nancy, France, Université de Lorraine

Contents

Abstract

Nonlinear transport in high-temperature plasmas due to turbulence and phase-space vortices is investigated through numerical simulations and theory. In this work, we investigate the diffusion of charged particles due to the presence of a prescribed turbulent electric field (Langmuir and ion-acoustic waves with random phases), the diffusion due to phase-space vortices in a turbulent background, and the dynamics of solitary phase-space vortex. In this work, two codes were used, one for test particle trajectories named PERKS used for the diffusion studies, and a second kinetic, Vlasov-Poison solver named COBBLES used to perform the analysis of phase-space vortices. Turbulent diffusion at a low Kubo number, defined as the ratio between the autocorrelation time and characteristic trapped bounce time of the electric field $K = \tau_0/\tau_b$, is correctly predicted by quasi-linear theory, including resonance broadening. However, for large Kubo numbers, a new regime is reached where the diffusion coefficient increases and scales as a power law $E^{3/2}$, which is explained by a random-walk diffusion of the centers of trapped-particle trajectories. In the presence of phase-space vortices, diffusion is divided into two regimes: The first one is where diffusion is dominant, particles experience random-walk trajectories, and diffusion is predicted as if no structure is present in the plasma. In the second case, where structures are dominant over turbulence, particle dynamics is that of trapped-particle trajectories, and diffusion is predicted by the one generated due to the structure. Finally, the dynamic of solitary Schamel phase-space vortices is investigated. Limits and discrepancies of the analytical theory with respect to numerical simulations are discussed, particularly the large impact the ion-distribution function and small variations of distribution gradients have over the dynamics of electron vortices.

Keywords: Diffusion, Phase-Space, Turbulence, Vortex, Fusion.

Résumé

Le transport non linéaire dans les plasmas à haute température dû à la turbulence et aux vortex de l'espace des phases est étudié par des simulations numériques et par la théorie. Dans ce travail, nous étudions la diffusion de particules chargées due à la présence d'un champ électrique turbulent prescrit (ondes de Langmuir et ondes ioniques-acoustiques avec phases aléatoires), la diffusion due aux vortex de l'espace des phases dans un fond turbulent, et la dynamique des vortex solitaires de l'espace des phases. Dans ce travail, deux codes ont été utilisés, l'un pour les trajectoires des

particules test appelé PERKS utilisé pour les études de diffusion, et un second solveur cinétique de Vlasov-Poison appelé COBBLES utilisé pour effectuer l'analyse des tourbillons de l'espace des phases. La diffusion turbulente à un faible nombre de Kubo, défini comme le rapport entre le temps d'autocorrélation et le temps de rebond caractéristique du champ électrique $K = \tau_0/\tau_b$, est correctement prédite par la théorie quasi-linéaire, y compris l'élargissement par résonance. Cependant, pour de grands nombres de Kubo, un nouveau régime est atteint où le coefficient de diffusion augmente et s'échelonne comme une loi de puissance $E^{3/2}$, ce qui s'explique par une diffusion par marche aléatoire des centres des trajectoires des particules piégées. En présence de tourbillons dans l'espace des phases, la diffusion est divisée en deux régimes : Dans le premier cas, la diffusion est dominante, les particules ont des trajectoires de marche aléatoire et la diffusion est prédite comme si aucune structure n'était présente dans le plasma. Dans le second cas, où les structures sont dominantes par rapport à la turbulence, la dynamique des particules est celle des trajectoires de particules piégées, et la diffusion est prédite par celle générée par la structure. Enfin, la dynamique des tourbillons solitaires de Schamel dans l'espace des phases est étudiée. Les limites et les divergences de la théorie analytique par rapport aux simulations numériques sont discutées, en particulier l'impact important de la fonction de distribution des ions et les petites variations des gradients de distribution sur la dynamique des tourbillons d'électrons.

Mots-clés: Diffusion, Espace des phases, Turbulence, Tourbillon, Fusion.

Acknowledgement

The work discussed in this manuscript is the result of my three years of a Ph.D. in Institut Jean Lamour, during which I have had an opportunity to meet a lot of people who made me, personally and professionally, a better person. Without them, this work would be incomplete, and for this, I would like to express my sincere gratitude.

First of all, I am deeply indebted to my supervisor Maxime. Without him, this work would not have been possible. His thoughtfulness and support helped me enormously when I got discouraged about not being productive enough or questioned my willingness to continue. By learning from him, I improved as a person and learned what it really means to become a good researcher. Working with him during the past three years was a great pleasure. I also deeply appreciate his guidance and careful revision of all my many versions of the manuscripts and his trust in me, which encouraged me to get through this journey.

I would like to thank also all the other current and former colleagues of team 107 plasma chauds in IJL. Guillaume, Debraj, Anil, Luigi, Sarah, Stéphane, Thierry, Daniele, Frédéric, Jérôme, Alain and all the others with whom I shared many unforgettable moments. I am also very thankful to my coauthors Xavier, Patrick, and Yusuke, whose fruitful discussions drastically improved my article's writing and scientific content.

Thank you also to all the members of my Judo club, in particular Fabien, Julie, Jean-Philippe, Luis-Arthur, and Sebastien, who taught me the art of Judo, which helped me forget about physics for a moment and gave me a lot of energy to get back to work again. Special thanks to my friends whom I met outside my office. Spending time with you helped me not become crazy.

Finally, I would like to thank my family, who has supported me during my entire studies and encouraged me since my early teenage years to continue on this path. Especial thanks to my grandparents, uncles, and aunts who, despite the time difference, kept encouraging me to finish this whole journey.

This work was funded by the Agence Nationale de la Recherche for the Project GRANUL (ANR-19-CE30–0005). This work was granted access to the HPC resources of EXPLOR (Project No. 2017M4XXX0251) and CINECA MARCONI under Project FUA35 GSNTITE. This work has been carried out within the framework of the EUROfusion Consortium, funded by the European Union via the Euratom Research and Training Programme (Grant Agreement No. 101052200—EUROfusion). Views and opinions expressed are, however, those of the author(s) only and do not necessarily reflect those of the European Union or the European Commission.

Chapter 1

Introduction

Contents

1.1 High-temperature plasmas

1.1.1 Plasmas

The fundamental theoretical concepts of plasma physics were developed in the first half of the 20th century. However, due to the lack of heating techniques, the temperature of experimental plasmas was generally low, in the order of a few electron volts. Within the "low-temperature" plasmas regime, many practical applications were found and developed in manufacturing, medicine, or communication domains. It was not until the middle of the century that the use of plasmas for the production of energy via Fusion reactions was considered. This new goal shifted the relevant energy levels of many orders of magnitude (tens of kilo electron volts) and accelerated the development of modern plasma physics.

At such high energy levels, most particles in the plasma are ionized, we call this a high-temperature or highly ionized plasma. In this case, plasma can be thought of as a collection of free-charged particles with a very small fraction of neutral particles. The behavior of such a state of matter becomes collective in nature, dictated by long-range electromagnetic forces: The motion of a typical particle is governed by electromagnetic interactions with a collection of distant particles instead of binary interactions between neighboring particles, in contrast to the strong coupling among individual particles governing neutral fluids.

Aside from the potential practical importance of plasmas, investigations into plasma dynamics hold inherent interest to physicists on multiple fronts. On a macroscopic scale, the coupling between various motions and fluctuating electromagnetic fields gives rise to considerable studies of plasma instabilities. On a microscopic level, plasma consists of a collection of interacting particles through long-range forces, thus, presenting an N-body problem of immense academic interest. Lastly, it could lead to significant progress in the understanding and connection between the microscopic and macroscopic description of a plasma, such as the transport of particles and energy.

1.1.2 Plasmas models

Since plasma is a collection of charged particles, in principle, a simple model such as Newton's equations of motion will correctly describe the dynamics of the plasma. Nevertheless, modeling the long range interaction between particles is a difficult task, and will require enormous resources to characterize all the interactions between particles of the plasma.

A fluid-like approach can solve this problem by considering not individual particles but macroscopic plasma sections. Through this model, one assumes a plasma to be a smoothly energy-distributed collection of particles, similar to a neutral gas, where quantities such as density, flow velocity, pressure, and temperature dictate the

evolution of the fluid. However, in a high-temperature plasma, this assumption is not true. Specifically, in high-temperature plasmas collisions between particles are few and far between, as a consequence, particles can resonate strongly with electromagnetic waves and induce strong departures from a smooth-fluid distribution. An accurate portrayal of such mechanisms calls for a more accurate theory, the Kinetic model. In the collision-less regime, plasma is correctly modeled by the Vlasov-Maxwell system of equations, which describes the time evolution of particle distributions f in a 6D (3D-3V) phase-space. Relevant kinetic-Vlasov plasmas are astrophysical, laser, or magnetic confinement plasmas.

1.1.3 High-temperature plasmas

In literature, different terms can be encountered depending on the nature of the plasma, such as: ”high-temperature”, ”weakly-coupled”, ”Vlasov”, or ”collision-less”. In astrophysical and interplanetary plasmas, which are low-density plasmas, the absolute temperature reaches levels where the thermal kinetic energy significantly exceeds the potential energy of interactions among charged particles. On the other hand, in magnetic confinement plasmas, the temperature of ions and electrons is of the order of Millions of degrees. Such plasmas are confined in strong magnetic fields, where the collisional frequency (or mean-free-path) is of multiple orders larger than the size of the machine.

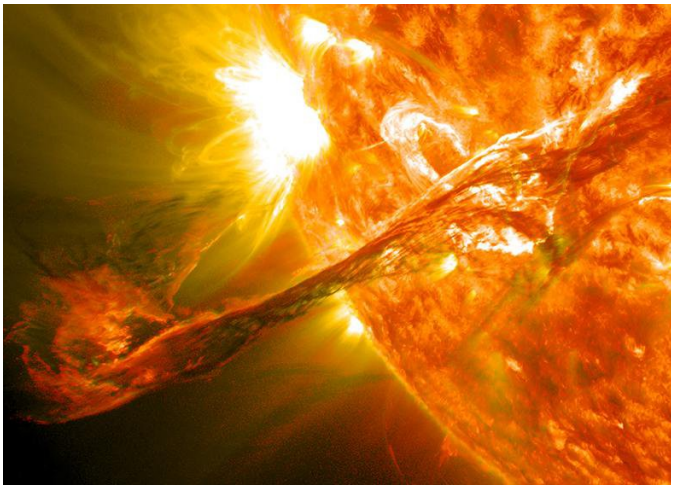

Figure 1.1: High-temperature plasma in a solar flare

One of the challenges in studying high-temperature plasmas is the intricate and complex dynamics displayed by plasma parameters such as particle densities, temperatures, or magnetic fields across various time scales. In the short term, instabilities or fluctuations in these quantities emerge. Some causes include wave-particle resonances,

fast-evolving species like electrons, or nonlinear effects. For intermediate times, the plasma experiences the growth of linear instabilities and transitions toward equilibrium. This includes the development, growth, and dissipation of coherent phase-space structures or the generation of plasma turbulence. And for large timescales, a quasi-stationary state is characterized by strong nonlinear saturation and stabilization of plasma fluctuations. Understanding and controlling all the mechanisms involved in plasma dynamics through theoretical and numerical modeling is of considerable scientific interest, which will result in significant progress for humanity, like magnetically confined fusion energy or space propulsion systems.

1.2 Turbulence and transport in plasmas

Plasma turbulence plays an important role in natural and laboratory plasmas, a notable example is the small-scale turbulence in magnetic confinement fusion, which determines the energy confinement time and performance of the devices. Fundamentally, turbulence and transport are examples of nonlinear dynamics for high degrees of freedom systems, such as plasmas. Which can be triggered by for instance by instabilities or wave-particle resonances. Some examples of very effective transport processes in plasmas are particle and energy flows, or electromagnetic collisions. These result in large mass, charge, and energy transfers, which tend to bring the system toward thermodynamical equilibrium.

1.2.1 Turbulence

Measurements on astrophysical and laboratory plasmas have shown that most high-temperature plasmas of interest are turbulent in nature. This turbulence manifests as particle density or electromagnetic potential fluctuations spanning a broad range of scales. Within these fluctuations, energy cascades between scales, leading to small and large-scale chaotic particle motion, transport of momentum and heat, and the generation of highly dynamical plasma structures.

Turbulence theories aim to model and predict the statistical behavior of microscopic fluctuations and their macroscopic consequences within the entire plasma system through the use of internal quantities such as plasma parameters, electromagnetic fields, and external sources and sinks of particles and energy. Early plasma theories borrowed concepts coming from turbulence theories of neutral fluids, such as near-equilibrium where spectral cascades transfer energy from large to small scales, or mean-field approaches where relaxation mechanisms drive unstable particle distributions. However, research showed that high-temperature plasmas depart greatly from neutral fluid turbulence due to significant non-linear and kinetic effects such as resonances.

1.2.2 Theories and numerical simulations

One of the first theories considering wave-particle resonances is the Quasi-Linear theory [Romanov and Filippov, 1961; Drummond and Pines, 1962; Vedenov et al., 1962] of plasmas turbulence, with several corrections to consider neglected non-linear effects years later, such as resonance broadening [Dupree, 1966; Weinstock, 1968]. The Quasi-linear theory aims to study the problem of plasmas outside equilibrium by neglecting strong non-linear particle trapping and coupling between modes. It has been shown throughout the decades that for a relatively large number of plasmas, quasi-linear theory and resonance broadening are sufficient and correctly predict plasma turbulence. However, for many astrophysical or laboratory high-temperature plasmas, it has been shown that strong particle trapping and non-linear effects take place and drive the dynamics of the plasma. More sophisticated theories have been built in the past decades, which hope to improve the understanding of non-linear turbulence and transport [Berman et al., 1982; Dupree, 1983].

On the other hand, in recent years, thanks to the technological improvement of electronics, complex kinetic numerical simulations have seen a surge in the investigation of plasma turbulence and transport. The use of numerical simulations allows researchers to develop new exciting scenarios on which they can verify analytical theories before implementing them in expensive laboratory devices. Some examples of numerical codes are COBBLES [Lesur et al., 2006a; Lesur, 2010], TERESA [Sonnendrücker et al., 1999; Depret et al., 2000; Sarazin et al., 2005], or GYSELA [Abiteboul et al., 2011; Grandgirard, 2016], which are kinetic codes in two, four, and five-dimensional phase-spaces, respectively. However, the agreement between simulations, theories, and experiments remains incomplete. Numerically relying on arbitrary or non-physical input parameters, a narrow set of approximations, numerical diffusion, or an insufficiently discretized phase-space due to outdated computational capabilities. And analytically, relying on simplified models, extremely limited conditions of validity, or hypotheses that neglect or average-out effects like phase-space structures.

Nevertheless, using analytical theory and numerical simulations to understand plasma turbulence better remains extremely valuable for researchers. In particular, theories and simulations which include full non-linearities, wave-particle resonances, and phase-space structures.

1.3 Phase-space structures

Phase-space structures are specific arrangements of particle distribution phase-space density. They are known in various contexts of plasma turbulence, such as Bump-on-tail, two-stream or ion-acoustic instabilities, Landau damping, atmospheric plasmas, magnetic reconnection, and magnetic-confinement devices.

A variety of phase-space structures are described in the literature, one particular is a vortex-like structure of localized negative phase-space density fluctuation, $\delta f < 0$, that leads to strong local trapping of particles, which is called a phase-space hole. Other structures known as phase space bums or plateaus have local positive $\delta f > 0$ or null $\delta f = 0$ phase-space density fluctuation, respectively.

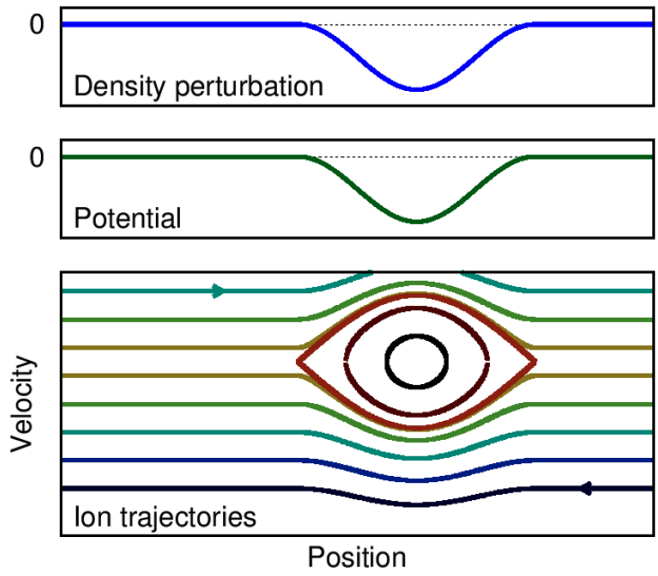

Figure 1.2: Schematic of the different electrostatic quantities for a phase-space electron-hole. In blue is the charge density perturbation, in black is the electric field, and in green is the electric potential. And lastly, the phase space of the electron trajectories: orange for free-passing electrons, brown for trapped electrons, and red for the separatrix.

Phase-space holes are the result of localized kinetic non-linear particle-trapping through their own electrostatic potential; figure 1.2 shows the relation between a phase-space structure (in this case and electron-hole), the density and potential perturbation. Phase-space holes were observed through numerical simulation [Roberts and Berk, 1967], later analyzed by theory [Bernstein et al., 1957; Schamel, 1971; Ghizzo, 1987], and observed in a variety of stellar and laboratory plasmas [Boström et al., 1988; Ergun et al., 1998; Khotyaintsev et al., 2010; Kamaletdinov et al., 2021].

1.3.1 Dynamics of structures

Studies have observed phase-space to have rich and complex dynamics: They can explore the phase-space by accelerating and decelerating, grow in size and depth, be

dispersed or destroyed, and interact or merge with each other. However, quantitatively and predictively little is known about phase-space hole dynamics, except for the non-linear growth rate of an isolated hole [Boutros-Ghali and Dupree, 1982; Berman et al., 1985], and the attractive interaction between different structures [Ghizzo et al., 1987].

Fig. 1.3 shows the life of an isolated phase-space hole: Starting as a small phase-space perturbation, which grows by accelerating and trapping an increasing number of particles, saturating at a phase-velocity close to the average particle velocity of the species, and finally getting destroyed due to non-linear effects with the particle distributions or other phase-space structures.

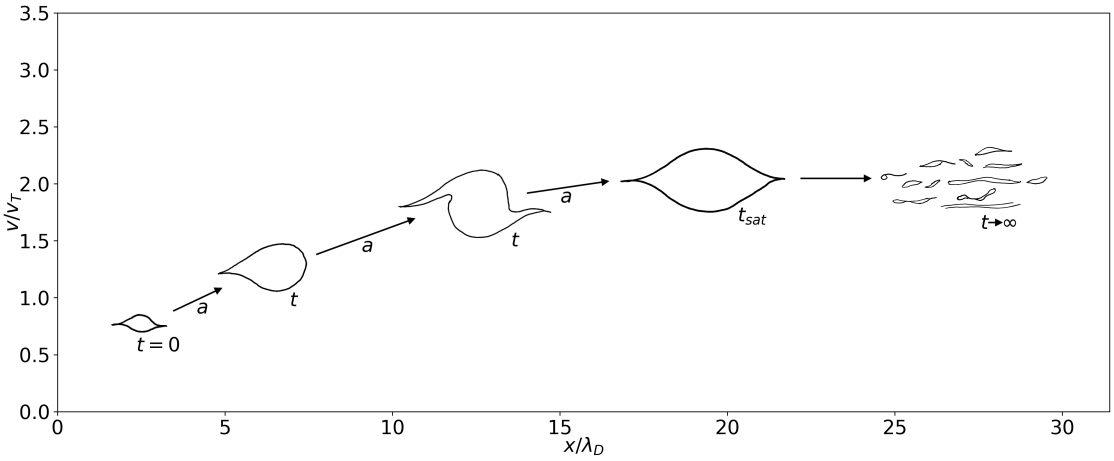

Figure 1.3: Mechanism of the development of a phase-space structure: Small perturbation, growth and acceleration, saturation, and destruction.

This work attempts to quantitatively study the dynamics of isolated phase-space holes through numerical kinetic simulations and analytical theory. Furthermore, an effort was made to investigate the binary interactions between phase-space structures with the aim of predicting the dynamics of the involved structures.

1.4 Objective and Outline

The aim of this thesis is to improve the understanding of particle dynamics, namely diffusion, and transport of particles, develop a strong database of numerical simulations, and develop a strong analytical foundation of the mechanisms in question.

In chapter 2, we describe the analytical scaffold and present the numerical code for the study of particle dynamics in prescribed electric fields. We discuss how the simple problem of particles in a two-wave system presents localized regions of strong

chaos and stochasticity. In particular, we focus on the behavior and statistics of particle trajectories through time and space.

In chapter 3, we show the study of particle dynamics in a prescribed turbulent electric field. We present quasi-linear and resonance-broadening theories applied to plasma waves. Moreover, we show the results of numerical simulations in different regimes of turbulence, including an expression at strong turbulence.

In chapter 4, we present the analytical theory necessary for the construction of a stable phase-space structure in the context of the kinetic code COBBLES. Moreover, we show the implementation in the code and the necessary steps to ensure long-time stability.

In chapter 5, we show the dynamics of phase-space holes through kinetic simulations and theory. We present the dynamics of isolated phase-space holes, including growth, acceleration, and saturation. And we show the results of binary-interactions between phase-space holes.

In chapter 6, we show the effects of phase-space holes in the dynamics of charged particle trajectories. We compare the predicted diffusion of phase-space holes against numerical simulations and how it affects quasi-linear theory.

Finally, in chapter 7, we summarize the principal results and propose further analytical and numerical investigations that can be pursued based on these findings.

Chapter 2

1D Particle trajectories in one, and two, wave(s) electric field

Contents

Throughout the years, the study of nonlinear dynamical problems has been at the center of numerous studies in different domains, such as astronomy, particle physics, statistical mechanics, quantum mechanics, and plasma physics. The pendulum is arguably the oldest and most important non-linear problem in all physics, with records showing that it was first studied in the early 17th century by Galileo Galilei. One of the most critical uses for centuries was as the most precise timekeeping method, thanks to the regular oscillations of the pendulum. Today pendulums are used in various scientific instruments like seismometers and accelerometers or for leisure in amusement parks. Academically, the pendulum represents one of the fundamental problems for any future physicist since it corresponds to the dynamics of a system under a simple sinusoidal wave.

As one increases the number of waves in the system, an issue arises, the system's dynamics become chaotic. Indeed, as the number of degrees of freedom increases, the Hamiltonian systems transition to a phenomenon known as large-scale chaos. This topic has been the subject of extensive research during the latter half of the 20th century, as documented by researchers such as Chirikov [Chirikov, 1969], Escande [Escande and Doveil, 1981], and Brandon [Brandon et al., 1995]. This chapter will delve into the system's dynamic of single and a pair of sinusoidal waves. Additionally, we will introduce the PERKS code, a tool used to study these systems.

2.1 Deterministic Hamiltonian system

2.1.1 Particle trapping

In classical mechanics, a potential well represents a specific region in space where a particle with a certain energy level can be confined. This confinement is due to the presence of a higher potential surrounding the particle. This is analogous to a ball resting at the bottom of a valley, where it is *trapped* unless provided enough energy to climb over the surrounding hills.

In the context of classical physics, potential wells can be used to describe a large variety of physical phenomena, such as the oscillations of a pendulum, the orbits of planets in the solar system, or the trapping of charged particles in electric or magnetic fields. In such problems, the characteristics of the potential well, in particular the shape and depth, play an important role in determining the particle's motion. The motion of particles within a potential well can be classified into two categories: *Trapped* and *Passing* particles. Trapped particles are any particles with insufficient energy to overcome the potential barrier, and these particles will remain captured within the well. On the other hand, Passing particles, also known as Free particles, are all particles possessing sufficient energy to escape the potential well. A particle will remain either trapped or free within the potential well unless provided a mechanism for energy exchange, such

as particle collisions, energy dissipation, or particle-wave resonances.

Analytically, one can express the trapping condition starting from the total energy equation of a particle, which writes:

$$E(x,v) = \frac{mv^2}{2} + V(x) \tag{2.1}$$

where $E(x,v)$ is the particle's total energy, $V(x)$ is the classical potential energy of the system, and m, v, and x, are the particle mass, velocity, and position, respectively.

If the particle's energy is lower than the maximum value of the potential energy $E < V_{max}$, then the particle is said to be trapped in the potential. Otherwise, if the particle's energy is higher than the maximum potential energy $E > V_{max}$, it is said to be a free or passing particle. Note the case where both the total and maximum potential energy are equal $E = V_{max}$. In this case, this trajectory is named the *Separatrix*, which is the boundary separating the two different particle behavior, and its velocity is defined to be:

$$v(x) = \pm\sqrt{\frac{2}{m}\Big(V_{max} - V(x)\Big)} \tag{2.2}$$

2.1.2 Pendulum: Sinusoidal wave

In general, the problem of trapped particles in an arbitrary potential can not be solved analytically. As a result, it becomes necessary to address specific cases independently of each other. One of the most important one-dimensional models in all of physics is the Pendulum problem. This problem is a staple in all first-year university courses on classical mechanics. Nevertheless, it is rarely solved in its entirety. Indeed, traditionally the problem is simplified into the *Harmonic oscillator*, which can easily be solved.

For the Pendulum problem, the Hamiltonian of the system, denoted as $H(v,x)$, is expressed as follows:

$$H(v,x) = \frac{mv^2}{2} - A\cos kx \tag{2.3}$$

where A is the positive amplitude of the potential energy $A = +|A|$, and k the wave number of the potential energy. The potential energy of the pendulum takes the form of a sinusoidal wave. This implies the presence of potential wells in which particles can become trapped. This makes the Pendulum problem a useful model for studying the behavior of trapped particles in potential wells. In order to find the characteristic equations of motion for the Pendulum, we first find the Action-Angle variables J and ω_b.

From equation 2.3, one can rewrite the Hamiltonian in terms of the generalized coordinates (q,p) and obtain a relationship between the momentum p and generalized

position $q = kx$

$$p = \pm\sqrt{\frac{2m}{k^2}}\sqrt{H_0 + A\cos q}\,, \tag{2.4}$$

where H_0 is the constant total energy of an arbitrary trajectory. Here the value of the ratio $\frac{H_0}{A}$ gives the type of trajectory will perform: Trapped for $\frac{H_0}{A} < 1$ and Passing for $\frac{H_0}{A} > 1$. By definition, the action of a couple of generalized variables (q, p) is defined as:

$$J = \frac{1}{2\pi}\oint p\, dq \tag{2.5}$$

where p is the generalized momentum of equation 2.4 in other words

$$J = \frac{1}{2\pi}\sqrt{\frac{2m}{k^2}}\oint \sqrt{H_0 + A - 2A\sin^2 q/2}\, dq \tag{2.6}$$

where the $\cos q$ of equation 2.4 was replaced by the half-angle identity. From this equation, we define the quantity

$$a = \sqrt{\frac{H_0 + A}{2A}} \tag{2.7}$$

referred to as the *elliptic modulus*, note that $a = 1$ defines the separatrix. Moreover, since a particle trajectory are symmetrical in both the horizontal and vertical direction, we can reduce the contour integral to an integral over a quarter of the trajectory, i.e. from $q = 0$ to $q = q_m$, the maximum value of the generalized coordinate q. And by reorganizing the equation, we obtain the following:

$$J = \frac{4a}{\pi}\sqrt{\frac{mA}{k^2}}\int_0^{q_m}\sqrt{1 - \frac{1}{a^2}\sin^2 q/2}\, dq\,. \tag{2.8}$$

Passing particles

To solve 2.8 for passing particles, $a > 1$, we consider only the particle trajectories at positive momentum, in other words, those in the top half of the phase space. Then we define the action J of a passing particle as half of equation 2.8. Note that since the potential energy is periodic in the q direction, then passing particle trajectories will also be periodic in the same direction. Therefore, the maximum q is given at $q_m = \pi$. By choosing the change of variable $\theta = q/2$ and simplifying the action equation 2.8, we simplify the action as:

$$J = \frac{4a}{\pi}\sqrt{\frac{mA}{k^2}}\int_0^{\pi/2}\sqrt{1 - \frac{1}{a^2}\sin^2\theta}\, d\theta\,. \tag{2.9}$$

Note that the right-hand side of equation 2.9 is by definition the complete elliptic integral of the second kind $E(a)$. Therefore, we can simplify the action of passing particles as:

$$J = \frac{4}{\pi}\sqrt{\frac{mA}{k^2}}aE\left(\frac{1}{a}\right) \ . \tag{2.10}$$

Note that the argument of the elliptic integral of the first kind must satisfy the inequality $0 < 1/a < 1$, which in this case is true, since for passing particles $a > 1$.

To obtain the characteristic frequency of oscillation of particles, in other words, the time it takes a particle to perform one periodic orbit, we use the frequency equation of Hamiltonian mechanics defined as:

$$\omega_b = \left(\frac{\partial J}{\partial H}\right)^{-1} \ . \tag{2.11}$$

From equation 2.10, we deduce that the oscillation frequency of a passing particle with elliptic modulus a is equal to

$$\omega_{b,P} = \pi\sqrt{\frac{k^2A}{m}}\frac{a}{K\left(\frac{1}{a}\right)} \ , \tag{2.12}$$

where $K(z)$ is the complete elliptic integral of the first kind.

Trapped particles

In order to solve 2.8 for trapped particles, $a < 1$, we choose the change of variables $\frac{1}{a}\sin^2 a/2 = \sin\varphi$, which leads us to rewrite the integral of equation 2.8 as,

$$J = \frac{8a^2}{\pi}\sqrt{\frac{mA}{k^2}}\int_0^{\pi/2}\frac{1-\sin^2\varphi}{\sqrt{1-a^2\sin^2\varphi}}\,d\varphi \ . \tag{2.13}$$

Note that the maximum of q occurs when $p = 0$, therefore from equation 2.4, we obtain $q_m = 2\arcsin a$. Which in addition to the change of variable gives us $q_m = \pi/2$. Thus trapped particle action can be rewritten as a function of the first and second kind complete elliptic integrals $K(a)$ and $E(a)$:

$$J = \frac{8}{\pi}\sqrt{\frac{mA}{k^2}}\left[E(a) - (1-a^2)K(a)\right] \ , \tag{2.14}$$

note that the elliptic modulus a must satisfy the inequality $0 < a^2 < 1$, which in the case of trapped particles is satisfied.

To obtain the characteristic frequency of oscillation of trapped particles, we once again inject the action variable of trapped particles into equation 2.11. We deduce that the oscillation frequency of a trapped particle with elliptic modulus a is equal to

$$\omega_{b,T} = \frac{\pi}{2}\sqrt{\frac{k^2 A}{m}}\frac{1}{K(a)} \tag{2.15}$$

Knowing this previous methodology, we can solve the equations of motion for trapped particle trajectories in the Pendulum problem. Indeed from equation 2.5, we can deduce that the differential equation of x can be written as:

$$\frac{dx}{dt} = \pm 2a\sqrt{\frac{A}{m}}\sqrt{1-\frac{1}{a^2}}\sin^2 kx/2\ . \tag{2.16}$$

To simplify this expression, we choose the change of variable $\sin kx/2 = a\sin z$, which leads us to rewrite the differential equation as,

$$\frac{dz}{dt} = \pm\sqrt{\frac{Ak^2}{m}}\cos kx/2\ . \tag{2.17}$$

After a few algebraic calculations, this expression can be transformed into the incomplete elliptic integral of the first kind $K(z,a)$

$$\int_0^t \sqrt{\frac{Ak^2}{m}}dt' = \int_0^z \frac{dz'}{\sqrt{1-a^2\sin^2 z')}} = K(z,a) \tag{2.18}$$

where z is known as the Jacobi elliptic amplitude used to define the Jacobi elliptic functions. Moreover, the elliptic amplitude is also known as the inverse function of the incomplete elliptic integral of the first kind $z = K^{-1}(\sqrt{\frac{Ak^2}{m}}t+\phi_0, a)$, here ϕ_0 is the integration constant of the left term of equation 2.18. In other words, by injecting equation 2.18 into the change of variable $\sin z = \sin kx/2/a$ we can obtain the equations of motion (x,v):

$$x(t,a) = \frac{2}{k}\arcsin\left(a\,\mathrm{sn}\left[\sqrt{\frac{Ak^2}{m}}t+\phi_0, a\right]\right) \tag{2.19}$$

$$v(t,a) = \pm 2a\sqrt{\frac{A}{m}}\sqrt{1-\mathrm{sn}^2\left[\sqrt{\frac{Ak^2}{m}}t+\phi_0, a\right]} \tag{2.20}$$

where $\mathrm{sn}(\phi,a)$ is the Jacobi elliptic sinus function, defined as $\mathrm{sn}(\phi,a) = \sin(z(\phi,a))$. Note that ϕ_0 is obtained trough equation 2.18 for $t=0$, in other words $\phi_0 = K(\pi/2,a)$.

2.1.3 Harmonic Oscillator limit

The harmonic oscillator is one of the well most known problems in physics. Most physicist learns how to solve the Harmonic oscillator during their studies, yet it is the most underestimated problem by students for its simplicity and strong hypothesis. Nevertheless, it is used in countless physics domains to solve the world's fundamental questions.

Since the Harmonic oscillator is the small perturbation limit of the Pendulum problem, one obtains the equivalent quantities by taking the respective limit of the equations shown in the previous section 2.1.2. Indeed by taking the limit of deeply trapped particles, in other words, $a << 1$, we can simplify the trapped particle frequency as:

$$\omega_{b,0} = \sqrt{\frac{k^2 A}{m}} \, . \tag{2.21}$$

Since in the limit $a << 1$, $K(a) \to \pi/2$. Moreover, equations 2.19 and 2.20 are simplified into the classical Harmonic oscillator,

$$x(t) = x_0 \cos\left(\omega_{b,0} t + \phi_0\right) \, , \tag{2.22}$$

$$v(t) = -x_0 \omega_{b,0} \sin\left(\omega_{b,0} t + \phi_0\right) \, , \tag{2.23}$$

where x_0 and ϕ_0 are the initial particle position and phase.

2.2 PERKS code

2.2.1 Principle

In order to study particle dynamics, we have developed a numerical code that performs the computation of test particle trajectories in the presence of an external, non-self-consistent, one-dimensional electric field based on a fourth-order Runge-Kutta algorithm. We have named this code PERKS, which stands for *Parallel Electrostatic Runge-Kutta Solver*.

PERKS is designed to solve Newton's one-dimensional equation of motion for N independent test particles. An important feature of this code is its parallelization across particle space. This means that each processor is assigned to compute the trajectories of a subset of the total number of particles, thereby improving computational efficiency. The Runge-Kutta method, specifically the fourth-order used in PERKS, is a numerical technique used to solve ordinary differential equations. It provides a balance between computational complexity and accuracy, making it an ideal choice for our work.

The concept of *test particles* refers to an ensemble of particles that are used to study the statistical effects of the electric field on particle dynamics. In our case, these test

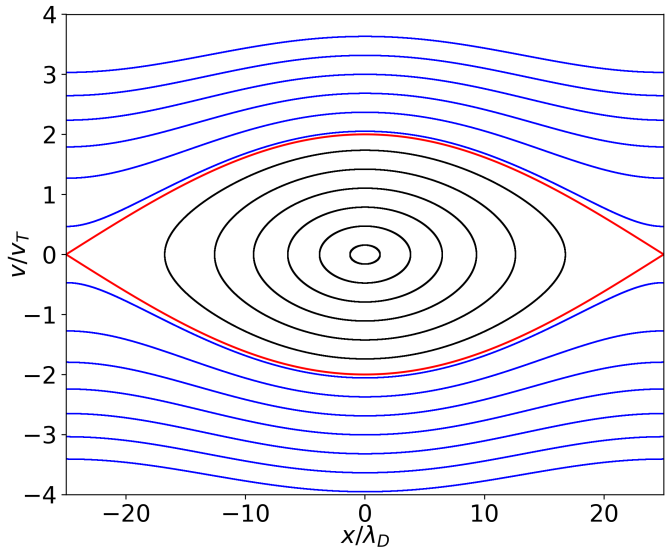

Figure 2.1: Numerical phase-space trajectories for the pendulum problem. Trapped particles in black, passing particles in blue, and the separatrix in red.

particles are independent of each other, meaning that the motion of one particle does not affect the other particles or the electric field. In other words, our code does not account for particle-particle collisions nor retroactive effects on the electric field, implying that its behavior will be prescribed with external parameters. This assumption simplifies the approach, allowing us to focus on the desired effects we want to study.

At $t = 0$, N test particle trajectories are initialized with random positions $x_{0,i}$ and velocities $v_{0,i}$, and here the i stands for the particle index. In particular, particle positions are distributed uniformly in a simulation box of length L_x. In other words, in the interval $[0; L_x[$. Similarly, particle velocities are distributed around a mean velocity v_0 with a Gaussian probability distribution function. In practice, an external electric field $E(x, t)$ is provided as an analytical function from which the algorithm can calculate E at the particle position, up to machine precision (double float).

Particle trajectory diagnostics are computed at each time step, such as particle distributions in both velocity and position space, the first four statistical moments (mean, variance, Skewness, and Kurtosis), and the maximum finite-time Lyapunov exponents. For more information on these diagnostics, please refer to section 3.4.1 and section 3.4.2.

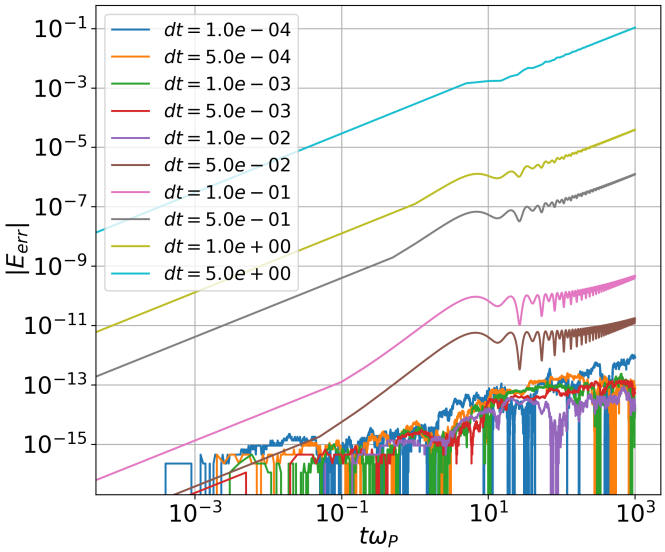

Figure 2.2: Numerical relative error of test particles in a sinusoidal potential as a function of time.

2.2.2 Application to the Pendulum

In order to verify and quantify the accuracy of the PERKS code, we studied numerical particle trajectories in the presence of a sinusoidal potential of amplitude A. From the theory in section 2.1.2, we expect two types of particle trajectories, passing and trapped particles, separated by a separatrix.

We performed a series of simulations for particles initialized with zero initial positions $x_{0,i}$, i.e. in the wave reference frame, and initial velocity $v_{0,i} = 0$. Analytically we calculated each particle's elliptic modulus a_i trough equation 2.7, which in the case of particles with such initial conditions, is proportional to the initial particle velocity.

Figure 2.1 shows different pendulum phase-space trajectories calculated through the numerical code PERKS. Trapped particles are shown in black, passing particles in blue, and the analytical separatrix in red.

PERKS relative error

As with any numerical algorithm to solve differential equations, the primary source of numerical error is the order of small-parameter expansion of the method used. In our case, we use the fourth-order Runge-Kutta method meaning that the total accumulated error is on the order of $O(dt^4)$, while the local truncation error is on the order of $O(dt^5)$, where dt is the time-step.

Numerically we obtain figure 2.2, which shows the relative error in total energy

between numerical simulations and theory as a function of time for different time step values. As anticipated, the larger the time step, the larger the error on the total energy. For small values of dt ($< 0.1/\omega_P$), the numerical error on the energy remains smaller than 10^{-9}, at a final time of $t_{fin} = 10^3/\omega_P$, which considering the number of iterations performed is more than enough for a correct description of particle trajectories (We observed important changes in the behavior of a few trajectories for $t_{fin} = [10^4, 10^5]/\omega_P$, and many for $t_{fin} = 10^6/\omega_P$). This manuscript's numerical simulations with the PERKS code have a time step smaller than $0.1/\omega_P$.

2.3 Two waves: Standard map

At the start of the 20th century, physicists began to delve into the dynamics of particles influenced by the presence of two sinusoidal waves. At first glance, this problem appears straightforward, only requiring the addition of a second wave to the existing wave from the Pendulum problem. However, as is often the case in physics, reality proved to be more complicated. In practice, the system showed unpredictable behavior, what is known as chaos or stochasticity.

Throughout the years, the exploration of chaos often led to intriguing mathematical scaffolding, one of which is the Standard Map, also known as the Chirikov–Taylor map [Chirikov, 1969; Brandon et al., 1995]. This mathematical model allows the easy visualizations of particle dynamics for systems with two degrees of freedom, such as the double pendulum. These types of systems are prevalent in various fields, like stellar mechanics, particle physics, chemistry, fluid dynamics, solid-state physics, or in the interest of this manuscript, plasma physics.

2.3.1 Transition to Hamiltonian stochasticity

In the field of chaos and stochasticity, two key questions often arise: How can the chaotic motion be predicted, and when does a system transition into chaotic behavior? This has been partially solved since, for a straightforward Hamiltonian system, the degree of stochasticity is quantified using the Chirikov resonance-overlap criterion, denoted as Λ first introduced by Chirikov [Chirikov, 1960], also commonly referred to as the stochasticity parameter s. Λ is defined as,

$$\Lambda = \frac{\Delta^{1/2} v_0 + \Delta^{1/2} v_1}{\Delta v^{\phi}_{0,1}} \tag{2.24}$$

where $\Delta^{1/2} v_i = \sqrt{\frac{2A_i}{m}}$ is the maximum half-width of the separatrix along the velocity direction of the ith wave, A_i the amplitude of the potential of the ith wave. And $\Delta v^{\phi}_{0,1}$ is the difference in phase velocity between the first and zeroth waves.

The Chirikov resonance-overlap parameter measures the increase in stochasticity in the system, which is directly proportional to the overlap between the two interacting waves. As the value of Λ increases, stochasticity transitions from local to global. Since in a two-degree-of-freedom system, such as the one studied in this section, as the overlap between the waves increases, particles within the system's boundaries can begin exploring all allowed regions of phase-space rather than being confined to one trajectory or a limited region of phase-space. Therefore it measures the fraction of the phase-space area where chaos is present.

A more natural characterization of the *transition to stochasticity* is that as the strength of the perturbation increases, then the regions of phase-space in between the separatrixes will present an increasingly larger stochastic motion. These regions have been studied in detail trough the KAM, *Kolmogorov-Arnold-Moser*, theory [Kolmogorov, 1954; Möser, 1962; Arnold, 1963]. Some examples of problems where KAM theory is used for are the 3-body problem, double coupled pendulum, pr magnetic islands on magnetic fusion devices.

2.3.2 Standard map

In order to study the transition between periodic-bounded orbits and stochastic orbits, that can explore a large area of phase-space, we use the standard map model. This map describes the Poincaré section of the system. The mapping is obtained from the 2π periodic time-dependent Hamiltonian equations of motion 2.3,

$$x_{i+1} = x_i + 2\pi v_{i+1} \tag{2.25}$$

$$v_{i+1} = v_i - A \sin k x_{i+1} \tag{2.26}$$

where x_i and v_i are the particle position and velocity for the ith iteration of mapping, A is the amplitude of the time-dependent perturbation wave, and k is the wave number. Every iteration of this map generates one point of the Poincaré map of the system, whereas, with the traditional numerical integration of the equations of motion, tens to hundreds of steps are necessary to get one point of the Poincaré map. Therefore, in terms of numerical resources, the standard map allows for a more efficient approach to studying such systems.

Figures 2.3, 2.4 and 2.5 show the Poincaré section for the two-waves problem. These figures show the characteristic orbits for three different Chirikov overlap parameters, $\Lambda = 0.50$ for 2.3, $\Lambda = 0.70$ for 2.4, and $\Lambda = 1.10$ for 2.5. Each color represents a different initial condition; note that some colors are repeated.

In these figures, four types of regions can be observed:

- Firstly, a region of phase-space where orbit follows passing, or free, particle trajectories, similarly to the passing particle trajectories of figure 2.1 for the pendulum. These orbits can be better observed in figure 2.3. They are located around

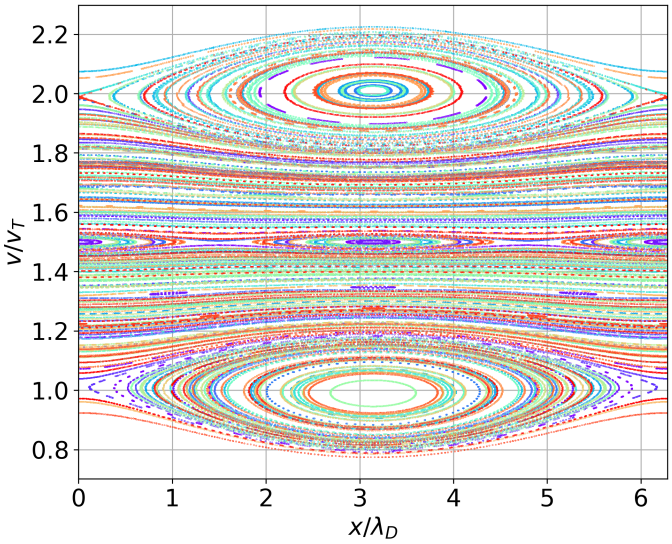

Figure 2.3: Poincaré section of the two-wave system, with a spatial periodicity of 2π, and a Chirikov overlap parameter of $\Lambda = 0.50$. Obtain via particle integration with the PERKS code.

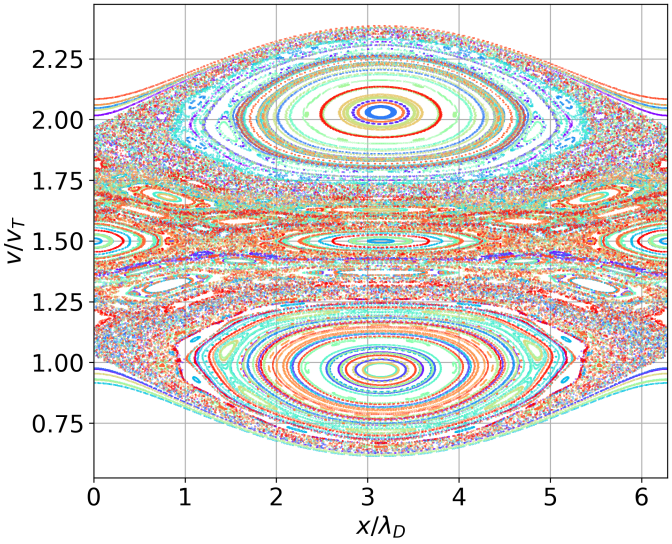

Figure 2.4: Poincaré section of the two-wave system, with a spatial periodicity of 2π, and a Chirikov overlap parameter of $\Lambda = 0.70$. Obtain via particle integration with the PERKS code.

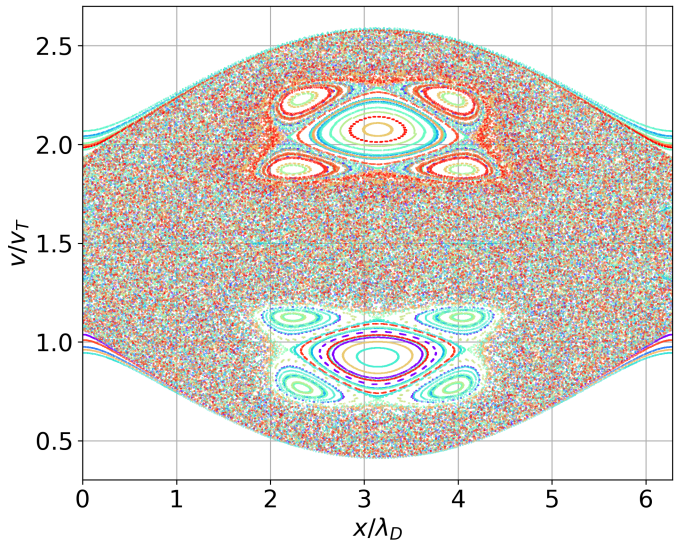

Figure 2.5: Poincaré section of the two-wave system, with a spatial periodicity of 2π, and a Chirikov overlap parameter of $\Lambda = 1.10$. Obtain via particle integration with the PERKS code.

the individual separatrixes and in between the waves. As for the pendulum, particles in this region are free of any potential and will only explore a limited range of velocities. Note that only a few passing particle orbits above the resonance are shown to prevent cluttering.

- Secondly, two regions where trajectories follow the trapped, or closed, orbits in phase-space, such as the two large regions at phase-velocity of $1v_T$ and $2v_T$. Here, particles are strongly trapped in each wave's potential and follow slightly deformed trapped particle trajectories, similar to the trapped orbits in figure 2.1 for the pendulum.

- Smaller localized regions of phase space where particles follow trapped-like orbits; however, they are regular trajectories. In these regions, particles are trapped in what is known as secondary islands generated via the interaction of the two waves or main islands. These are generally localized in the intersection between both waves, in this case with a phase-velocity of $1.5v_T$, but also found in between layers of trapped particle orbits from the main islands, like the ones around a phase-velocity of $2v_T$ and spatial coordinate of $1\lambda_D$ on figure 2.4, or the four secondary islands, clearly visible due to their size, around the main islands in figure 2.5. One property of the Standard map is that if we zoom in on one of these secondary islands, we would observe fractal property, in which new sec-

ondary islands would appear.

- And finally, a region where stochasticity and chaos dominate the behavior or particle trajectories. This stochastic region can be better observed in figure 2.5 due to the large overlap parameter. Here, any initial condition located in this region will, with enough time, explore the entirety of the stochastic region. Here the secondary islands are confined to around the main islands with a few small secondary islands in the intersection at phase-velocity $1.5v_T$.

The standard map problem for two interacting waves shows an intermediate step between a single wave (pendulum) dynamics and what occurs in plasmas where resonances between many waves can occur. It displays the transition between deterministic trajectories of single isolated waves and the stochastic behavior of particles in a system of two coupled waves.

2.4 Conclusion

In summary, in this chapter, we recalled the basic mechanism of particle trapping in potential wells, in particular for the pendulum problem and harmonic oscillator. We presented the test particle code PERKS used in this manuscript, the basic algorithm and we applied it to the pendulum problem and the two waves system. For the latter, we presented the Standard map and the notion of stochasticity in a system of two coupled waves, as well as the Chirikov overlap criterion which characterizes the stochasticity of a system with two or more coupled waves.

This chapter serves as an introduction and intermediate to the more complicated system of many interacting waves. The following chapter 3 presents the problem of charged particles in the presence of a prescribed turbulent electric field, where a more comprehensive study on stochasticity and diffusion of particles is presented.

Chapter 3

Turbulent electric field: Many interacting waves

Contents

In the following chapter, we delve into the effects turbulent electric fields have on charged particle trajectories. The content is primarily drawn from an article we published in early 2023 [Guillevic et al., 2023], with minor modifications to ensure consistency of notation and a restructuring of the sections to provide a comprehensive narrative.

Charged particle velocity-space diffusion in a prescribed one-dimensional turbulent electric field is investigated through numerical trajectories in phase-space (1D1V) and compared against quasi-linear theory (QL), including resonance broadening (RB). A Gaussian spectrum electric field of variable amplitude E is studied in conjunction with two plasma dispersion relations, namely the Langmuir and ion-acoustic dispersion. A first parameter scan shows that RB effects become significant for a Kubo number K of a few percent. A Kubo number scan shows that diffusion increases as a power law of $D \propto K^3 \propto E^{3/2}$ for large Kubo numbers. Moreover, at large Kubo numbers, transport processes include significant diffusion measured at velocities much higher than the resonant region, where QL and RB predict negligible diffusion. For times much larger than the trapped particle flight time τ_b and the autocorrelation time τ_0, the velocity distribution departs from a Gaussian. Nevertheless, measurements show that the variance increases linearly in time, with a Hurst parameter of $H \sim 0.5$, where the diffusion scales as $K^{5/2} \propto E^{5/4}$ and $K^{3/2} \propto E^{3/4}$ for small and large Kubo number respectively.

3.1 Introduction

The full description of charged particle dynamics in an electric field including several waves is sometimes divided into two categories: First, in the small amplitude limit, each particle interacts linearly with only one of the waves, and the dynamics are regular. Second, as the amplitude of the waves grows, particles interact with more than one wave leading to chaotic dynamics. From the point of view of the waves, the non-linear wave-particle interactions lead to energy cascades from one wave towards many other waves [Kolmogorov, 1941], leading to the generation of lower and higher modes, here the modes refer to the eigenfunction of the system. In fully developed turbulence, the electric field modes can be in random phase between each other, and the dynamics become complex; particles can be trapped in a wave and again de-trapped due to the interaction of a different mode. In a collision-less plasma, turbulence is one of the leading causes of particle transport and energy losses through plasma wave-particle resonances. In addition, a significant impact of turbulence is in the heating of the plasma in the form of particle acceleration [Mcbride et al., 1972]. The heating of particles has substantial consequences when energetic particles drive instabilities, in magnetic reconnection in space plasmas [Hamilton and Petrosian, 1992; Liu et al., 2008], stimulated Raman scattering [Gorbunov, 1973], or laser-plasma interactions [Bychenkov, 2018].

In the early 60s, turbulence studies saw a surge with the introduction of quasi-linear theory [Romanov and Filippov, 1961; Drummond and Pines, 1962; Vedenov et al., 1962], and resonance broadening [Dupree, 1966; Weinstock, 1968]. Quasi-linear theory first aimed to study the problem of plasma dynamics outside equilibrium by neglecting mode coupling, considering part of the non-linear terms, and the evolution in time of particle distribution, in which it is assumed that turbulence does not trap particles. Under these conditions, it is possible to derive an expression for transport as an expansion of the electric field amplitude. For moderate amplitudes (or low dispersion), non-linear terms are no longer negligible, which leads to a broadening of wave-particle resonances and mode coupling effects. Including the effect of QL diffusion in the model of particle motion, known as re-normalization, enables the account of this broadening [Adam et al., 1981; Laval and Pesme, 1983].

For prescribed electric fields with random phases, studies have shown a strong qualitative and quantitative agreement with the quasi-linear theory [Doveil and Grésillon, 1982; Hirose and Ishihara, 1999] at low electric field amplitude. Here we investigate the effects of high amplitude turbulence [Vlad and Spineanu, 2017; Médina et al., 2018; Lim et al., 2020]. Regarding the self-consistent problem, that is accounting for the modification of mean fields. It has been experimentally [Tsunoda et al., 1987b,a, 1991] and numerically [Besse et al., 2011] demonstrated that re-normalization is not necessary at low amplitude. Nevertheless, recent numerical simulations for the self-consistent bump-on-tail instability [Crews and Shumlak, 2022] reveal that the quasi-linear theory fails to predict plasma processes at low amplitude, enhanced diffusivity, and phase-space restructuring.

Analytically, one of the parameters ruling the validity of quasi-linear and resonance-broadening theories is measured in terms of the Kubo number [Kubo, 1963]. This quantity is defined as the ratio between the time it takes the turbulent electric field to change its shape, referred to as the autocorrelation time τ_0, and the time it takes a trapped particle to complete an orbit, referred to as the flight time or bounce time τ_b. In other words, the Kubo number is

$$K = \tau_0/\tau_b \tag{3.1}$$

Alternatively, by rewriting this expression as a function of the electric field amplitude, we obtain the expression $K \propto E^{1/2}$, since $\tau_b \propto E^{-1/2}$. Note that, for quasi-linear and resonance broadening theories to be applied, the Kubo number should be much lower than unity $K \ll 1$ [Vedenov et al., 1962].

The importance of the Kubo number is ubiquitous in the literature related to turbulence. First, it allows the differentiation of the type of trajectory performed. As a mental representation, one may picture particles jumping between arcs of trapped trajectories for $K \ll 1$, and particles performing multiple trapped orbits separated by small jumps (or arcs) between two different trapped particle trajectories [Vlad et al.,

2004; Escande and Sattin, 2007] for $K \geq 1$. Furthermore, the Kubo number emerges in multiple plasma turbulence theories, such as quasi-linear and mean-field theories [Diamond et al., 2010; Lenard, 1960; Balescu, 1963], the latter describing the relaxation transport in plasmas.

Calculations based on mixing length theory assume that the Kubo number is close to unity $K \simeq 1$ [Dupree, 1972; Diamond et al., 2010], rather than $K \ll 1$, as required for the validity of the quasi-linear theory. However, mixing-length and quasi-linear theories are often used simultaneously.

This study investigates the statistical diffusion coefficient of test particles in a prescribed one-dimensional turbulent electric field. We compare results from numerical trajectories against quasi-linear theory, including resonance broadening. Diffusion is investigated for ion-acoustic and Langmuir dispersion relations to compare the effects of dispersivity, and a Gaussian amplitude electric potential spectrum is adopted. Different regimes of particle trapping [Doveil and Grésillon, 1982; Hirose and Ishihara, 1999] are investigated, $K \geq 1$ in particular. We address the following questions: How far quasi-linear theory works from the $K \ll 1$ regime? Is there a way to expand, correct, or replace quasi-linear theory to describe a plasma in the $K > 1$ regime? These questions are deeply connected with standard map problem [Chirikov, 1969, 1979; Rechester et al., 1981; Escande, 1982]. In this work, we are concerned with many resonances.

In section 3.2, quasi-linear and resonance-broadening theories are presented. We introduce the analytical description for the prescribed electric field in section 3.3 in the case of plasma waves. Numerical results are reported in sections 3.5.1 and 3.5.2 for small and large Kubo number regimes, respectively. Finally, a conclusion is provided in section 3.6.

3.2 Turbulent autocorrelation time and quasi-linear theory

In this section, we introduce the quasi-linear theory [Vedenov et al., 1962; Sagdeev, 1966] and resonance broadening correction [Dupree, 1966, 1967; Adam et al., 1981; Ishihara et al., 1992] to study homogeneous steady-state turbulence in a one-dimensional plasma.

3.2.1 Autocorrelation time

We focus on the Eulerian two-point autocorrelation function of the electric field $E(x,t)$, defined as $\langle E(0,0)E(x,t)\rangle$, where the brackets $\langle\cdot\rangle$ stand for the statistical average over

an ensemble of particles, while t and x are the displacements over time and space respectively.

From the point of view of a particle at a given velocity v, the electric field evolves over a characteristic time scale called autocorrelation time. This time defines the typical time over which there is a noticeable change in the electric field shape. Analytically, the Lagrangian autocorrelation time $\tau_0(v)$ [Kubo, 1963] is defined as the integral of the two-point autocorrelation of the electric field,

$$\tau_0(v) = \frac{1}{\langle E(0,0)^2 \rangle} \int_0^{+\infty} dt \int_{-\infty}^{+\infty} dx \delta(x - vt) \langle E(0,0) E(x,t) \rangle \tag{3.2}$$

where $\delta(x-vt)$ is the Dirac delta function, and v the velocity of particles in the electric field. By solving the space integral equation (3.2) is simplified as

$$\tau_0(v) = \frac{1}{\langle E(0,0)^2 \rangle} \int_0^{+\infty} dt \langle E(0,0) E(vt,t) \rangle \tag{3.3}$$

Note that τ_0 is often interpreted as the time it takes for the electric field to change its shape. However, for our purposes, it represents the time it takes particles to receive a velocity kick from a low-amplitude turbulent electric field, in other words, $K \ll 1$.

3.2.2 Quasi-linear theory for low amplitude fields

To study the one-dimensional motion $(x_i(t), v_i(t))$ of a charged particle, identified by an index i, in a turbulent electric field $E(x,t)$, we use Newton's equation of motion

$$\frac{d^2 x_i}{dt^2} = \frac{q}{m} E(x_i, t) \tag{3.4}$$

where q and m are the electric charge and mass of the particle, respectively.

By integrating equation of motion (3.4) over time, the i-th particle velocity variation $\Delta v_i(t) = v_i(t) - v_i(0)$ at time t is obtained as

$$\Delta v_i(t) = \frac{q}{m} \int_0^t dt' E(x(t'), t') \tag{3.5}$$

Moreover, the statistical mean square variation σ_v^2, or variance, of an ensemble of N particles is defined as

$$\sigma_v^2 = \frac{1}{N} \sum_{i=1}^{N} \left(\Delta v_i(t) \right)^2 \tag{3.6}$$

In quasi-linear theory, the unperturbed motion $x_i(t) = x_i(0) + v_i t$ is substituted into equations (3.5) and (3.6). Then, by considering that the electric field evolves slowly

in time, we can simplify the double integral in the square term of (3.6) to a single integral in time. For large enough times, it becomes

$$\sigma_v^2 = 2tD_0(v) \tag{3.7}$$

Reminiscent of Brownian motion, the velocity variance increases linearly with time. Here, the rate of increase is given by the quasi-linear diffusion coefficient

$$D_0(v) = \frac{q^2}{m^2}\langle E(0,0)^2\rangle \tau_0(v) \tag{3.8}$$

which is proportional to the autocorrelation time defined in equation (3.2) and the intensity $\langle E(0,0)^2\rangle$ of the turbulent field for $K \ll 1$, or by using expression (3.1), it becomes a function of the Kubo number. Contrary to Brownian motion, where diffusion occurs in the real space x, diffusion of charged particles in a $1D$ turbulent electric field occurs in the velocity space v.

3.2.3 Resonance broadening

The diffusion coefficient D_0, as given in equation (3.8), depends on two parameters: the amplitude of the electric field and the velocity of the particle trajectories. As the amplitude of the field increases, the assumption of an unperturbed motion is no longer valid. The number of modes able to interact strongly with the particle increases, leading to more complex dynamics. However, interactions between particles and waves remain local, in the sense that only waves in a range $\Delta v = \left(D_0(v)/k(v)\right)^{1/3}$ about v induce chaotic diffusion, while the other ones act perturbatively [Dupree, 1966; Bénisti and Escande, 1998]. This locality can help to understand intuitively that the diffusion picture remains valid for moderate amplitude [Bénisti and Escande, 1997]. The widening of the resonant region is considered in resonance broadening theory [Dupree, 1966; Ishihara et al., 1992; Hirose and Ishihara, 1999].

To account for this widening of resonance region and correct the diffusion coefficient, resonance broadening theory [Doveil and Grésillon, 1982] suggests computing the diffusion coefficient through an iterative procedure. At step n, the diffusion coefficient calculated in the previous step $n-1$ is used to calculate a broadening probability distribution

$$P_{n-1}(v,x,t) = \left[2\pi\sigma_{x,n-1}^2\right]^{-1/2} \exp\left[-\frac{(x-vt)^2}{2\sigma_{x,n-1}^2}\right] \tag{3.9}$$

which substitutes the Dirac distribution function in equation (3.2). The position standard deviation $\sigma_{x,n-1}^2$ at the $n-1$ iteration is defined by

$$\sigma_{x,n-1}^2 = \frac{2}{3}t^p D_{n-1}^{RB}(v) \tag{3.10}$$

where D_{n-1}^{RB} is the resonance-broadening diffusion coefficient defined in equation (3.11), and $p \in]2, 4[$ is a real number that gives the time-dependence of the position standard deviation. The value of this parameter is discussed in section 3.4.3.

This procedure yields the resonance broadening diffusion coefficient at step n from the point of view of particles initially at v:

$$D_n^{RB}(v) = \frac{q^2}{m^2} \int_0^{+\infty} dt \int_{-\infty}^{+\infty} dx P_{n-1}(v, x, t) \langle E(0,0) E(x,t) \rangle \tag{3.11}$$

At step $n = 1$, $D_0^{RB}(v) = D_0(v)$ is calculated in equation (3.8) from linear orbits. This iterative method converges rapidly (typically in a few iterations) towards a resonant broadening diffusion coefficient $D_\infty^{RB}(v)$.

In resonance broadening, the characteristic time τ_{RB}[Dupree, 1966; Cary et al., 1990; Bénisti and Escande, 1997] is defined as

$$\tau_{RB} \sim \left(\frac{k^2 D_0}{6} \right)^{-1/3} \propto K^{-4/3} \tag{3.12}$$

where D_0 is the quasi-linear regime diffusion coefficient, and k the resonant wave number.

Note that, if the autocorrelation function is given, one can solve the quasi-linear diffusion (3.8), and resonance broadening diffusion (3.11). However, when the autocorrelation is not analytical, one can solve these equations in Fourier space. Indeed, since we study homogeneous steady-state turbulence, and particle trajectories are well inside the chaotic domain, then Boltzmann's ergodic hypothesis [Boltzmann, 1895] tells us that ensemble and space averaging are equal $\langle \cdot \rangle = \langle \cdot \rangle_x$ [Brandon et al., 1995]. Consequently, one can solve this equation by transforming the autocorrelation to a sum over the wavenumber k using a Fourier transformation of the electric field $E(x, v)$, and Parseval's identity to solve the space integral. Therefore, after a few calculations, equations (3.8) and (3.11) become respectively,

$$D_0(v) = \frac{q^2}{m^2} \int_0^{+\infty} dt \sum_k \frac{\hat{E}_k^{\,2}}{2} \cos\left[(kv - \omega)t\right] \tag{3.13}$$

$$D_n^{RB}(v) = \frac{q^2}{m^2} \int_0^{+\infty} dt \sum_k \frac{\hat{E}_k^{\,2}}{2} e^{-\frac{\sigma_{x,n-1}^2 k^2}{2}} \cos\left[(kv + \omega)t\right] \tag{3.14}$$

where the integrand in equation (3.13) corresponds to the autocorrelation function of the electric field $\langle E(0,0)E(x,t) \rangle$, the integrand in equation (3.3). First note that equation (3.13) and equation (3.14) look similar except for a coefficient and sign difference in the cosine term. Indeed, the coefficient corresponds to the Fourier transform of the probability distribution P_{n-1} from equation (3.9), and the sign in front of ω appears as the space integral is developed, and by assuming a symmetric dispersion relation, one can show in the QL limit that eq. (3.14) becomes eq. (3.13).

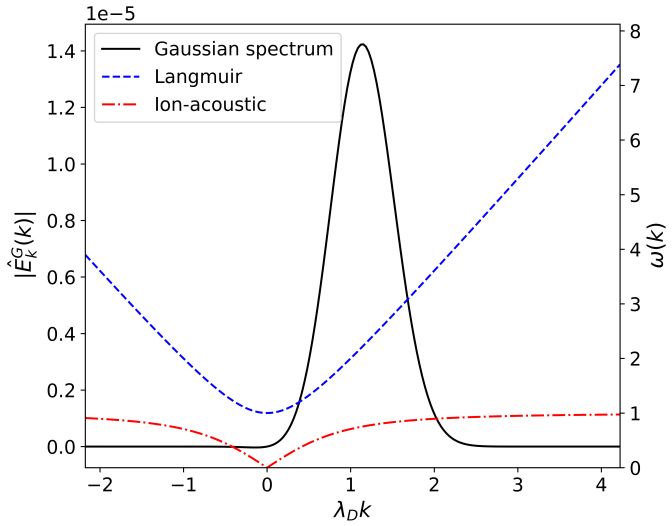

Figure 3.1: Turbulent electric field characteristics: In solid line wave number spectrum from equation (3.17), in blue dashed line the Langmuir wave dispersion relation, and in red dash-dotted the ion-acoustic wave dispersion relation, with arbitrary amplitude a_0 and parameters $\lambda_D k_0 = 1$, $\lambda_D \delta k = 0.4$.

3.3 Application to plasma waves

Generally, when studying plasmas, a self-consistent approach is preferred, where both the electric field and distribution function are solved simultaneously through the self-consistent Vlasov-Poisson system. However, this study focuses on the effects of a prescribed turbulent electric field on particle dynamics. Therefore a test particle approach is preferred. Note that this approach is simpler than the self-consistent problem that led to the development of QL theory; nevertheless, quality information can be gathered through this method.

3.3.1 Dispersion relation and amplitude electric field

For one-dimensional plasma, two ubiquitous waves are the Langmuir plasma wave and ion-acoustic wave (IA). Their respective dispersion relations are

$$\omega^L(k) = \sqrt{\omega_p^2 + 3v_{th}^2 k^2} \tag{3.15}$$

$$\omega^{IA}(k) = \sqrt{\frac{c_s^2 k^2}{1 + \lambda_D^2 k^2}} \tag{3.16}$$

where ω_p, λ_D, and c_s are the electron plasma frequency, Debye length, and ion sound velocity, respectively. We choose to study both Langmuir and ion-acoustic waves since they have qualitatively distinct properties regarding the evolution of frequency (constant for small k and linear for large k for Langmuir and opposite for ion-acoustic waves), resulting in a broad vision of the phenomena present in a one-dimensional plasma.

In this paper we chose a simple Gaussian amplitude spectrum $\hat{E_k}^G(k)$ [Doveil and Grésillon, 1982] defined as

$$\hat{E_k}^G(k) = ka_0\sqrt{\frac{2}{\delta k\sqrt{\pi}}}\exp\left[-\left(\frac{k-k_0}{2\delta k}\right)^2\right] \tag{3.17}$$

where k_0, δk^2, and a_0 are the mean wavenumber, variance, and amplitude of the electric field spectrum, respectively. Figure 3.1 shows the typical dispersion relation functions and Gaussian spectrum of arbitrary amplitude, used in this paper as a function of the wavenumber k.

3.3.2 Test particles in a prescribed turbulent electric field

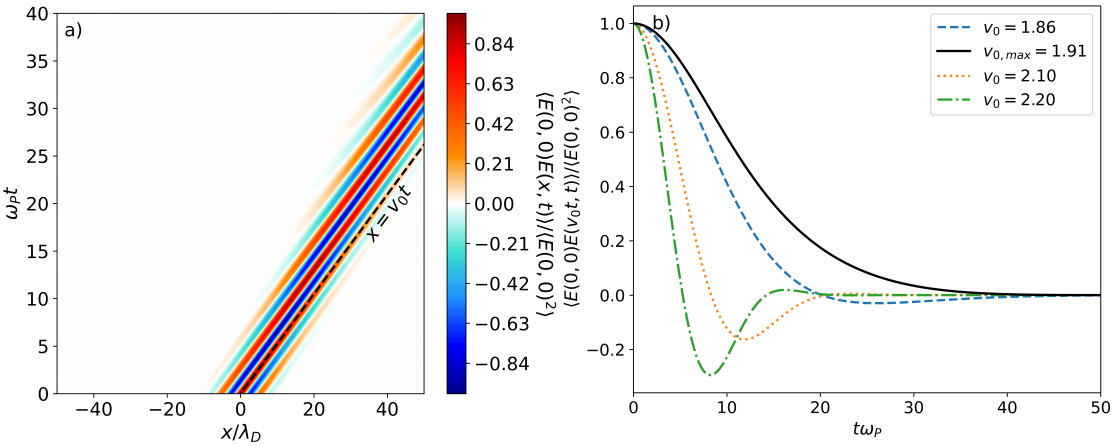

Figure 3.2: Correlation function of the electric field with Langmuir dispersion and for a spectrum with parameters $k_0 = 1$, $\delta k = 0.4$, $M = 201$ and $a_0 = 8.0 \times 10^{-4}$. (a) Correlation as a function of time and distance, dashed diagonal line for $x = v_{0,\max}t$, where $v_{0,\max}$ corresponds to the velocity where QL diffusion is maximal. And (b) correlations functions at $x = v_0 t$ for different velocities v_0.

The numerical study of test particle trajectories requires us to prescribe a "turbulent" electric field. In other words, the modes of the electric field have random phases.

In this paper, the electric field is chosen to be a sum of M sinusoidal modes with random phases, defined as

$$E(x,t) = \sum_{j=1}^{M} \hat{E_k}^{G} \sin(\omega_j t - k_j x + \beta_j) \tag{3.18}$$

where k_j is the wave number distributed uniformly between $[-2.2, 4.2]$, the standard deviation of the k distribution $\delta_k = 0.4$, and the mean $k_0 = 1$, all in units of λ_D. ω_j is the frequency from equations (3.15) and (3.16), and β_j the initial random phase uniformly distributed between $[0, 2\pi[$ of the j-th mode. $\hat{E_k}^{G}$ is the amplitude function of each mode, in our case defined by equation (3.17) and plotted in figure 3.1. Since this electric field is discrete in the reciprocal space (M modes), it possesses a periodicity length of $L = 2\pi/\Delta k$, where $\Delta k = k_i - k_{i-1}$ is the constant interval of k discretization. In the following sections, turbulence refers to a large number of overlapping modes, with random phases, of the electric field.

Figure 3.2(a) shows, in the case of Langmuir dispersion, an example of the autocorrelation function which corresponds to the integrand term in equation (3.13), plotted as a function of the displacement in time t and space x, for a discrete spectrum with $M = 201$ modes. The black dashed diagonal with equation $x = v_{0,\text{max}}t$ shown in figure 3.2(a); note that $v_{0,\text{max}}$ corresponds to the velocity of maximum-diffusion, which will be discussed later in this section, graphically it aligns with the monotonous curve of origin $(x = 0, t = 0)$. Figure 3.2(b) shows different autocorrelation functions at different velocities as a function of time, in particular the maximum-diffusion autocorrelation (black solid line). As observed in both figures, the autocorrelation function is a smooth, continuous, and non-monotonic function (only for $v_{0,\text{max}}$ the function is monotonic), which converges to zero for large values of the time. These properties allow for simple numerical integration and, therefore, calculation of diffusion coefficients, equation (3.13).

Since the electric field is periodic, the autocorrelation function also presents a periodicity in both space and time directions called echoes. In our case, we chose the number of modes and spacing Δk such that these echoes are located far apart and do not interfere with the integration of the autocorrelation function. Moreover, as shown in the previous section 3.2.3, we calculate the diffusion coefficients by integrating the autocorrelation function over time. Numerically, we transform the indefinite integral to a definite integral with a finite upper bound as long as the autocorrelation goes to zero after a few ω_p^{-1}, which is the case for Langmuir and ion-acoustic dispersion relations (shown in figure 3.2(b) for Langmuir dispersion).

To compare against theory, we study the dynamics of test particles in the prescribed turbulent electric field. We developed an algorithm that calculates N particle trajectories using a fourth-order Runge-Kutta algorithm in the prescribed electric field. At $t = 0$, N test particles are initialized with random velocities $v_{0,i}$ and positions $x_{0,i}$.

Notably, particle velocities are distributed in a narrow Gaussian probability around a mean velocity v_0. Particle positions are distributed uniformly in one periodicity interval of the electric field $[0; L[$. Every time step, trajectory diagnostics are computed, such as: particle distributions, statistical moments, and the maximum finite-time Lyapunov exponents.

For each simulation, two quantities are computed: The velocity-diffusion coefficient D by measuring the initial slope of the velocity variance σ_v^2, and the p parameter of equation (3.10) by measuring the time dependence of the spatial variance σ_x^2. More details are given in section 3.4.4 and section 3.4.3, respectively.

3.3.3 Single particle trajectories and trapped particle time

As presented in section 2.1.2, in a simple sinusoidal electric field, the movement of a charged particle is known to be an oscillation in time and space. This trajectory can be represented in phase space (x,v) as either closed trajectories or oscillating open trajectories as shown in figure 2.1, named *Trapped particles* and *Passing particles*, respectively. Since trapped particle trajectories are closed in phase space, one can define a characteristic time/frequency for which it takes a particle to complete one orbit τ_b/ω_b, named bouncing time/frequency. A simple expression of the bouncing time for deeply trapped particles is defined as a function of the wave number and electric field amplitude (k and E) as

$$\tau_b = 2\pi\sqrt{\frac{m}{|q|kE}} \tag{3.19}$$

and the corresponding bouncing frequency $\omega_b = 2\pi/\tau_b$. Note that this section's electric field is expressed as a sum of sinusoidal waves; therefore, we chose a definition of bouncing time/frequency where the product kE from equation (3.19) is replaced by $< k^2 E(0,0)^2 >^{1/2}$. Note that alternatively, one can use $k < E(0,0)^2 >^{1/2}$ where k is either the average wave number $(k = k_0)$ or the wave number from the resonant mode $(k = k_j)$, however, for the values used in this chapter, these only give variations on the bouncing time of less than 15%.

Two examples of test particle trajectories in turbulent electric fields of low and high amplitude, respectively shown in figures 3.3(a) and 3.3(b). As prescribed by quasi-linear theory, trajectories in a low amplitude electric field (small Kubo number), figure 3.3(a), follow Brownian-like motion in phase-space. On the other hand, in a large amplitude field (large Kubo number), figure 3.3(b), particles are trapped in potential wells and follow closed orbits in phase-space, which get disrupted occasionally when particles jump to a neighbor potential well, reminiscing of random-walk motion of the centers of trapped-particle trajectories. Nevertheless, on average, particle trajectories are randomized after several bounce times τ_b due to the turbulent field. This randomization allows us to calculate statistics on particle trajectories such as statistical moments, the

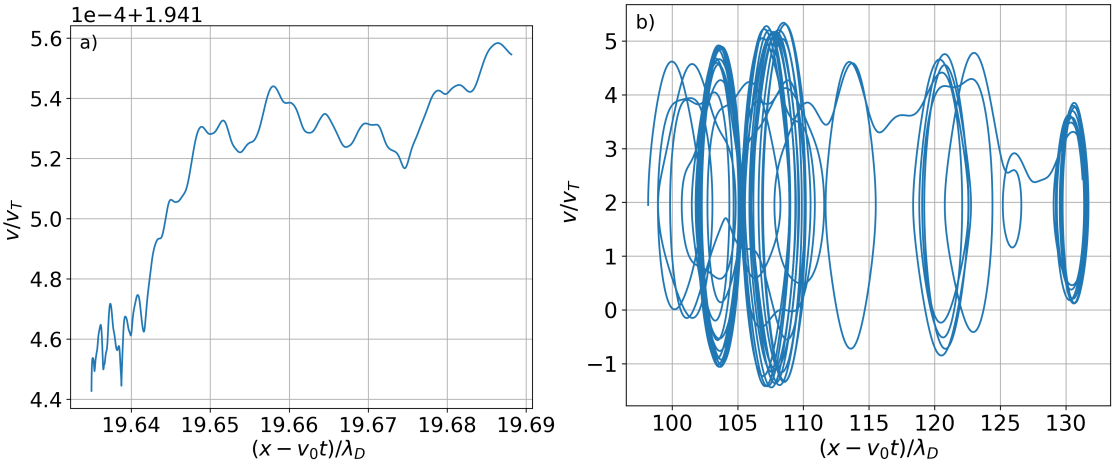

Figure 3.3: Example of particle trajectories in the wave reference frame$x_i - v_{0,i}t$ and v_i, for a small $K = 1.3 \cdot 10^{-3}$ (a) and large $K = 4.0$ (b) Kubo number.

maximum finite-time Lyapunov exponents (FTLE), and in the case of our study, diffusion coefficients.

3.4 Diffusion diagnostics

3.4.1 Statistics on particle trajectories

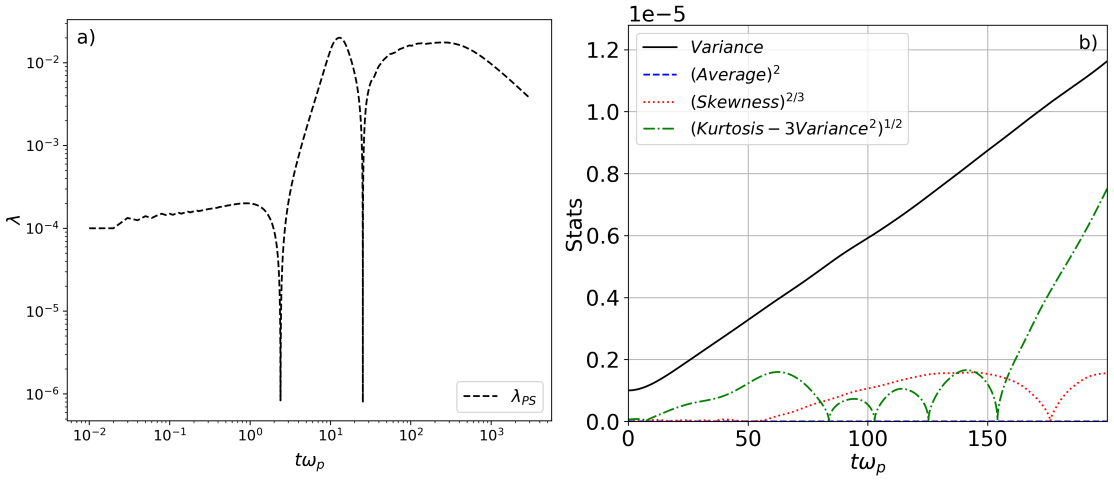

Figure 3.4: Plots of the maximum finite-time Lyapunov exponent in (a), and the first four statistical moments in (b), for an arbitrary simulation with $N = 480\ 000$ test particles.

As stated in section 2.2.1, during a simulation, our code calculates different statistical quantities, particularly the first four velocity moments (Mean difference, variance, skewness, and kurtosis), the spatial and velocity distributions, the FTLE, and the standard velocity deviation σ_v^2 of equation (3.6). In particular, the first three quantities (moments, distribution, and FTLE) allow us to determine the regime of transport particles follow in the turbulent electric field.

For the transport generated by the electric field to be considered to be diffusion, these quantities should respect some rules:

- First, the FTLE can tell us if the transport is stochastic if, in the limit of long times ($t \to +\infty$), the exponent is positive. In this paper, we define the FTLE as [Benettin et al., 1976],

$$\lambda = \frac{1}{t_n - t_0} \sum_{i=1}^{n} \ln\left(\frac{d(t_i)}{d_0}\right) \tag{3.20}$$

where d_0 and $d(t_i)$ are the distance separating two trajectories at $t = 0$ and $t = t_i$ respectively. Figure 3.4(a) shows the FTLE as a function of time. For short and intermediary times, λ_{PS} is positive and grows until it reaches a maximum where it remains for a couple of τ_b. This is followed by a decrease in the FTLE for large times, outside the time scales of any simulation performed in this paper. Consequently, we can consider particle trajectories as stochastic in the initial time interval, where the FTLE is finite and positive. However, after $t\omega_p \sim 500$, λ_{PS} decreases and seems to converge to a negative power of time; however, it remains one-two orders of magnitude larger than the initial FTLE. Therefore, we can consider that particle trajectories remain stochastic for simulation times larger than $500\omega_p^{-1}$.

- Second, since particles are initialized with a Gaussian velocity distribution around v_0, a pure, homogeneous diffusion will only lead to an increase in particle distribution variance, while the other moments should stay null. However, since diffusion is a function of particle velocity (equations (3.13) and (3.14)), one would expect the development of an asymmetry in the distribution of particles, increasing the amplitude of moments other than the variance. Nevertheless, if these moments remain small with respect to the variance, and as long as the standard deviation remains much smaller than the scale of variation of $D(v)$ then the transport generated by the electric field can be considered as a diffusion. Figure 3.4(b) shows the evolution of the first four velocity moments as a function of time for an arbitrary simulation with a small Kubo number (The same results are found for a large Kubo number). We observe that at the start of the simulation, the variance remains considerably larger than the other three moments, until at $t\omega_p = 155$, the kurtosis increases and becomes significant.

Hence, the transport generated by a turbulent electric field of the form presented in section 3.3.1 leads to the stochastic diffusion of particles in a time interval of several τ_0. For later times we can not guarantee that the transport is diffusive.

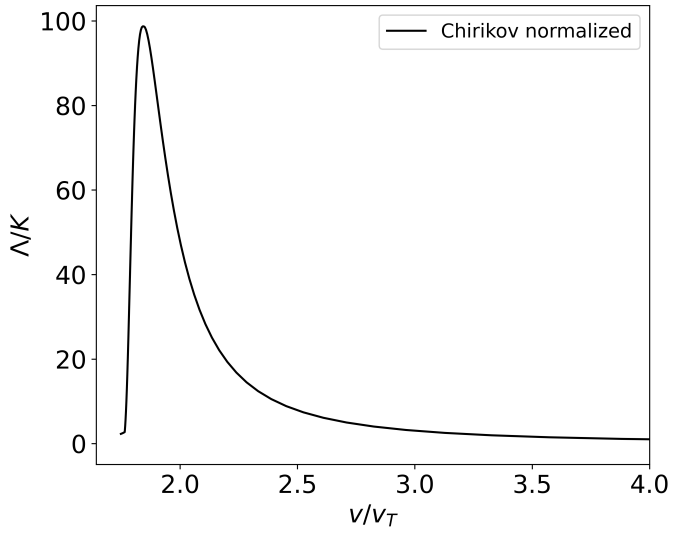

Figure 3.5: Velocity distribution of the local Chirikov overlap criterion Λ, normalized to the Kubo number K.

3.4.2 Chirikov overlap criterion

The Chirikov parameter or Chirikov resonance-overlap criterion [Chirikov, 1960] measures the ratio of superposition of two neighboring waves to characterize the chaotic motion in deterministic Hamiltonian systems. Mathematically it is defined as,

$$\Lambda = \frac{\Delta^{1/2} v_i + \Delta^{1/2} v_{i+1}}{\Delta v^{\phi}_{i,i+1}} \tag{3.21}$$

where $\Delta^{1/2} v_i = \sqrt{\frac{2qE_i}{mk_i}}$ is half of the maximum width of the separatrix along the velocity direction, here E_i and k_i are the $i-th$ mode electric field amplitude and wave number. And $\Delta v^{\phi}_{i,i+1}$ is the difference between the i and $i+1$ modes phase velocities.

For regular dynamics, the Chirikov criterion takes values much lower than unity $\Lambda \ll 1$, and for chaotic dynamics $\Lambda \geq 1$. For values closer to unity, $\Lambda \lesssim 1$, the width of the chaotic domain in phase space is smaller compared to the case where it is $\Lambda \gtrsim 1$. For example, at $\Lambda = 0.5$, the chaotic region will be narrow and localized near the separatrix, and for $\Lambda > 1$, the chaotic region will become significant, encompassing the whole domain.

Figure 3.5 shows the velocity distribution of the local Chirikov overlap criterion normalized to the Kubo number. We choose to normalize the Chirikov criterion by the Kubo number since, for two arbitrary waves, the numerator is proportional to the square amplitude of the electric field, in other words, $\Delta^{1/2} v_i \propto \sqrt{E}$ which is the same dependence as the Kubo number $K \propto \sqrt{E}$. Note that the Chirikov distribution is

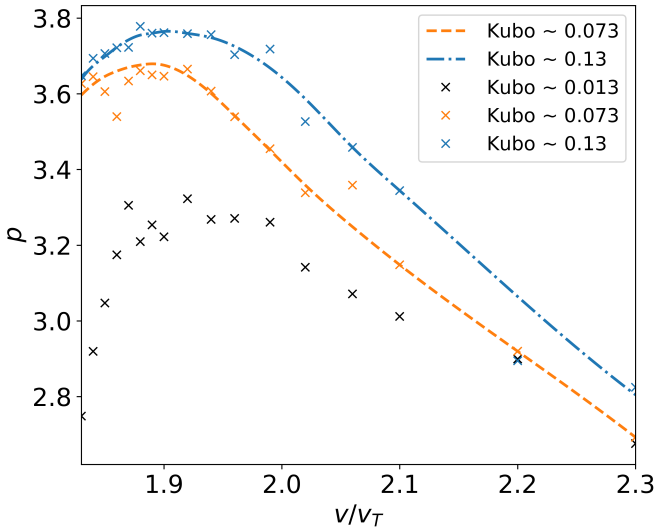

Figure 3.6: The resonance broadening p parameter distribution as a function of particle velocity for three values of Kubo number, Gaussian amplitude, and Langmuir dispersion relation.

comparable to the QL diffusion coefficient of the figure 3.9(a); it is a bell-shape function with a maximum at $v \sim 1.9 v_T$ and a tail that approaches zero as v/v_T increases.

3.4.3 Resonance broadening p parameter

In resonance broadening theory, the p parameter describes the evolution of the position standard deviation as the p power function of time, defined in eq. (3.10). Analytically, p is expected to converge to $p = 3$ when $t \to +\infty$. Indeed, Dupree [Dupree, 1966] shows in equation (7.1) that for the self-consistent kinetic problem, $p = 3$ is a solution. Moreover, Doveil and Grésillon [Doveil and Grésillon, 1982] define the asymptotic p as such. However, a measurement of their σ_x^2 from numerical simulations was not performed.

In our simulations, we observed the p parameter to fluctuate in the interval $]2, 4[$, and indeed for large enough times to converge to $p = 3$. However, the diffusion regime of a simulation is located in the time interval of several τ_0, as shown in section 3.4.1. Therefore, we measured and characterized the p parameter for different Kubo numbers and initial velocities. The results are plotted in figure 3.6.

Figure 3.6 shows the numerical p parameter against velocities for the Langmuir set of simulations. First, we observe that this p parameter is not constant over particle velocities for the three values of the Kubo number, and it takes values varying around $p = 3$, which corresponds to the asymptotic value of p for large enough times [Dupree,

1966; Doveil and Grésillon, 1982]. The dashed curves in figure 3.6 show the smoothed out distribution function of p used to compute the analytical resonance broadening diffusion coefficients in equation (3.14).

We smoothed out the numerical distribution of p (shown in dashed lines) for the analytical resonance broadening diffusion coefficient calculation. This methodology allows us to use resonance broadening in the diffusion regime and compare it against numerical results. Furthermore, as presented in section 3.5.1, we have a qualitative and quantitative agreement between numerical results and theory for the Kubo number of a few percent.

3.4.4 Diffusion estimation: σ_v^2 slope measurement

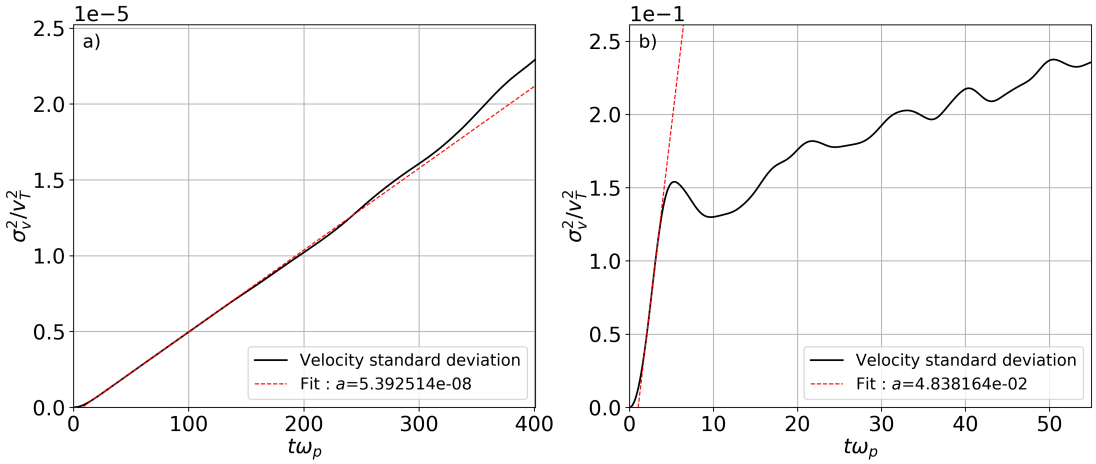

Figure 3.7: In solid lines, the velocity standard deviation as a function of time for two arbitrary simulations with Langmuir dispersion, and in red dashed line, the linear fit in the diffusion regime. In (a) with Kubo number $K = 1.3 \cdot 10^{-2}$. And in (b) with Kubo number $K = 1.3$.

As written in equation (3.7), a diffusion coefficient is defined as the slope of the velocity variance σ_v^2. Therefore, we estimate diffusion coefficients by measuring the linear slope of σ_v^2 over a dozen of τ_0. Figure 3.7, and figure 3.8 show the velocity variance σ_v^2 for a small, medium and large Kubo number in a solid black line, and the linear slope in red dashed line.

Three phases can be observed in the evolution of σ_v^2: In the first phase, where σ_v^2 evolves parabolically. After around one τ_0, a second phase of variable length starts where σ_v^2 grows linearly. Here diffusion is estimated by the measurement of the linear slope in this time interval. Finally, a third phase begins when the first slope of σ_v^2 changes amplitude drastically. However, due to previous arguments, this quantity statistically can not be equated to a diffusion coefficient.

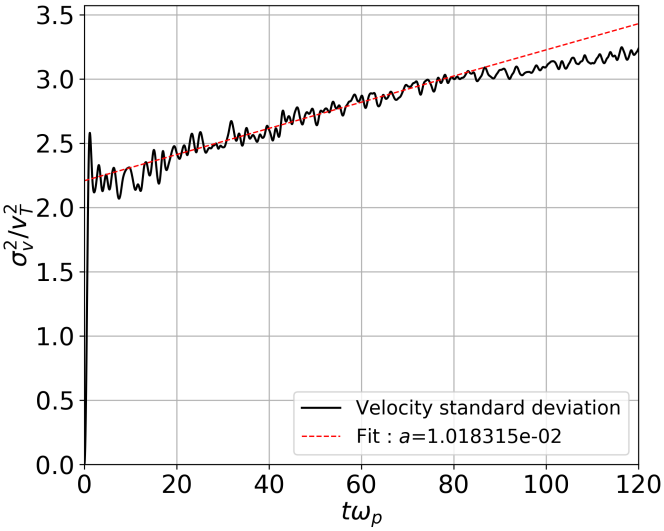

Figure 3.8: In solid line, velocity standard deviation of a typical simulation with Langmuir dispersion at Kubo number $K = 2.7$. The red dashed line is the linear fit during the second slope regime.

3.5 Results

3.5.1 Case of Gaussian spectrum, small Kubo number

First, we focus on the quasi-linear theory regime for Kubo number $K << 1$. We select three different electric field amplitudes a_0, corresponding to $K = [1.3 \cdot 10^{-2}, 7.3 \cdot 10^{-2}, 1.3 \cdot 10^{-1}]$, where $\tau_0 = 12.9\omega_p^{-1}$ and $\tau_0 = 13.1\omega_p^{-1}$ are the Lagrangian autocorrelation time of the electric field at $v_{0,\max}$ calculated from eq. (3.2), for the Langmuir and ion-acoustic dispersion, respectively. And the typical resonance broadening time at $v_{0,\max}$ for the three values of Kubo and the Langmuir dispersion relation are $\tau_{RB}\omega_p \sim [551, 56, 26]$. We perform a series of simulations for each dispersion relation at different particle mean velocities v_0.

The analytical quasi-linear and resonance broadening diffusion is compared against diffusion from numerical simulations in figures 3.9(a) and 3.9(b), for Langmuir and ion-acoustic dispersion simulations, respectively. We find qualitative and quantitative agreement between theory and numerical results for the two dispersion relations and the three values of the Kubo number.

Note that for $K \leq 1.3 \cdot 10^{-2}$, the numerical and resonance broadening diffusion coefficients converge to the quasi-linear diffusion coefficient. On the other hand, resonance broadening effects become significant for Kubo of a few percent ($K \simeq 7.3 \cdot 10^{-2}$, which corresponds to $a_0 \simeq 10^{-3}$ in terms of electric field amplitude). These effects cor-

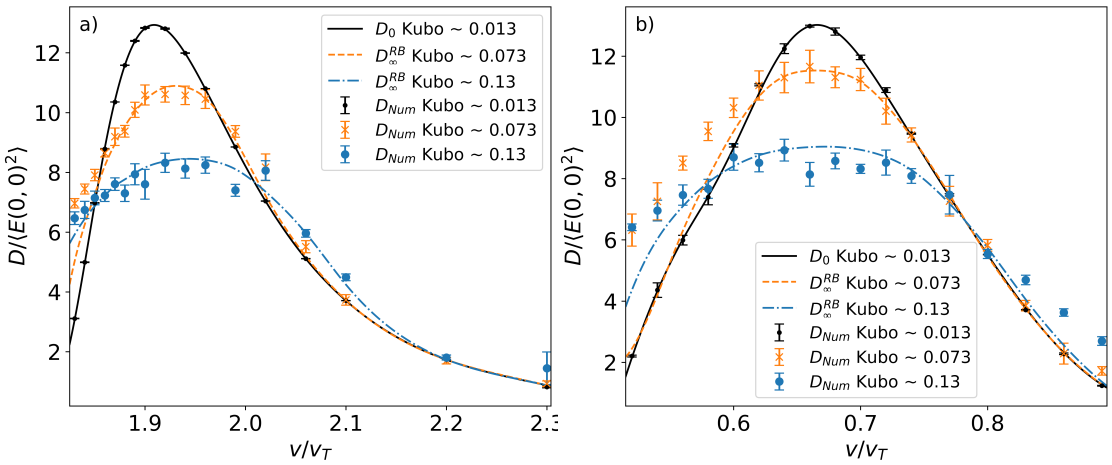

Figure 3.9: Comparison of analytic (solid, dotted, and dashed lines) and numerical (points, crosses, and stars) diffusion coefficients as a function of the initial velocity of particles v for three different initial electric field amplitudes. (a) simulations with Langmuir dispersion relation, and (b) with ion-acoustic dispersion relation.

respond to a flattening of the diffusion curves, an increase in the maximum-diffusion velocity, and an enlargement of the velocity interval where particles diffuse, as explained in section 3.2.3. For these Kubo numbers, particles are partially, or fully trapped in the electric field, therefore, exploring a wider range of velocities around the initial velocity. These variations result in an increase in the number of waves interacting with the particle, but with a limited, relatively local, range. This leads to an effective average operation on the diffusion felt by particles.

Furthermore, the diffusion coefficients are bell-shaped for the chosen dispersion relations. Indeed, the maximum diffusion, located at $v_{0,\max}$, corresponds to the velocity of maximum resonance between waves and particles. This resonance corresponds to the velocity shown as a diagonal in the autocorrelation function in the figure 3.2(a).

From numerical simulations, we observe a broadening and decrease in amplitude of the particle diffusion as expected from resonance broadening theory for Langmuir and ion-acoustic dispersion relations. However, for the ion-acoustic dispersion relation, figure 3.9(b), we observe a difference in diffusion coefficients between resonance broadening theory and numerical simulations. Simulation diffusion is greater than predicted for values at the boundaries of the velocity interval. This effect becomes more noticeable as the Kubo number increases or for less-dispersive waves, such as ion-acoustic waves. This effect is studied in detail in the next section for Langmuir dispersion simulations and high Kubo numbers.

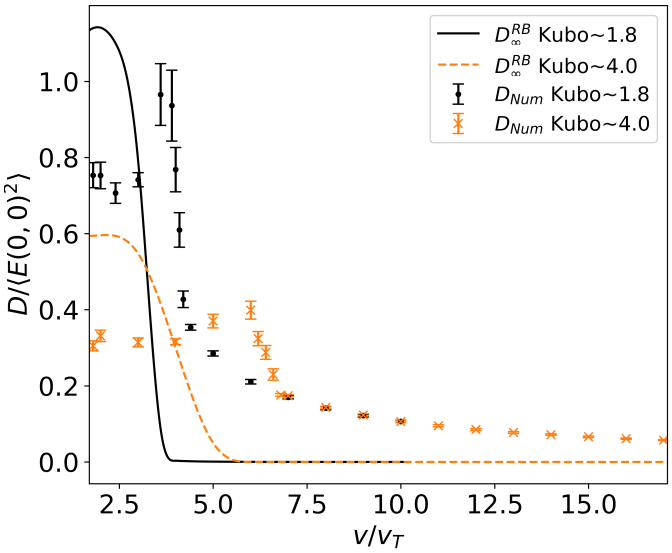

Figure 3.10: Comparison of analytic (solid, dotted, and dashed lines) and numerical (points, crosses, and stars) diffusion coefficients as a function of the initial velocity of particles v for Kubo number of 1.8 and 4.0, with Langmuir dispersion relation.

3.5.2 Large Kubo number

For the second study, we have investigated the evolution of the diffusion coefficient outside the validity range of the quasi-linear theory regime. In other words, for Kubo numbers larger than one ($K \geq 1$) with Langmuir dispersion relation. First, we chose two values of the electric field amplitude corresponding to $K \simeq 1.8$ and $K \simeq 4.0$, respectively. The results are shown in figure 3.10. We find that RB theory predicts the order of magnitude of diffusion for velocities around the resonance velocity ($v < 4v_T$), but a significant discrepancy in the shape of the diffusion coefficient is observed. Note that the ratio between the analytical and numerical diffusion coefficients is not constant and depends on simulation parameters. Furthermore, we measure a significant diffusion from numerical simulations for fast particles, while negligible diffusion is predicted by quasi-linear theory and resonance broadening. Finally, we observe that the diffusion coefficients converge regardless of the Kubo number for particle velocities over $v > 8v_T$ and $K > 1$. Indeed, as explained in section 3.5.1, the electric field is discrete and distributed for the most part around the resonance velocity region of $v < 4v_T$, with a small number of modes located at velocities outside this region. Therefore, a small diffusion coefficient is measured for high enough particle velocities where only two chains of islands overlap. Moreover, as the electric field amplitude increases, the overlap of these few modes increases, and particle stochasticity and diffusion increase, pushing the boundaries of the plateau to higher velocities.

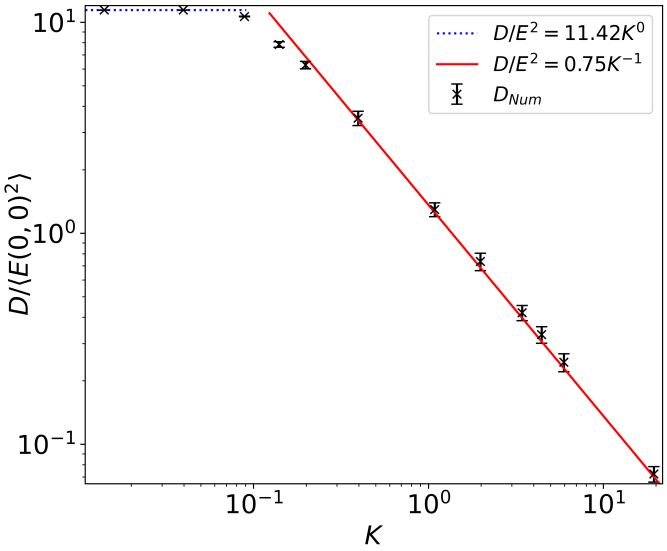

Figure 3.11: Numerical diffusion coefficient in crosses as a function of the Kubo number K, for $v_0 = 1.95$. The power law fit dependence on Kubo number of diffusion is in solid and dashed lines.

We have studied the dependence of the diffusion coefficient as a function of the Kubo number at fixed v_0 in two different time intervals. First, for times of the order of τ_0, figure 3.11 shows the normalized diffusion coefficient from numerical simulations as a function of the Kubo number. We observe three different regimes: For $K \ll 1$, the normalized diffusion is constant as predicted by quasi-linear theory. This is followed by a transition regime where the Kubo number is of the order of a few percent, here the diffusion coefficient decreases non-linearly as observed in the previous section 3.5.1 and predicted by resonance broadening [Doveil and Grésillon, 1982; Hirose and Ishihara, 1999]. And for the case of $K > 0.5$, the normalized diffusion evolves as a power of the Kubo number K^{-1}. Similar results are found for ion-acoustic dispersion relation.

As of the writing of this manuscript, there is no theory or method to predict diffusion in the large Kubo regime accurately. Nevertheless, we observed particle trajectories to resemble those originating from a random walk of the centers of trapped-particle trajectories in velocity space. Therefore we suppose that the diffusion coefficient takes the form $D = \frac{\Delta v^{RW}}{2\Delta t}$. Here we define the elapsed time between jumps as $\Delta t = \tau_b$, the time for a particle to perform one trapped orbit. We define the velocity step to be the resonance broadening [Dupree, 1966] $\Delta v^{RW} = \Delta v^{TB} = (D/6k)^{1/3}$, which corresponds to the range of velocities particles can interact with neighbor electrostatic modes. This approximation shows that for $K \gg 1$ diffusion scales as a power

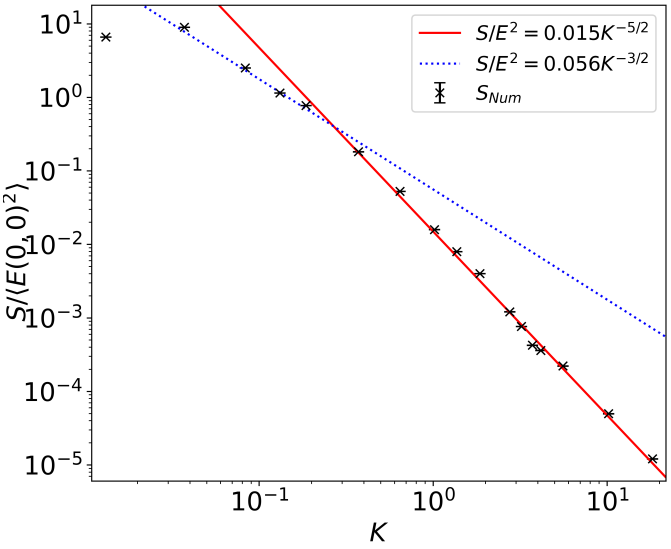

Figure 3.12: Numerical S coefficient in crosses as a function of the Kubo number K after a time much larger than τ_0, for $v_0 = 1.95$. The power law fit dependence on Kubo number of diffusion is in solid and dashed lines.

of the electric field: $D = CE^{3/2}$, where $C = k^3/288$, matching the results of figure 3.11. Note that this expression predicts the proper electric field scaling but may not predict the exact value of diffusion. In our case, by denormalizing the diffusion coefficient and using the second expression of the Kubo number, $K \propto E^2$, our results become: In the quasi-linear regime, D is proportional to $K^4 \propto E^2$, and for large Kubo numbers, D is proportional to $K^3 \propto E^{3/2}$.

Finally, we studied the second slope on σ_v^2 located at times much larger than τ_b and τ_0, as shown in section 3.4.4. In this regime, we measure the first four statistical moments and the maximum finite-time Lyapunov exponent (FTLE) [Benettin et al., 1976; Brandon et al., 1995; Falessi et al., 2015] to characterize the second slope on σ_v^2. First, in the FTLE diagnostic, we observe that for times of the order of a couple τ_b (less than $500\omega_p^{-1}$), the FTLE is positive, and it converges to a plateau. For larger times, we observe that the FTLE starts to decrease with time; this gives us an upper limit in simulation time. Nonetheless, particle trajectories remain stochastic for times larger than $500\omega_p^{-1}$ since the value of the FTLE remains positive and, in particular, one-two orders of magnitude higher than for the initial FTLE. Furthermore, by examining particle statistics and distribution, we observe that the excess kurtosis becomes important compared to the variance at larger times. Moreover, the particle distribution becomes non-Gaussian after the time corresponding to the first slope (see figure 3.4(a)). Thus, this indicates that for longer times, particles do not follow what can be strictly defined

as a diffusion despite measuring a slope on σ_v^2, or in other words, a Hurst parameter of $H \sim 0.5$. Therefore, we name this quantity the slope coefficient S.

In figure 3.12, we show the normalized slope coefficient as a function of the Kubo number. First, we observe that S is several orders of magnitude smaller than in the previous figure 3.11, and we observe two different regimes where S evolves as a power of the Kubo number, a first at a relatively low Kubo number, $K < 0.5$, where $S \propto K^{5/2} \propto E^{5/4}$, and a second for a larger Kubo number, $K > 0.5$, where $S \propto K^{3/2} \propto E^{3/4}$.

3.6 Conclusion

In summary, we investigated the diffusion of charged particles in a prescribed one-dimensional turbulent electric field by means of numerical simulations and quasi-linear theory. We measured statistical diffusion coefficients at different Kubo number values using a Gaussian amplitude spectrum and realistic plasma dispersion relations: Langmuir and ion-acoustic dispersions. First, diffusion at a low Kubo number was investigated as a function of the initial particle velocity. The results from numerical simulations are in qualitative and quantitative agreement with quasi-linear theory, including resonance broadening as well as with previous papers [Doveil and Grésillon, 1982; Hirose and Ishihara, 1999], which studied diffusion at low Kubo numbers and for non-physical dispersion relations. Secondly, a study of diffusion coefficients outside the quasi-linear regime, for large Kubo numbers, was performed as a function of the Kubo number, where we measured diffusion to scale as a power law, $K^3 \propto E^{3/2}$, which we explain to be a random walk diffusion of the centers of trapped-particle trajectories in the velocity direction. And finally, for times much larger than τ_0 and τ_b, we measure two power laws for the evolution of the slope coefficient S in the form of $K^{5/2} \propto E^{5/4}$ and $K^{3/2} \propto E^{3/4}$ for small and large Kubo number respectively.

In conclusion, in the case of realistic plasma dispersion relations and a prescribed turbulent electric field, quasi-linear and resonance-broadening theories in the limit of small Kubo numbers ($K < 10\%$) accurately predict particle diffusion. Remarkably, a simple random walk expression ($D \propto E^{3/2}$), generally employed in other conditions, predicts the evolution for large Kubo numbers $K \gg 1$. However, further work is required to improve the understanding of turbulence, transport, and diffusion. This study is subject to two caveats: Firstly, the incorporation of the Poisson equation to get a complete self-consistent problem where particle distributions are allowed to modify the electric field, and secondly, by considering the evolution of phase-space structures [Bernstein et al., 1957; Berk et al., 1970; Schamel, 1971; Dupree, 1972; Schamel, 1972; Berk et al., 1997; Lesur et al., 2014]. Consequently, the next step of this study is to consider phase-space structures by prescribing a relationship between the initial phases of the electric field modes, as observed in laboratory plasmas [Tsunoda et al., 1987b,a,

1991], and studying the self-consistent (Vlasov-Poisson) kinetic problem.

Chapter 4

Vlasov plasmas and kinetic phase-space structures

Contents

In the second half of the 19th century, Boltzmann developed a statistical description of the behavior of a thermodynamical system out of equilibrium, named the Kinetic theory of ideal gases. This theory assumes that any interaction between particles other than collisions is negligible. But it was not until the early 20th century that the collisionless-Boltzmann equation, also known as the Vlasov equation, was applied to charged particle systems, coupling it with Maxwell's electromagnetic equations. Therefore, unlike the kinetic theory of ideal gases, the kinetic theory of plasmas considers the significant long-range interactions that dominate in high-temperature plasmas.

Nevertheless, most high-temperature plasmas of interest do not strictly follow the Vlasov equation. Plasmas are subject to external forces, small amounts of collisions, and sources or sinks of energy and particles, to citep a few. However, in some cases, these processes' time and space scales allow researchers to separate or neglect them, allowing the approximation of the system by the Vlasov equation.

4.1 Kinetic model: Vlasov-Poisson

In general, the Kinetic model describes the evolution of species s through a $6 + 1$ dimension particle distribution $f_s(\boldsymbol{x}, \boldsymbol{v}, t)$, where $\boldsymbol{x}$, and $\boldsymbol{v}$ are the position and velocity vectors respectively, and t is the time coordinate. The distribution function measures in every point of the phase-space the particle density, such that at an arbitrary time t, $f_s(\boldsymbol{x}, \boldsymbol{v}, t)d\boldsymbol{x}d\boldsymbol{v}$ gives the expected number of particles in a small phase-space volume of size $d\boldsymbol{x}d\boldsymbol{v}$.

The equation reigning over the evolution of the distribution function is known as the Boltzmann equation. It describes the evolution of f_s as a series of convection terms in phase-space plus a collision term. It writes:

$$\frac{\partial f_s}{\partial t} + \boldsymbol{v}\frac{\partial f_s}{\partial \boldsymbol{x}} + \frac{q_s}{m_s}(\boldsymbol{E} + \boldsymbol{v} \times \boldsymbol{B})\frac{\partial f_s}{\partial \boldsymbol{v}} = C_s \tag{4.1}$$

where C_s is the collisional term of species s. However, as mentioned previously, high-temperature plasmas are considered to be collision-less. Therefore, we can neglect the C_s term on the right of the equation, changing the equation's name to the Vlasov equation. And $\boldsymbol{E}$ and $\boldsymbol{B}$ are electric and magnetic fields, given by the Maxwell equations.

4.1.1 One-dimensional equations

Since we study a two-species (ions and electrons) one-dimensional plasma, the Vlasov-Maxwell system of equations is greatly simplified. For this, quantities such as the distribution function or the fields are rewritten as a function of the scalar space x and

velocity v, $f_s(x, v, t)$ and $E(x, t)$ respectively. Following this simplification, it is trivial to deduce that the new 1D system of equations written as,

$$\frac{\partial f_s}{\partial t} + v\frac{\partial f_s}{\partial x} + \frac{q_s}{m_s}E\frac{\partial f_s}{\partial v} = 0\,, \tag{4.2}$$

$$\frac{\partial E}{\partial x} = \frac{e}{\varepsilon_0}\int_{-\infty}^{+\infty}[f_i - f_e]\,dv \tag{4.3}$$

the Vlasov and the Poisson equations of a 1D plasma consisting of electrons and single-charge ions. Where E is the scalar electric field in the direction of the movement, e is the elementary charge, and f_i and f_e are the ion and electron distribution functions.

4.1.2 Equilibrium

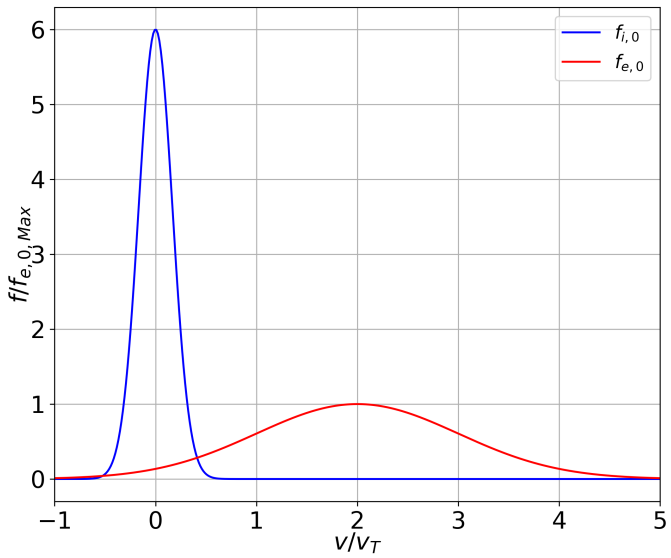

Figure 4.1: Initial equilibrium distribution function of ions (blue) and electrons (red), normalized to the maximum of the electron equilibrium distribution function $f_{e,0,max} = n_{s,0}/v_{e,T}\sqrt{2\pi}$, for a mass ratio of $m_i/m_e = 36$, and a drift velocity of $v_d = 2v_T$.

The equilibrium state of charged particles in the 1D plasma is defined as any solution to the Vlasov-Poisson system, in other words, any couple of f_s and E. One of these equilibriums, and mainly used in this manuscript, is known as a Maxwellian or Gaussian equilibrium. By definition, this equilibrium has no electric field present in

the plasma, and the distribution function is defined as:

$$f_{s,0}(v) = \frac{n_{s,0}}{v_{s,T}\sqrt{2\pi}} \exp\left[-\frac{1}{2}\left(\frac{v - v_{s,0}}{v_{s,T}}\right)^2\right] \tag{4.4}$$

where $n_{s,0}$, $v_{s,T}$ and $v_{s,0}$ are the initial particle density, thermal velocity, and average velocity of species s. In this manuscript, the laboratory frame of reference is that of the ions, in other words, $v_{i,0} = 0$. On the other hand, the average velocity of electrons $v_{i,0}$, also known as the electron drift velocity $v_d = v_{e,0}$, remains a free variable. Moreover, since we study systems near statistical equilibrium, such as those found in stellar plasmas, the electron drift velocity is generally not zero. Figure 4.1 shows the typical equilibrium distribution function of ions and electrons for an artificial mass ratio of $m_i/m_e = 36$ and a drift velocity of $v_d = 2v_T$.

This equilibrium, under certain conditions, is a stable equilibrium. However, for values of the drift velocity larger than a critical value, the system becomes unstable, which leads to an unstable equilibrium where $E \neq 0$. This instability is known as the Current-Driven Ion-Acoustic instability, which has seen considerable interest from scientists in the second half of the $XXth$ century [Kindel and Kennel, 1971; Hasegawa, 1974; Papadopoulos, 1977].

4.2 BGK structures

High-temperature plasmas, such as fusion, ionospheric or astrophysical, can be considered collision-less since the collisional mean-free-path of these plasmas can be considered much larger than the wavelengths of dominant electromagnetic modes. Consequently, particle distributions tend to often deviate from Gaussian distributions. Many studies in collision-less Vlasov plasmas have shown the analytical [Bernstein et al., 1957; Schamel, 1971; Dupree, 1982] and experimental [Roberts and Berk, 1967] existence of self-consistent steady-state nonlinear solutions to the Vlasov-Poisson system of equations known as BGK (Bernstein-Green-Kruskal) structures (or modes) [Bernstein et al., 1957]. They represent nonlinear electrostatic waves that propagate and trap particles of a collision-less plasma. These trapped particles' populations play an essential role in the transport of particles and energy, instability triggering, and disturbance on plasma confinement.

The BGK method, also known as the integral approach method, starts with a given, often physical, electric potential $\phi(x)$ and a distribution of free particles f_{fe}, deriving a distribution of trapped particles. The difficulty with this method is that it does not ensure that the distribution function will be physically meaningful or stable in time. Often it results in undesirable effects like negative values or singularities. To overcome the problems with the BGK method, a differential approach, also known as a pseudo-potential, Sagdeev, or Schamel method/approach, proceeds the inverse way. It imposes

a physically meaningful distribution function, from which the Vlasov-Poisson system is solved to find a self-consistent electric potential.

4.2.1 Schamel model of electron-holes

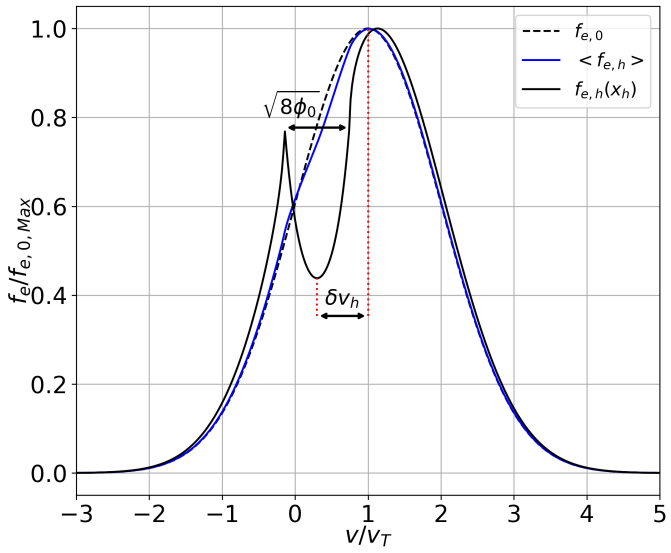

Figure 4.2: Electron Schamel distribution function slice at $x = x_h$ normalized to the maximum of the electron equilibrium distribution function $f_{e,0,max} = n_{s,0}/v_{e,T}\sqrt{2\pi}$, for a mass ratio of $m_i/m_e = 36$, and parameters $\phi_0 = 0.10$, $\beta_h = -5.80$, and $\delta v_{e,h} = 0.70 v_T$.

After Bernstein-Green-Kruskal's formulation, H. [Schamel, 1971] provided a formulation to study time-stable BGK structures. The technique used by Schamel is known as the differential equation technique [Schamel, 1971]. This method divides the total distribution function into two phase-space regions, corresponding to the free and trapped particle distribution function. For a one-dimensional plasma the total particle distribution of species s writes as [Schamel, 1971, 2000; Luque and Schamel, 2005]:

$$f_{s,h}(x,v) = \frac{n_{s,0}}{v_{s,T}\sqrt{2\pi}} \exp \begin{cases} -\frac{1}{2}\left(\frac{\delta v_{s,h}}{v_{s,T}}\right)^2 - \beta_h \frac{E_s}{m_s v_{s,T}^2}, & \text{if } E_s \leq 0 \\ -\frac{1}{2v_{s,T}^2}\left(\sigma_v \sqrt{2\frac{E_s}{m_s}} - \delta v_{s,h}\right)^2, & \text{if } E_s > 0\,. \end{cases} \tag{4.5}$$

where $\delta v_{s,h} = v_{s,0} - v_{h,0}$ is the shift in velocity between the drift velocity $v_{s,0}$ and the initial phase velocity $v_{h,0}$ of the BGK structure, $\sigma_v = \operatorname{sgn}\left(v - \delta v_{s,h}\right)$ is the sign of the velocities difference. β_h is named the trapping parameter corresponding to the

coefficient determining the curvature of the structure: $\beta_h < 0$ is a hole, $\beta_h = 0$ a plateau, and $\beta_h > 0$ for a hump in the distribution. And E_s is the energy of particles from species s in the reference frame of the structure, defined by,

$$E_s(x,v) = \frac{1}{2} m_s \Big(v - (v_{s,0} - \delta v_{s,h}) \Big)^2 + q_s \phi(x - x_h) \, . \tag{4.6}$$

where $\phi(x)$ is the localized electric potential of a Schamel structure of amplitude ϕ_0.

Figure 4.2 shows a slice of the electron distribution functions at the center of the electron-hole $x = x_h$, the Schamel distribution function $f_{e,h}$ and the equilibrium distribution function $f_{e,0}$, for a mass ratio of $m_i/m_e = 36$, and parameters $\phi_0 = 0.05$, $\beta_h = -6.56$, and $\delta v_{e,h} = 0.45 v_T$.

Following the Schamel approach, the particle density obtained from the distribution function from equation 4.5 is used to derive the electric potential $\phi(x)$ by solving the Poisson equation through the Sagdeev potential, or pseudo-potential, method. Following this technique, a family of bell-shaped localized electric potentials can be derived.

4.2.2 Generalized electron structures

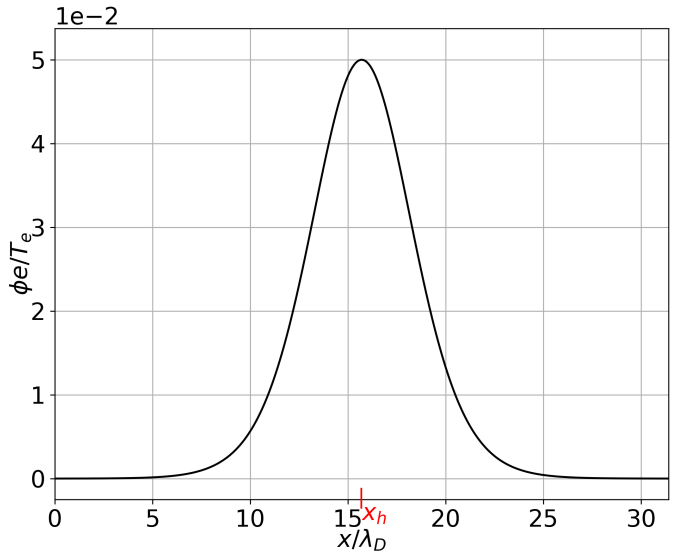

Figure 4.3: Electron-hole Schamel *sech4* hole-potential with amplitude $\phi_0 = 0.05 T_e/e$.

In this manuscript, we focus on the study of electron structures. In particular, we study the dynamics of local electrostatic holes in the electron phase-space. Therefore, in the case of Schamel's theory, ions are considered to be a neutralizing background

species. The ion distribution function, for the purposes of this theory, is defined to be a Maxwellian, in other words, equal to equation 4.4, $f_i(x,v) = f_{i,0}(v)$.

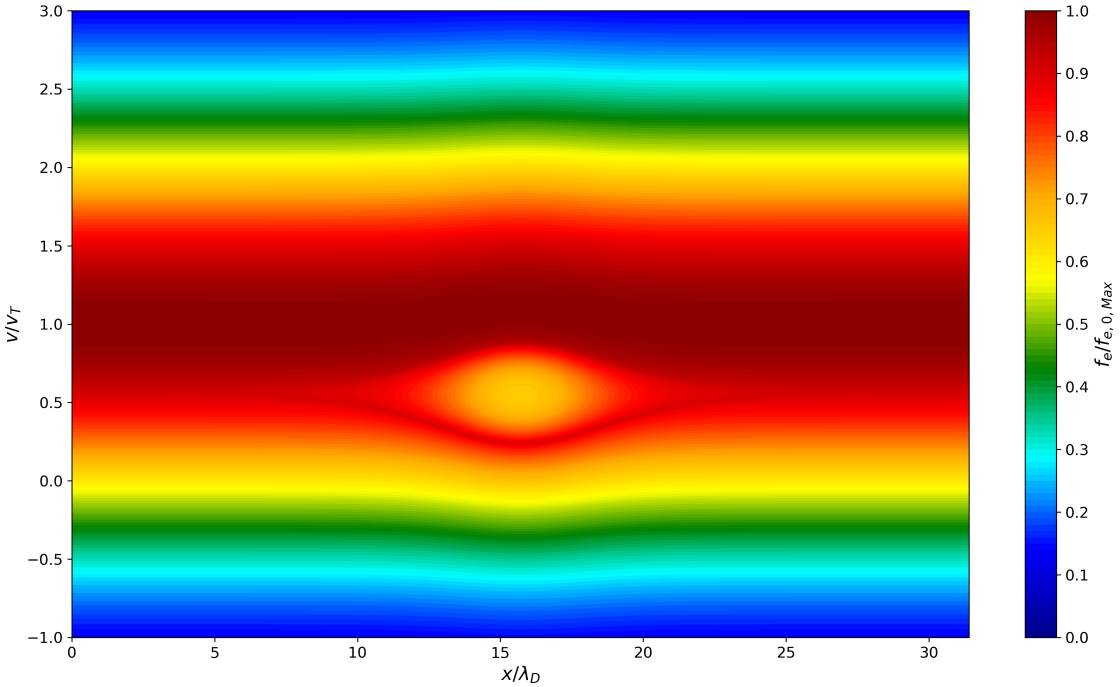

Figure 4.4: Electron-hole distribution function phase-space for a mass ratio of $m_i/m_e = 36$, and parameters $\phi_0 = 0.05$, $\beta_h = -6.56$, and $\delta v_{e,h} = 0.45 v_T$.

Since the ion fluctuations are neglected, the Schamel pseudo-potential method leads to the derivation of a solitary electric potential pulse characterized by electron trapping. In this manuscript, this structure is referred to as *sech4* defined as:

$$\phi(x) = \phi_0 \operatorname{sech}^4\left(\frac{x - x_{h,0}}{\Delta x_h}\right) \tag{4.7}$$

where ϕ_0 is the electric potential amplitude, $x_{h,0}$ is the initial position of the structure, and Δx_h the structure characteristic width defined by the hole parameters, as:

$$\Delta x_h = \sqrt{\sqrt{\frac{\pi}{\phi_0}} \frac{15 \exp\left(\delta v_{s,h}^2/2\right)}{\left(1 - \beta_h - \delta v_{s,h}^2\right)}} \tag{4.8}$$

Figure 4.3 shows the typical Schamel *sech4* electric potential for an electron-hole in phase-space from equation 4.7. The *sech4* is a bell-shaped function with a maximum $\phi = \phi_0$ at $x = x_h$, where the skirts converge to $\phi = 0$ in the limit $|x - x_h| \to +\infty$.

Figure 4.4 shows an arbitrary Schamel electron-hole distribution function in phase-space (x, v). As observed, at distances much larger than Δx_h, in other words, away from the electron-hole center, the distribution function is equal to the equilibrium distribution from equation 4.4. Note that the size of electron-holes in the velocity direction is equal to $\sqrt{8\phi_0}$ in units of electron thermal velocities.

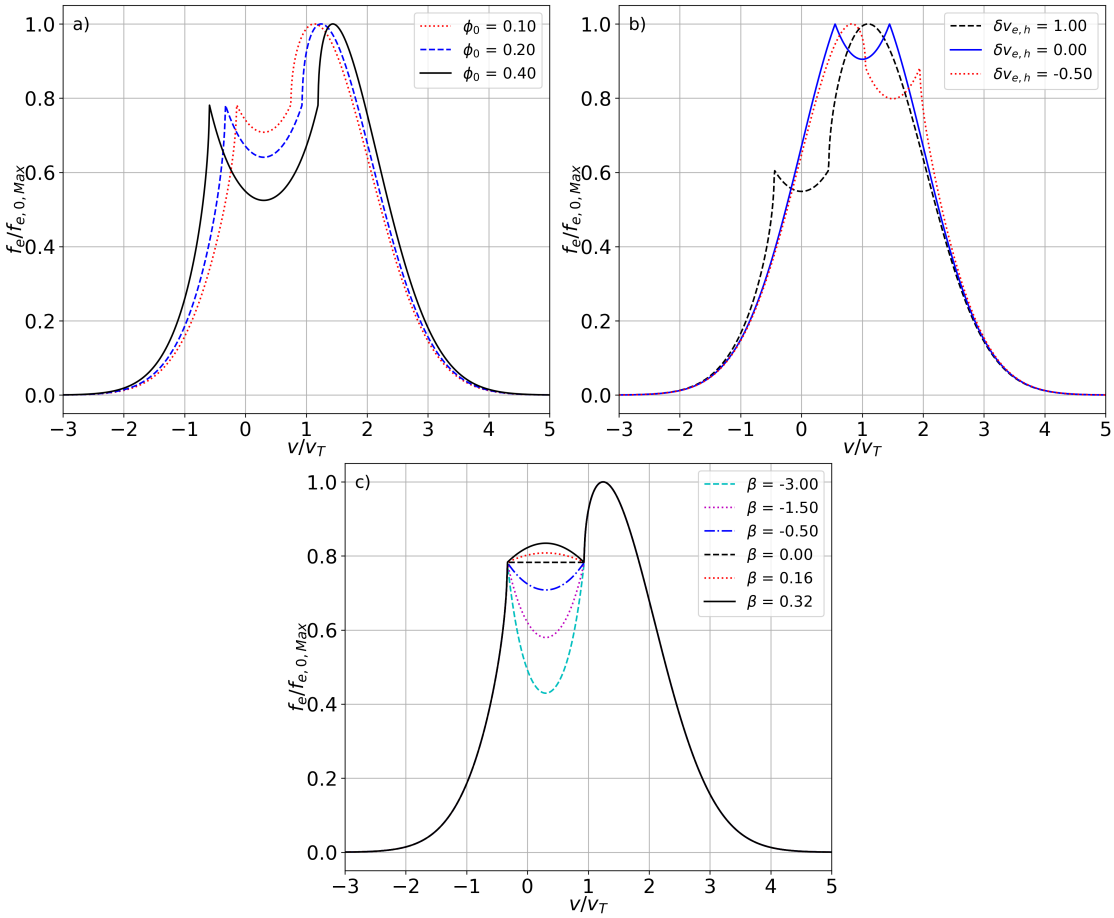

Figure 4.5: Schamel electron-hole slices at $x = x_h$ for different parameter values. In $a)$ three different values of ϕ_0, in $b)$ four different values of hole velocity $\delta v_{e,h}$, and in $c)$ multiple values of β_h.

Figure 4.5 shows three different figures with different, arbitrary Schamel electron distribution function values. In $a)$, three different values of the amplitude of the electric potential ϕ_0 are plotted. This parameter modifies both the velocity size of the hole as well as the depth of the hole. In $b)$, three values of the electron-hole velocity $\delta v_{e,h}$ are shown: one value for a negative $\delta v_{e,h}$, one at the electron drift velocity and one at positive $\delta v_{e,h}$. And finally, in $c)$, six values of β_h are plotted, three for negative β_h, which represents a hole, one for $\beta_h = 0$ corresponding to a plateau, and finally two

for positive β_h corresponding to a hump.

In summary, a *sech4* structure is defined through three parameters: ϕ_0, β_h, and $\delta v_{s,h}$, where two are independent parameters. In our simulations, we chose the independent parameters to be ϕ_0 and $\delta v_{s,h}$, while β_h is calculated from the quasi-neutrality condition of the plasma. This method is explained in more detail in section 4.3.3.

4.3 Implementation of numerical code

4.3.1 Kinetic code: COBBLES

In order to study the dynamics of Schamel *sech4* electron-holes in a two-species plasma, we use the self-consistent Kinetic electrostatic code **COBBLES** [Lesur et al., 2006b; Lesur, 2010]. **COBBLES** is an initial value problem solver which solves the one-dimensional Kinetic Vlasov-Maxwell system of equations using a semi-Lagrangian method [Durran, 1999] trough a Cubic-Interpolated-Propagation scheme in a form which conserves exactly elements of phase-space, and splitting method [Nakamura et al., 2001]. **COBBLES** is written in FORTRAN 90 language parallelized using MPI. It was developed by Maxime Lesur [Lesur et al., 2006b; Lesur, 2010] to solve the Vlasov-Poisson system for the Landau Damping and Berk-Breizman problems and ion-acoustic turbulence.

A semi-Lagrangian scheme consists in solving the system of equations on a fixed grid of points by using interpolated trajectories of particles at the previous time-step. At each iteration, the **COBBLES** solves different parts of the Vlasov-Poisson system separately. First, for a half-time-step $\Delta t/2$ it solves the position-space advection therm, followed by the collisional and source terms, and lastly, it solves the Poisson equation. Secondly, for a full-time-step Δt, the code solves the velocity-space advection term of the Vlasov equation with the newly calculated species distribution function f_s. And finally, the first three steps are repeated backward for another half-time-step $\Delta t/2$, the Poisson equation, followed by the collision and source terms, and the position-space advection. In summary, after one time-step, **COBBLES** calculates the new distribution function for each species and new electric field.

4.3.2 Implementation problems: density and periodicity

At the initial time, the **COBBLES** code defines two distribution functions for electrons f_e and ions f_i inside a box of length L_x and periodic in the position-direction and discretized by a grid of points of size $N_x \times N_v$, where N_x and N_v are the numbers of points in the position and velocity spaces respectively. Two conditions are required for the code to function: The first one is that all particle distributions must be small enough at the edges of the velocity direction. This can be achieved by defining the distribution function as a bell-shaped curve like the Maxwellian distribution and by

choosing an adequate maximum and minimum velocity on which the cutoff of the distribution occurs. And secondly, the global quasi-neutrality condition of the plasma inside the periodic box must be satisfied.

To study the simulated plasma, we add a perturbation to the distribution function. This perturbation in **COBBLES** is initialized in three different ways: First, by sinusoidal waves with wave number $2\pi/L_x$, secondly by creating a local deficit of phase-space density, or thirdly, in the context of the present work, I implemented the initialization of a Schamel phase-space hole. All these three methods need to verify the global quasi-neutrality condition of the plasma.

For the sinusoidal wave, the global quasi-neutrality condition is naturally achieved by choosing a wave mode with the same periodicity as the box. However, the other two perturbations require numerical adjustments, such as re-normalizing one of the species distribution functions to fulfill global quasi-neutrality. While, in principle, re-normalizing one of the distribution functions solves the global quasi-neutrality problem, this does not solve an inherent problem that any plasma at electrostatic equilibrium is defined to have no local electrostatic field. Indeed, this definition becomes a problem when studying phase-space holes with a periodic plasma with numerical simulations since the plasma must remain at equilibrium far away from the phase-space hole. Re-normalizing one of the distribution functions creates a small constant charge in those regions, generating a linear electric field and electric potential.

Therefore, to study the dynamics of phase-space holes, one needs to find a distribution function that allows for a local deficit of phase-space density while allowing for a neutral plasma far away from the perturbation. In the case of a Schamel *sech4* phase-space hole, the parameter β_h allows the adjustment of the distribution function's shape so that quasi-neutrality in the box is achieved.

4.3.3 Minimization of total charge

As suggested in section 4.2.1, a Schamel phase-space hole is defined by three parameters ϕ_0, β_h, and $\delta v_{s,h}$. In general, ϕ_0 and $\delta v_{s,h}$ describe the velocity-size and hole phase velocity, respectively. We chose these two parameters to be independent in this manuscript. This will allow us to customize and study a large variety of different phase-space holes. The third parameter, β_h, is the main parameter adjusting the depth and length of the hole. Nevertheless, if we want a quasi-neutral plasma, the parameter β_h becomes a non-linear function $\beta_h(\delta v_{s,h}, \phi_0)$.

In order to find the value β_h takes for each set $(\delta v_{s,h}, \phi_0)$, we wrote a minimization algorithm that searches to optimize the Schamel *sech4* phase-space hole parameter for quasi-neutrality in the simulation box. In other words,

$$0 = \frac{e}{\varepsilon_0}\int_0^{L_x}\int_{-\infty}^{+\infty} f_{i,0}(v)dvdx - \frac{e}{\varepsilon_0}\int_0^{L_x}\int_{-\infty}^{+\infty} f_{e,h}(x,v)dvdx\ . \tag{4.9}$$

Equation 4.9 expresses the quasi-neutrality condition of the plasma in a box of length L_x. Since all the plasma parameters, namely $n_{s,0}$, $v_{s,T}$, and m_s, and hole parameters are fixed, the only way to achieve quasi-neutrality is by varying the β_h such that the regions of negative charge density are compensated by positive regions; this is shown in figure 4.6 where the electron charge density shows three extrema, two negative and one positive.

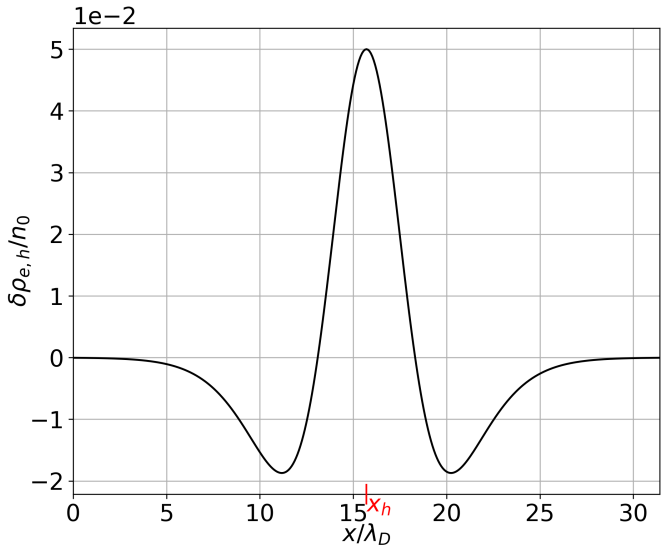

Figure 4.6: Electron charge density perturbation of a plasma with a phase-space electron-hole, for a mass ratio of $m_i/m_e = 36$, and parameters $\phi_0 = 0.05$, $\beta_h = -6.56$, and $\delta v_{e,h} = 0.45 v_T$.

4.3.4 Application: Stationary hole in COBBLES

In summary, an electron-hole with phase velocity such that $0 < v_h < v_d$ will experience an acceleration due to a repulsive force due to the ions and electron distributions gradients $\partial_v f_{e,h}|_{v_h} \partial_v f_{i,h}|_{v_h}$. The electron-hole will then climb the electron distribution and grow in size and depth. This force and hole acceleration are investigated in 5.

To verify the stability of the Schamel electron-hole in the **COBBLES** code, we performed a simulation with one initial electron-hole, with parameters $\phi_0 = 0.05$, $\beta_h = -7.29$, and $\delta v_{e,h} = 0$. In this case, $v_{h,0} = v_{e,0}$, the hole will not receive any repulsive force that will lead to an electron-hole's acceleration or deceleration. For the Schamel electron-hole distribution to be considered a stable equilibrium distribution function in our code, this electron-hole must experience a negligible acceleration during the simulation time and remain quasi-stationary.

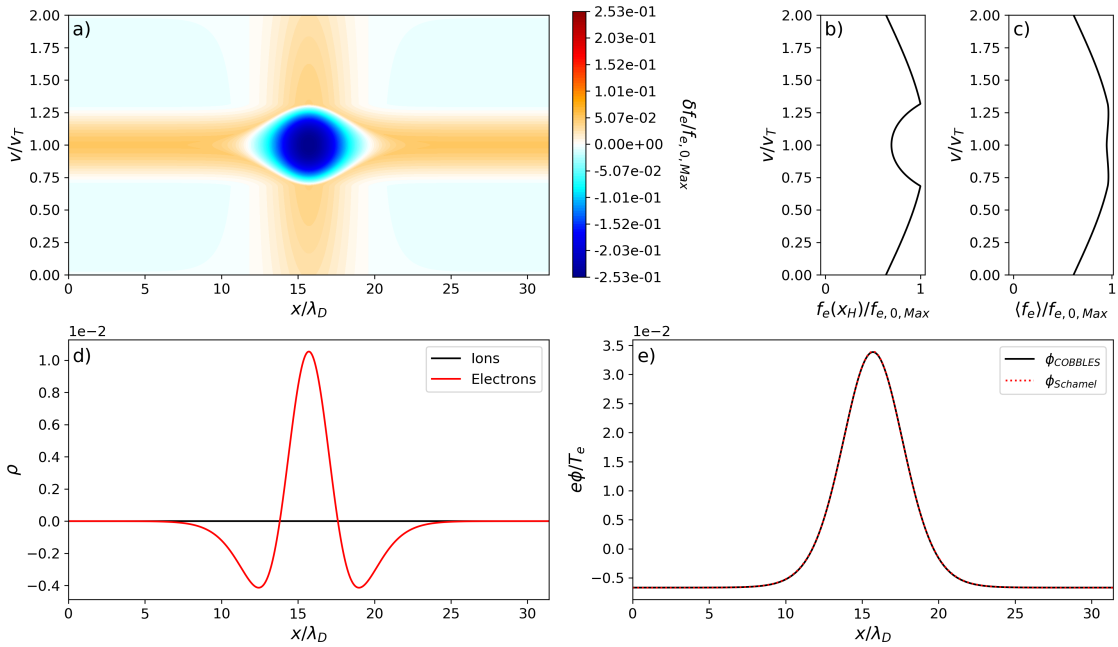

Figure 4.7: Electron-hole at $t = 0$, for a mass ratio of $m_i/m_e = 36$, and parameters $\phi_0 = 0.05$, $\beta_h = -7.29$, and $\delta v_{e,h} = 0$. *a)* the 2D distribution function, *b)* slice of f_e at $x = x_h$, *c)* spatially averaged distribution $\langle f_e \rangle$, *d)* charge density perturbation, *e)* the electric potential and a sech^4 fit. Here, the distribution functions are normalized to the maximum of the electron equilibrium distribution function $f_{e,0,max} = n_{s,0}/v_{e,T}\sqrt{2\pi}$.

Figure 4.7 and figure 4.8 show the electron distribution function, slices of the distribution function, the spatially-averaged electron distribution, the charge density perturbation and the electric potential (and a *sech4* fit) for the initial time and final time of the simulation, $t = 1500\omega_P^{-1}$. At $t = 0$, we verify that the electric potential, charge density perturbation, and distribution function are that of a Schamel electron-hole. On the other hand, for $t = 1500\omega_P^{-1}$ we observe that the distribution function and the slices at $x = x_h$ did not change in shape nor amplitude. We observe that the electric potential increased slightly in amplitude; it went from around $4 \times 10^{-2} T_e/e$ to $5 \times 10^{-2} T_e/e$. Nevertheless, the shape of the electric potential remained mostly unmodified. And lastly, we observe that the charge density perturbation of both electrons and ions changed. In the case of the ion charged density perturbation, there is a slight increase around $x = x_h$. In the case of the electron charge density perturbation, we observe a slight positive shift of the function everywhere in the box and a slight decrease in the maximum value of the perturbation around $x = x_h$, and this is to compensate for the increase of ion perturbation at the same position. In summary, the Schamel electron-hole distribution function is stable enough for a large enough

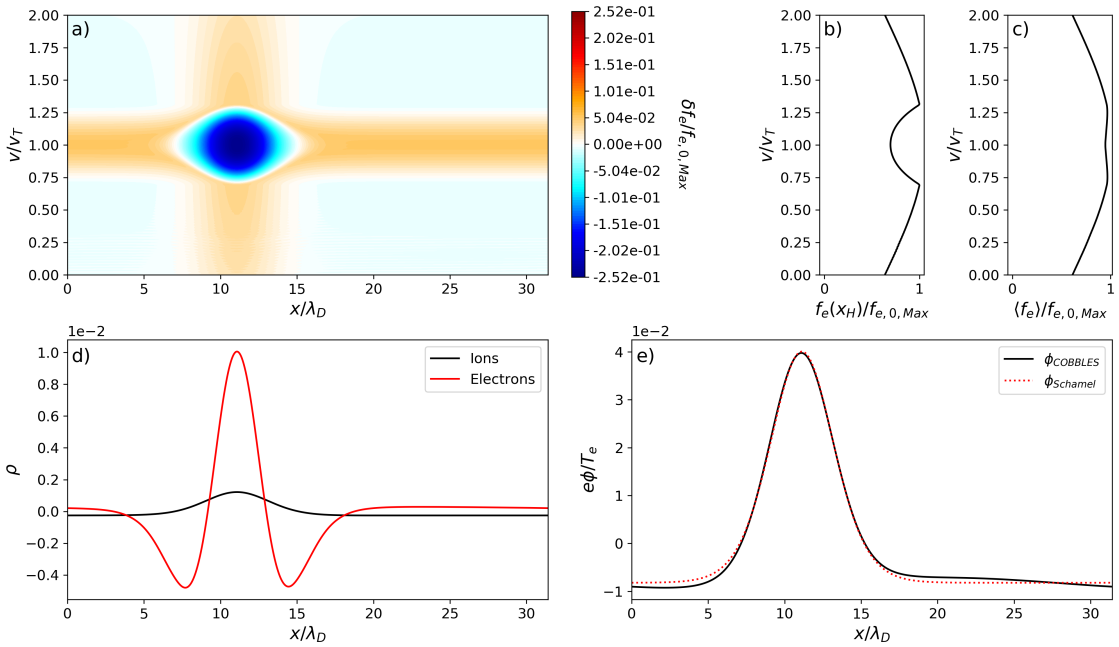

Figure 4.8: Electron-hole at $t = 1500\omega_P^{-1}$, for a mass ratio of $m_i/m_e = 36$, and parameters $\phi_0 = 0.05$, $\beta_h = -7.29$, and $\delta v_{e,h} = 0$. $a)$ the 2D distribution function, $b)$ slice of f_e at $x = x_h$, $c)$ spatially averaged distribution $\langle f_e \rangle$, $d)$ charge density perturbation, $e)$ the electric potential and a sech^4 fit. Here, the distribution functions are normalized to the maximum of the electron equilibrium distribution function $f_{e,0,max} = n_{s,0}/v_{e,T}\sqrt{2\pi}$.

simulation time, to enable our subsequent study of hole acceleration (which can be measured on timescales of the order of $10 - 100\ \omega_P^{-1}$) at fixed hole parameters.

4.4 Conclusion

In the context of the Vlasov-Poisson kinetic model governing the dynamics of a one-dimensional plasma, we presented the Schamel distribution function for solitary electron-holes, which describes the shape of an electron-hole by means of three parameters, where two of them are independent. We implemented the Schamel distribution function into the kinetic self-consistent code COBBLES and solved the implementation problems related to the charge density and periodicity by minimizing the trapping parameter β_h. And finally, we showed, via numerical simulations, that the Schamel electron-hole is a stable solution for large enough simulation times. This allows us to perform in the next chapters an in-depth study of the dynamics of electron-hole for unstable initial conditions.

Chapter 5

Dynamics of a single electron-hole

Contents

5.1 Phase-space hole dynamics

An electron-hole has rich and complex dynamics in phase-space. One of the important processes is the rapid acceleration of the hole to higher velocities and the deepening, or growth, of the electron-hole phase-space density and phasetrophy. These two quantities are studied in detail in this chapter via numerical simulations through the COBBLES Vlasov-Poisson Kinetic code.

5.1.1 State of the art

An electron-hole's stability in phase-space is a delicate balance between the electromagnetic forces of the plasma and the momentum associated with the hole. As mentioned in chapter 4, when an electron-hole's velocity takes particular values, the interaction between the trapped electrons and the ions leads to an acceleration of the electron-hole and a growth of the amplitude of the initial perturbation. In the second half of the $XXth$ century, observation in a variety of stellar [Mozer et al., 1997], laboratory [Fox et al., 2012], and numerical plasmas [Davidson et al., 1970; Ghizzo et al., 1987; Bégué et al., 1999] proved the existence of electron-holes rich dynamics, including acceleration, growth, decay, and binary interactions. In the early $80s$, a series of analytical [Boutros-Ghali and Dupree, 1982] [Dupree, 1982, 1983] [Tetreault, 1983] and numerical [Berman et al., 1982, 1985] papers proposed a theory predicting the acceleration and growth-rate of phase-space holes. However, it is not until the past few decades, through the improvement in diagnostics in spacecraft [Kamaletdinov et al., 2021], and numerical simulation [Hosseini-Jenab and Spanier, 2016; Zhou and Hutchinson, 2016; Hosseini-Jenab and Brodin, 2019; Mandal et al., 2020; Schamel et al., 2020], that more in-depth and precise studies have taken place in order to understand, explain, categorise, and predict the mechanisms of electron-hole acceleration.

5.1.2 Phase-space hole acceleration and phasetrophy growth-rate

The theories presented in the series of papers in the early $80s$ describe how small-scale phase-space granulation of the distribution function, known as clumps, grows and evolves in phase-space over time. These clumps, are a group of particles or phase-space density, all moving at roughly the same speed. One special type of these clumps is the phase-space electron-holes.

In order to describe the dynamics of a single hole, they considered the general situation where an electron hole is located at a velocity in between the maxima of the ion and electron (shifted by a given drift velocity) Gaussian distribution function, in other words, with positive hole velocity $0 < v_h < v_d$. This situation is shown in figure 5.1, where a narrow-square electron-hole initialized at a low velocity accelerates

and grows in depth to a higher velocity in a period of $t = \delta t$, climbing the electron distribution function in the process.

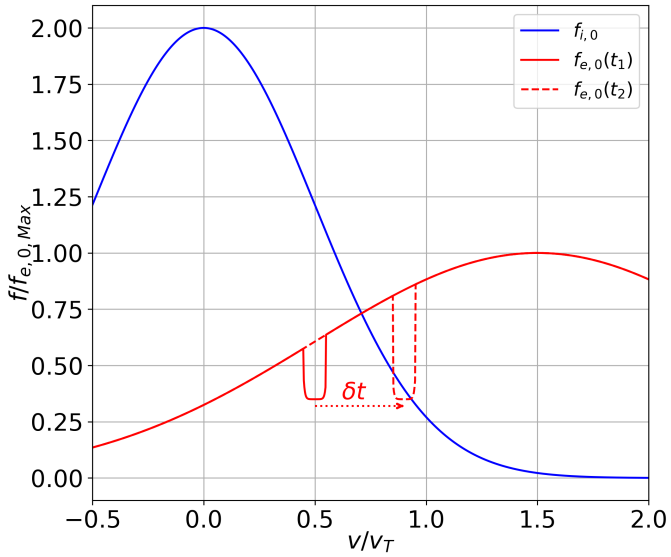

Figure 5.1: Schematic of an electron-hole acceleration and growth mechanism after a time δt between the two distributions. Ion equilibrium distribution function in blue, initial electron distribution in solid red, and final electron distribution in dashed red, normalized to the maximum of the electron equilibrium distribution function $f_{e,0,max} = n_{s,0}/v_{e,T}\sqrt{2\pi}$. The mass ratio $m_i/m_e = 4$, and the drift velocity $v_d = 1.5v_T$ are reduced for the sake of readability of the figure.

Since an electron-hole is a region of plasma with a deficit of electrons, in other words, positively charged, thus one can consider an electron-hole as a macroparticle with negative mass and positive charge. In this region of space, ions will, as a consequence, be reflected by the electric field generated by the electron-hole. If there are more ions moving at velocities slower than the electron-hole, rather than slower, then reflecting resonant ions will give energy and momentum to the hole. That is, accelerating the electron-hole, which moves it to a region of phase-space with a larger distribution function value, and since the latter must remain constant along particle trajectories to satisfy Louiville's theorem, the hole grows deeper. Physically this means that if an electron hole is located at a velocity in-between the maxima of the ion and electron distribution functions, it will tend to accelerate to a higher velocity and grow in depth and size, as shown in figure 5.1.

Clumps, including electron-hole, tend to be destroyed by particle collisions and electromagnetic turbulence in the plasma during their lifetime. However, when these collisional and electromagnetic effects occur in time scales much larger than the life-

time of an electron-hole (Which is relevant for our studies and fusion plasmas), a clump can grow before decaying. It is this rate of growth that the previously mentioned papers and this manuscript investigate.

There exist multiple ways of measuring the growth-rate of a phase-space hole. Two proportional ways to measure the same quantity are the acceleration of the clump in phase-space and the rate of growth of a global quantity known as phasetrophy. The phasetrophy ψ_h, was first introduced by P. H. Diamond as an analogy of the 2D ideal fluid enstrophy for a 1D-1V phase-space plasma [Diamond et al., 2010, 2011]. Indeed, phase-space structures resemble vortices in 2D fluid turbulence [Mcwilliams, 1984] in more than just the shape. Both systems are constrained by two invariants: the energy and enstrophy (mean square vorticity) for fluids and wave energy and the distribution perturbation square for the Vlasov plasma. Hence, the term phasetrophy stands for phase-space enstrophy.

For a 1D-1V plasma phasetrophy is defined as

$$\psi_h = \int \langle \delta f_e^2 \rangle dv \ , \tag{5.1}$$

where $\langle \delta f^2 \rangle$ is the spatial average of the distribution perturbation square. And the phasetrophy growth-rate defined as

$$\gamma_h = \frac{1}{\psi_h} \frac{d\psi_h}{dt} \ . \tag{5.2}$$

By using the conservation of $\int f^2 dv$,

$$\frac{d}{dt} \int \langle f^2 \rangle dv = \frac{d}{dt} \int \langle f \rangle^2 dv + \frac{d\psi_h}{dt} \ , \tag{5.3}$$

equation 5.2 can be simplified into

$$\gamma_h = -\frac{2}{\psi_h} \int \langle f_e \rangle \frac{\partial \langle f_e \rangle}{\partial t} dv \ , \tag{5.4}$$

which links the phasetrophy with the relaxation of f. After substituting the derivative term with the conservation of the phase-space density equation

$$\frac{\partial \langle f_e \rangle}{\partial t} + \frac{q_e}{m_e} E \frac{\partial \langle \delta f_e \rangle}{\partial v} = 0 \ , \tag{5.5}$$

and performing integration by parts, it yields an exact expression for the phasetrophy production

$$\gamma_h = -\frac{2}{\psi_h} \frac{q_e}{m_e} \int \frac{d\langle f_e \rangle}{dv} \langle E \delta f_e \rangle dv \ . \tag{5.6}$$

Assuming that the gradient of f_e remains relatively constant in the velocity interval bounded by the electron-hole velocity width Δv_h, the $\frac{d\langle f_e \rangle}{dv}$ term can be considered as constant and be taken out of the integral. What is left in the integral is a term proportional to the electric field and the distribution perturbation

$$\gamma_h = -\frac{2}{\psi_h}\frac{d\langle f_e \rangle}{dv}\frac{q_e}{m_e}\int \langle E\delta f_e \rangle dv \ . \tag{5.7}$$

Note that the integral term in equation 5.7 is defined as the electron-hole acceleration,

$$a_h \equiv \frac{q_e}{m_e}\int \langle E\delta f_e \rangle dv \ . \tag{5.8}$$

In other words, we get that the phasetrophy growth-rate and the electron-hole's acceleration are proportional to each other $\gamma_h \propto a_h$.

For consistency, this manuscript quantifies a phase-space hole's growth-rate through its phasetrophy, but via the hole's acceleration is equally valid.

Multiple theories predicting a hole's growth-rate emerged from the series of papers published in the $80s$. One of them takes a series of assumptions on the hole's shape, size, and depth [Berman et al., 1985] to deduce a simple equation for the phase-space hole growth-rate. By considering a rectangular hole, in other words, a phase-space density with a rectangular base of size $\Delta x_h \times \Delta v_h$, constant depth δf_h, and mean velocity v_h, then the growth-rate of the phase-space hole is given by

$$\frac{a_h}{\omega_P} = -2\frac{\Delta v_h}{\Delta x_h}\frac{v_T^2 \partial_v f_{e,0}|_{v_h} \partial_v f_{i,0}|_{v_h}}{(\lambda_D/\lambda)^2 + 4\left[\partial_v f_{i,0}|_{v_h}\right]^2} \tag{5.9}$$

where λ is the shielding length. The negative sign in equation 5.9 is consistent with the fact that a_h is positive for an electron-hole located in-between the maxima of the ion and electron distributions, then: the ion distribution gradient $\partial_v f_{i,0}|_{v_h}$ is negative, and the electron distribution gradient is $\partial_v f_{e,0}|_{v_h}$ positive.

Nevertheless, this equation remains a crude approximation of the growth-rate due to the assumption of the shape of the electron-hole. We compared against our numerical results and did not find agreement between simulations and theory. An improved growth-rate formula might be obtained by considering a Schamel electron-hole; however, it is not clear whether the calculations are tractable. Regardless, equation 5.9 gives us some indices on the important parameters the growth-rate could depend on. In the following section, we investigate the growth-rate of electron-holes as a function of the parameters v_h, $\partial_v f_{e,0}|_{v_h}$, $\partial_v f_{i,0}|_{v_h}$, and ϕ_0.

5.2 Single hole dynamics

In this section, we use the numerical code COBBLES to study the dynamics of isolated electron-holes over time. Hereafter, we study a two-species plasma, ions, and electrons

with a mass ratio $m_e/m_e = 36$; such a small mass ratio reduces the time necessary to perform numerical simulations and improves the numerical handling of the phase-space while retaining a significant separation of scales between electrons and ions. The system size is $L_x = 10\pi\lambda_D$. The initial velocity distribution of each species is a Gaussian. Ion mean velocity is $v_{i,0} = 0$. The ion and electron temperatures are chosen to be equal to each other $T_e = T_i$. Note that our normalization is such that our results are valid for any reasonable temperature (as long as collision and relativistic effects are negligible). The spatial resolution is chosen to be $N_x = 4096$. On the other hand, the variable parameters are the velocity-space resolution N_v, electron drift velocity $v_{e,0} = v_d$, relative electron-hole velocity δv_h, and the Schamel potential amplitude ϕ_0,

5.2.1 Time evolution of a single electron-hole

To study electron-hole's acceleration and growth, we consider electron-holes in the growth regimes, which corresponds to hole velocities in the regime $0 < v_h < v_d$. In terms of the Schamel hole parameter, the growth regime corresponds to positive relative hole velocity $\delta v_h > 0$, in other words a hole located in between the maxima of the ions and electrons distribution functions. Note that for small values of δv_h, the value of the growth-rate is such that any measurement will require significantly large simulations, which increases time-related numerical error.

To observe this acceleration, we performed a simulation with a single initial electron-hole, with parameters $v_d = 1v_T$, $\phi_0 = 0.05$, $\beta_h = -6.56$, and $\delta v_{e,h} = 0.45v_T$.

Figure 5.2 and figure 5.3 show the electron distribution function (more precisely the fluctuation $\delta f_e = f_e - \langle f_e \rangle$, slices of the distribution function, the spatially-averaged electron distribution (noted $\langle f_e \rangle$), the charge density perturbation and the electric potential (and a *sech4* fit) for the initial time and final time of the simulation, $t = 620\omega_P^{-1}$. At $t = 0$, we verify that the electric potential, charge density perturbation, and distribution function are exactly that of a Schamel electron-hole, as prescribed. After a simulated time of $620\omega_P^{-1}$, we observe that the hole quantities evolved and changed. In particular:

- The hole's velocity v_h and hole's depth $\delta f_e(x_h, v_h)$ increased during the simulation as a result of the hole's acceleration.

- We observe an increase of the electric potential amplitude from 4.15×10^{-2} to 6.71×10^{-2}. Which results in an increase of the hole's velocity width Δv_h. Moreover, we observe a slight deviation from the *sech4* potential prescribed by Schamel far away from the hole but remaining of the form *sech4* as a whole.

- The hole's width Δx_h increased during the simulation. In particular, Δx_h increases during the first stages of acceleration, which happen between $t = 0$ and

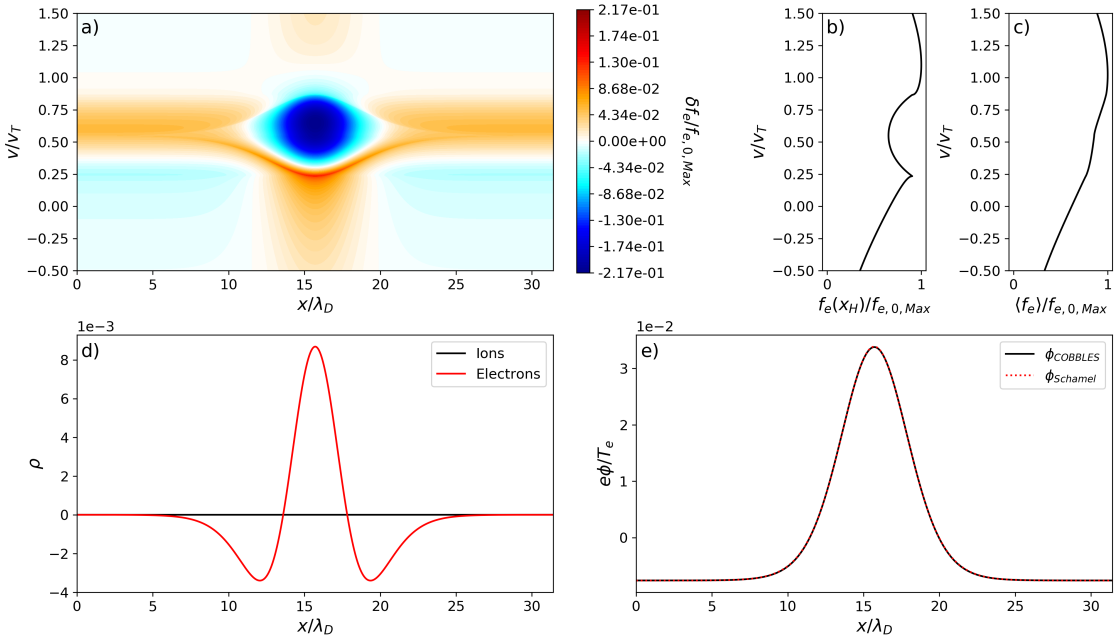

Figure 5.2: Electron-hole at $t = 0$, for a mass ratio of $m_i/m_e = 36$, and parameters $\phi_0 = 0.05$, $\beta_h = -6.56$, and $\delta v_{e,h} = 0.45 v_T$. $a)$ the 2D distribution function, $b)$ slice of f_e at $x = x_h$, $c)$ spatially averaged distribution $\langle f_e \rangle$, $d)$ charge density perturbation, $e)$ the electric potential and a sech^4 fit which is indistinguishable. Here, the distribution functions are normalized to the maximum of the electron equilibrium distribution function $f_{e,0,max} = n_{s,0}/v_{e,T}\sqrt{2\pi}$.

$t = 100\omega_P^{-1}$, then it remains constant. This is due to the hole changing its shape in order to attain a self-consistent and stable shape.

- We observe narrow horizontal bands of negative density in phase-space, reminiscent of filamentation. These bands can be thought of as the wake the hole leaves as it moves and accelerates in phase-space. Indeed, as the hole starts moving, fluctuations at low velocities of the initial hole are left behind by the hole. These bands then accelerate (since they can be considered phase-space structures on their own) and accumulate vertically at each passage of the hole. Note that the number of bands shown in phase-space is equal to the number of times the hole has moved by a distance of L_x.

- And finally, we observe differences between the initial and final electron and ion charge density. In particular, there is a large increase in the ion charge density at the hole center, and secondly, an increase in the absolute value of both charged densities far away from the hole center.

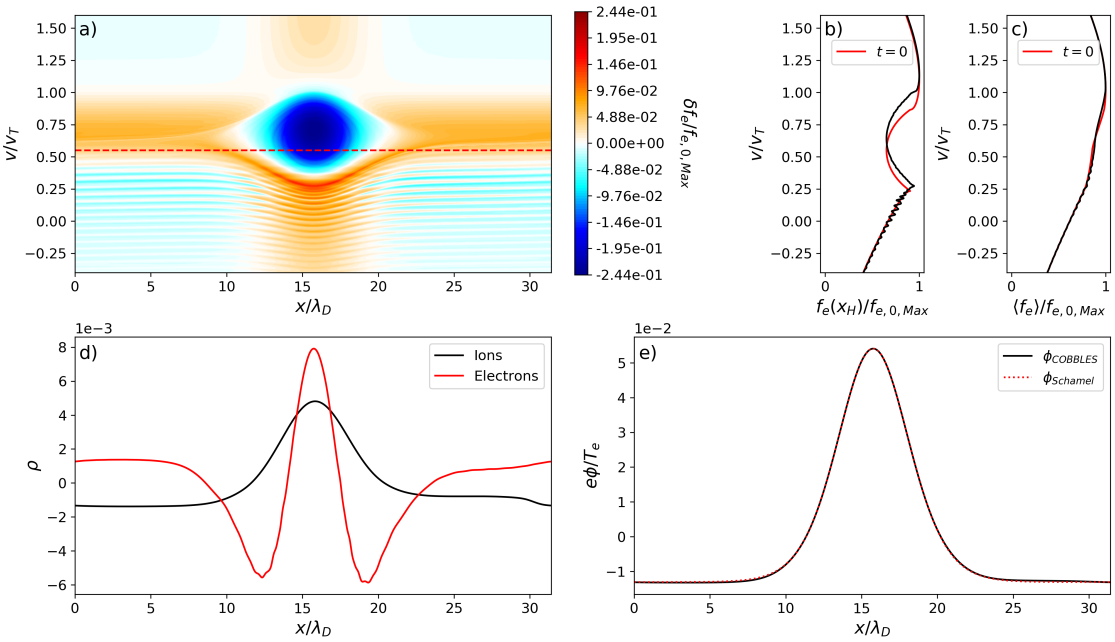

Figure 5.3: Electron-hole at $t = 620\omega_P^{-1}$, for a mass ratio of $m_i/m_e = 36$, and parameters $\phi_0 = 0.05$, $\beta_h = -6.56$, and $\delta v_{e,h} = 0.45 v_T$. $a)$ the 2D distribution function and a horizontal line at the initial velocity of the hole, $b)$ slice of f_e at $x = x_h$, $c)$ spatially averaged distribution $\langle f_e \rangle$, $d)$ charge density perturbation, $e)$ the electric potential and a sech^4 fit which is almost indistinguishable. Here, the distribution functions are normalized to the maximum of the electron equilibrium distribution function $f_{e,0,max} = n_{s,0}/v_{e,T}\sqrt{2\pi}$.

In summary, as the hole accelerates and evolves in phase-space, its physical characteristics change in order to attain a more self-consistent shape. This is shown in the increase of the hole's velocity, depth, and spatial and velocity width. Moreover, spatially large fluctuations of the electron distribution, or bands, develop at velocities inferior to that of the hole and accumulate vertically during the hole's acceleration. Finally, we observe a significant increase in the local ion charge density perturbation around the position of the electron-hole, which induces a corresponding change in the shape of both the ion and electron distributions far from the hole's position. In conclusion, a Schamel electron-hole at a velocity in between the maxima of the ions and electrons distributions is not a stable self-consistent structure. Initially, it will seek equilibrium by accelerating, changing its shape, and modifying the charge density and electric potential until a stable equilibrium is obtained after a time of several orders of magnitude.

As explained in the previous section 5.1, a solitary hole in a non-equilibrium con-

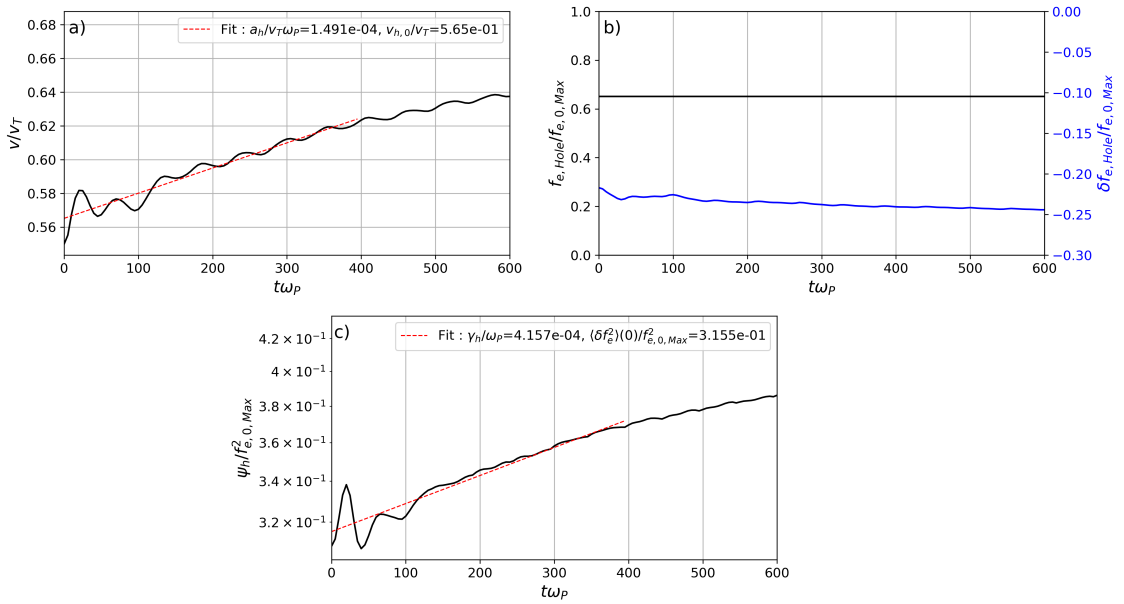

Figure 5.4: Time evolution of the electron-hole velocity in $a)$, f_e and δf_e hole depth in $b)$, and the hole phasetrophy in $c)$. For initial parameters: $v_d = 1v_T$, $\phi_0 = 0.05T_e/e$, $\beta_h = -6.56$ and $\delta v_h = 0.45v_T$

dition, such as having a non-zero δv_h, results in an acceleration of the hole, and an increase of the hole phasetrophy. Moreover, the Vlasov equation states that the phase-space distribution function $f(x, v)$ along particle trajectories is a conserved quantity. Therefore, at the hole's center, the distribution's value along deeply trapped particle trajectories must remain constant through time. We can observe these three quantities in figure 5.4, which shows the time evolution of the electron-hole velocity, hole phasetrophy, and hole depth. We observe the predicted increase of both the hole velocity and phasetrophy, and we verify that the value of the distribution at the center of the hole remains constant over time. Analytically, in this case, we expect a decrease in both the hole acceleration and growth-rate amplitude as the hole's velocity increases. This is mainly due to a decrease in the ions and electrons equilibrium distribution gradient factors. Therefore, in for our measurements, we estimate these two quantities for our electron-hole in a time interval starting after the initial stabilization of the hole at around $100\omega_P^{-1}$ and finishing at the noticeable decrease in the velocity slope at around $400\omega_P^{-1}$. We obtain that our electron-hole has an acceleration of $1.06 \times 10^{-3} v_T\omega_b$ ($1.49 \times 10^{-4} v_T\omega_P$) and a growth-rate of $2.95 \times 10^{-3}\omega_b$ ($4.16 \times 10^{-4}\omega_P$), where ω_b is the bounce frequency of the deepest trajectories of the electron-hole. Note that we have oscillations in both the hole velocity and phasetrophy (more noticeable in the velocity rather than phasetrophy). These oscillations are the result of small changes

in the hole velocity since, as it accelerates, the ions push and pull on the electron-hole to find a stable equilibrium, which is only reached after very large times (due to collisions or its numerical equivalent). Nevertheless, these oscillations are averaged in the measurement interval and do not contribute to the overall acceleration or growth-rate.

In the following sections, we chose arbitrarily to focus on the study of the phasetrophy growth-rate instead of the acceleration since they both are a measurement of the effects on the dynamics of a phase-space electron-hole.

5.3 Parameter evolution of the phasetrophy growth-rate

In this section, we performed a series of electron-hole simulations through three parameter scans: δv_h, v_d, and ϕ_0. These simulations will allow us to understand the main dependencies of electron-holes acceleration and phasetrophy growth-rate. As shown in equation 5.9, the acceleration is non-linearly dependent on the hole velocity $v_h = v_d - \delta v_h$ trough the electron and ion equilibrium distribution gradients $\partial_v f_{e,0}(v_h)$ and $\partial_v f_{i,0}(v_h)$, noted in the rest of this chapter as $f'_{e,h}$ and $f'_{i,h}$, and non-linearly dependent on ϕ_0 trough the velocity width Δv_h and Δx_h.

5.3.1 Relative hole velocity δv_h

The first parameter scan we will look at is the relative hole velocity δv_h. The variation of this parameter permits the study of the hole velocity while the drift velocity remains constant, which allows the space between distributions to stay constant while modifying the equilibrium gradients felt by the electron-hole.

We performed 10 simulations with initial parameters: $v_d = 1 v_T$, and $\phi_0 = 0.05 T_e/e$. We varied the initial δv_h from $0.65 v_T$ up to $-0.30 v_T$. Five simulations are done at positive δv_h, which translates into a positive electron gradient $f'_{e,h} > 0$, and five other simulations at nil or negative δv_h corresponding to $f'_{e,h} < 0$, and in all cases negative ion gradient $f'_{i,h} < 0$. The phasetrophy growth-rate for this parameter scan is plotted in figure 5.5 as a function of the average relative electron-hole velocity at the measurement. Note that we chose the average relative electron-hole velocity at the moment of the measurement instead of the initial relative electron-hole velocity since holes with relatively low initial velocity (close to the maxima of the ion distribution function) will experience a strong initial acceleration resulting from a reorganization of the phase-space due to interactions with the ion distribution. However, we are not interested in this initial acceleration in this study. Therefore for this and the following studies, we chose the velocity in the middle point of the interval where the growth-rate and acceleration are measured.

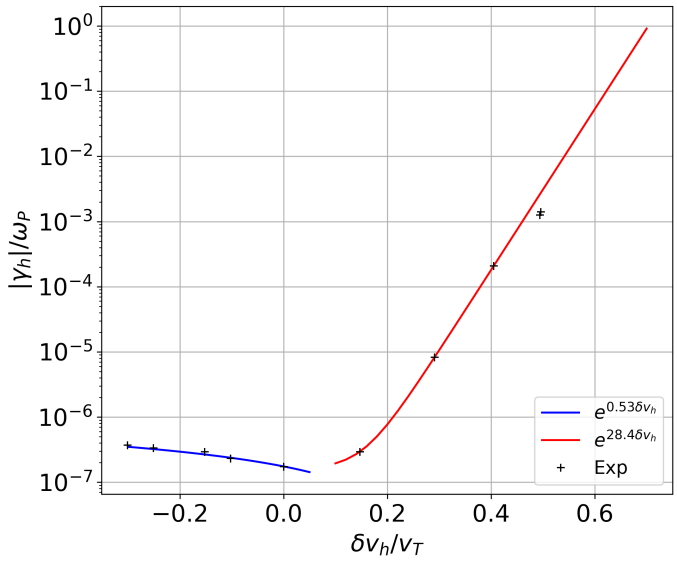

Figure 5.5: Absolute value of the electron-hole phasetrophy growth-rate as a function of the average relative electron-hole velocity at the moment of the measurement, where the y axis is in logarithmic scale. In black crosses is the growth-rate from numerical simulations, and in solid blue and red lines are exponential fits of the data in the two δv_h regimes.

Firstly, for positive δv_h, we observe an exponential increase in the growth-rate with the relative hole velocity. In particular, at low δv_h, between 0 and $0.45 v_T$, we observe a small deviation with respect to the exponential fitting with a coefficient of $28.4/v_T$, while for larger values of δv_h, a discrepancy is observed, which we assume is the result of an increase of the interactions between the electron-hole and the ion distribution. Indeed, the velocity width of this set of electron-holes is equal to $\Delta v_h = 0.64 v_T$ (or $0.32 v_T$ from the center to the edge), which is around two ion thermal velocities, where $v_{T,i} = (36)^{-1/2} \sim 0.17 v_T$. In other words, as an electron-hole approaches the ion distribution, the interaction between each other becomes increasingly important, which results in a strong and rapid non-linear initial acceleration and an abhorrent measured growth-rate. Therefore, to measure a correct acceleration and growth-rate, it is preferred to simulate electron-holes with a hole velocity such that the separatrix is separated from the ion distribution by a few ion thermal velocities. For more information on the effects of the ion distribution on electron-hole dynamics, a more precise parameter scan on this ion distribution and hole velocity gap is performed in the following section, section 5.3.3.

Lastly, for nil or negative δv_h, between $-0.3 v_T$ and 0, we observe in figure 5.5 an increase of the absolute value of the growth-rate with the decrease of δv_h. Note that

the sign of the growth-rate in this region is negative, but since it is difficult to show negative values on a logarithmic scale, we chose to show the absolute growth-rate instead. In the negative δv_h regime, for all values, including the case where $\delta v_h = 0$, we observe exponential growth with a fitting coefficient of $0.53/v_T$. Two things occur in this interval: First, the hole experiences negative gradients for both $f'_{i,h}$ and $f'_{e,h}$. Secondly, while $f'_{i,h}$ remains relatively constant, $f'_{e,h}$ increases in amplitude with the decrease in δv_h. In other words, an electron-hole with $\delta v_h/v_T = [-0.30, 0.00]$ experiences a slow decrease in its phasetrophy, contrary to the rapid increase a hole with positive δv_h experiences.

5.3.2 Local electron distribution gradient $\partial_v f_{e,0}$

In this section, we studied the effects a change in the electron gradient $f'_{e,h}$ has on the phasetrophy growth-rate. To do this, we fixed both the amplitude of the Schamel potential ϕ_0 and the electron-hole velocity v_h, while varying the relative hole velocity δv_h. We performed six simulations at a constant hole velocity of $v_h = 0.55 v_T$, and potential amplitude $\phi_0 = 0.05$. And varied the the relative hole velocity $\delta v_h/v_T = [0.00, 0.60]$, the electron mean velocity v_d is modified accordingly to equation $v_d = \delta v_h - v_h$, taking the values $v_d/v_T = [0.55, 1.15]$.

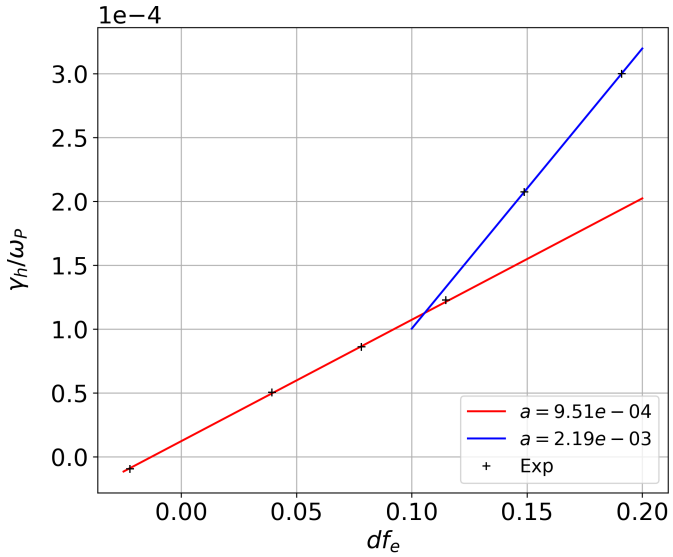

Figure 5.6: Phasetrophy growth-rate as a function of the electron equilibrium distribution gradient at the average hole velocity at the moment of the measurement. In black crosses is the growth-rate of from numerical simulations, and in solid red and blue lines are two linear fittings of the data.

This parameter scan allows us to isolate the phasetrophy growth-rate dependency on $f'_{e,h}$ since $f'_{i,h}$ remains constant between all the simulations. The results of this parameter scan are shown in figure 5.6, where the phasetrophy growth-rate is plotted as a function of $f'_{e,h}$, at the average hole velocity at the measurement.

We observe a linear relationship between $f'_{e,h}$ and the value of the phasetrophy growth-rate for values smaller than $f'_{e,h} < 12.5\%$, corresponding to values of $\delta v_h < 0.40 v_T$. This result seems to be in agreement with the dependence shown in equation 5.9 that predicts the hole acceleration to be linear with $f'_{e,h}$. On the other hand, for values of the gradient larger than 12.5%, the measurements of the growth-rate deviate from the low gradient linear fit. We observe what could be a second linear slope. Unfortunately, we do not possess enough simulation points to verify if this is indeed a linear dependence or a non-linear effect due to the large $f'_{e,h}$. Note that all the theories of single hole dynamics, presented in section 5.1.2 assume a relatively small hole located in a region of phase-space where the variations of both $f'_{i,h}$ and $f'_{e,h}$ are small. Thus, one possibility is that since the hole velocity-width extends to velocities where these variations are no longer negligible, which in practice results in a force gradient that tends to accelerate the structure unevenly. Altogether, this force gradient increases the acceleration the whole structure feels, resulting in a larger growth-rate than expected from the extrapolation at lower $f'_{e,h}$.

5.3.3 Local ion distribution gradient $\partial_v f_{i,0}$

In this section, we studied the effects a change in the ion gradient $f'_{i,h}$ has on the phasetrophy growth-rate. To do this, we fixed both the amplitude of the Schamel potential ϕ_0 and the relative electron-hole velocity $\delta v_h = 0$, while varying the hole velocity v_h. We performed seven simulations at a constant relative hole velocity of $\delta v_h = 0$, and $\phi_0 = 0.05$, and varied the other parameter in the interval $v_h/v_T = [0.35, 1.00]$, and in this case $v_h/v_T = v_d/v_T$.

Note that analytically a hole with $\delta v_h = 0$ will experience no acceleration and growth since $f'_{e,h} = 0$. Nevertheless, choosing this value of relative velocity allows us to isolate all the effects due to $f'_{e,h}$, in particular effects related to the variations on both $f'_{i,h}$ and $f'_{e,h}$, which are considered to be small by theories, since a small velocity width hole is assumed. Thus, this parameter scan allows us to isolate the phasetrophy growth-rate dependency on $f'_{i,h}$. The results of this parameter scan are shown in figure 5.7, where the phasetrophy growth-rate is plotted as a function of $f'_{i,h}$ at the average hole velocity at the measurement.

Similar to the results for $f'_{e,h}$, we observe a linear dependence of the growth-rate with $f'_{i,h}$. Note that the figure is in logarithmic scale for the x and y axis, but the fitting is precisely linear. We observe that the growth-rate increases with the $f'_{i,h}$, which is to be expected since large values of $f'_{i,h}$ correspond to a hole located closer to the ion distribution (low hole velocity). Therefore, they experience stronger effects of $f'_{i,h}$, in

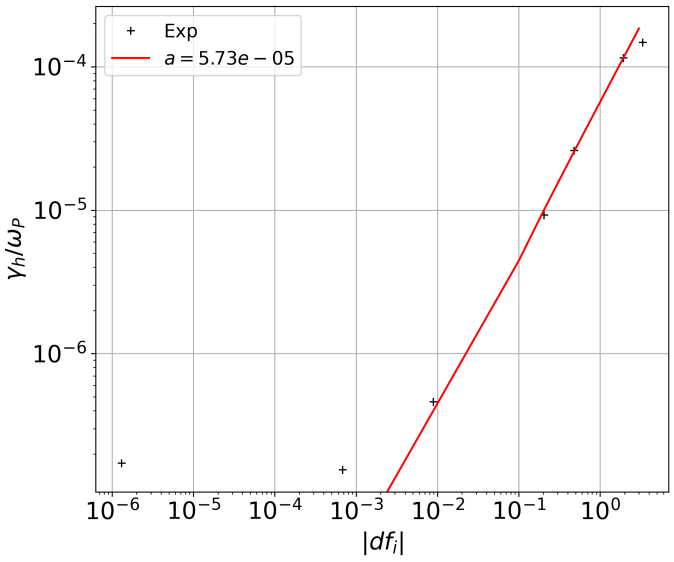

Figure 5.7: Phasetrophy growth-rate as a function of the absolute value of the ion equilibrium distribution gradient at the average hole velocity at the moment of the measurement. In black crosses is the growth-rate of from numerical simulations, and in solid red lines is a linear fitting of the data in the high amplitude regime.

particular those related to variations on $f'_{i,h}$, which is in agreement with the "aberrant" points observed in figure 5.5 and 5.6.

Moreover, for smaller values of $f'_{i,h}$, we observe that the phasetrophy growth-rate abruptly approaches zero, around 2×10^{-3}, or in terms of $v_h \sim 0.75 v_T$, which is expected, since at such velocities $f'_{i,h} \sim 0$. This value provides a limit at which the effects of ion distribution over an electron-hole's dynamics become negligible.

5.3.4 Electric potential amplitude ϕ_0

Finally, we studied the effects of the electric potential amplitude on an electron-hole phasetrophy growth-rate. To do this, we performed a parameter scan of six simulations by fixing the relative hole velocity $\delta v_h = 0.45 v_T$, and electron drift velocity $v_d = 1.00 v_T$, and varying the electric field amplitude in the interval $\phi_0 = [5 \times 10^{-3}, 1 \times 10^{-1}] T_e/e$.

As we saw in section 5.3.2 and 5.3.3, electron-hole dynamics strongly depend on the value of the ion and electron equilibrium distributions. However, changing ϕ_0 changes the width of the hole in the velocity direction. Therefore an arbitrary electron-hole will experience different gradients on the high-velocity side compared to the low-velocity, with all the intermediate gradients in between. To accommodate for the effect, we

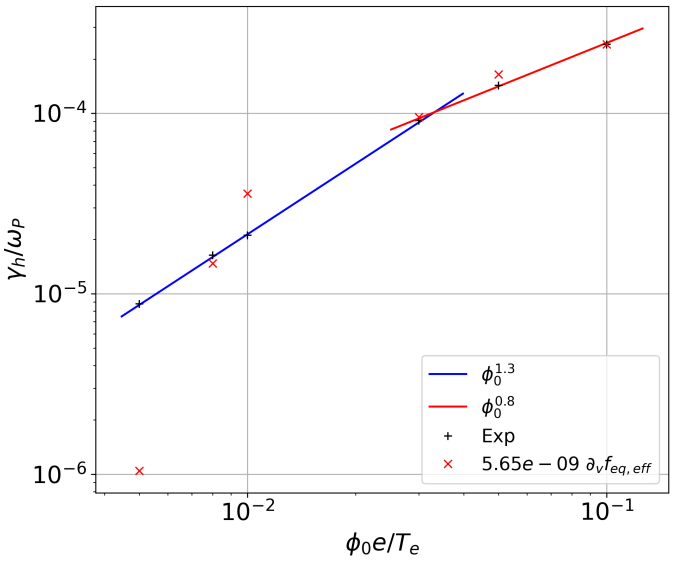

Figure 5.8: Phasetrophy growth-rate as a function of the initial Schamel electric potential amplitude. In black crosses is the growth-rate of from numerical simulations, and in solid red and blue lines are the linear fitting of the data in the low and high amplitude regime, and in red crosses is the effective electron equilibrium gradient normalized to the data.

introduce the effective electron equilibrium gradient $\partial_v f_{eq,\,eff}$ defined as the value of $f'_{e,h}$ weighted by the width of the electron-hole, in other words $\partial_v f_{eq,\,eff} \sim \partial_v f_{e,0}\sqrt{\phi_0}$.

The results of this parameter scan are shown in figure 5.8, where the phasetrophy growth-rate is plotted against ϕ_0. Firstly, we observe two regimes where the growth-rate is a power law of the potential amplitude: For $\phi_0 < 3 \times 10^{-2} T_e/e$, we measure $\gamma_h \sim \phi_0^{1.3}$, while for larger amplitudes, it increases as $\gamma_h \sim \phi_0^{0.8}$. Note that the point exactly at $\phi_0 = 3 \times 10^{-2} T_e/e$ correctly fits both power laws.

Secondly, in figure 5.8, we show $\partial_v f_{eq,\,eff}$ normalized to the data. For large values of ϕ_0, we observe qualitative and quantitative agreement between the effective gradient and the growth-rate from numerical simulations. On the other hand, for the low-amplitude regime, a large discrepancy is observed. These results allow us to conclude that for small electron-holes, where the difference in gradient between the two extremums of the hole is small, then the value of the gradient is sufficient to describe the electron-hole dynamics. On the other hand, for large electron-holes, the different regions of the electron-hole experience distinct gradients and, as a consequence, a different acceleration and increase of the phasetrophy. Thus the width of the electron-hole must be taken into account. Note that the Schamel electron-holes limit our ability to study this mechanism since the spatial and velocity widths are linked by equation

4.8, which states that the spatial width is inversely proportional to the square root of the velocity width. Thus, by decreasing Δv_h we increase Δx_h. However, this result is not physical since we know that the ratio between phase-space structures remains narrow over a large ensemble of structures, which is the case for the electron-holes simulated in this manuscript.

5.4 Conclusion

In summary, we have presented the acceleration and phasetrophy growth processes of electron-holes in phase-space. Firstly, we measured the effects of the discretization of phase-space, which results in an effective collisional operator that accelerates and smoothes phase-space holes. We performed four parameter scans on each of the hole parameters, such as the relative electron-hole velocity, Schamel potential amplitude, and $f'_{i,h}$ and $f'_{e,h}$. We have observed similarities between numerical and analytical electron-hole dynamics in these parameter scans. In particular, some similarities are:

- Hole growth is exponentially dependent on the relative hole velocity
- Linearly dependent on the electron and ion equilibrium gradients
- And a power law of the electric potential amplitude

Nevertheless, discrepancies between numerical and analytical results were observed, such as:

- For holes at negative δv_h, positive growth is observed while negative growth is predicted by theory. Resulting from the numerical discretization of phase-space.
- A larger acceleration is observed for holes at low velocities. This is due to a stronger repulsion due to the proximity in phase-space between the hole and the ion distribution.
- Effective gradient effects, resulting from small variations in the distribution gradients, $f'_{i,h}$ and $f'_{e,h}$, for holes with a large velocity width.

In conclusion, we have shown the validity and limits of analytical theories in predicting electron-hole growth by means of numerical simulations. In particular, we observed strong influences on the dynamics of an electron-hole by the ion distribution. Moreover, we found a more accurate approximation of hole growth to take into account the strong deviations resulting from variation in distribution gradients over the width of the hole by means of an effective gradient.

Chapter 6

Prescribed phase-space hole in a turbulent electric field

Contents

In the previous chapters, we studied the dynamics of charged particles in the presence of a prescribed turbulent electric field in different Kubo number regimes 3 but in the absence of phase-space structures (assuming an ensemble of waves with random phases), and the dynamics of phase-space electron-holes through a self-consistent kinetic Vlasov-Poisson code 5. In this chapter, we study the dynamics of charged particles in a prescribed turbulent electric field, including a Schamel electron-hole. This study is an intermediary step in the study of diffusion in a self-consistent problem, aiming for a deeper understanding of the dynamics generated by phase-space structures in stellar or laboratory plasmas.

6.1 Diffusion generated by an electron phase-space hole

Before addressing the numerical simulations, let us develop an analytical formulation for the diffusion coefficient of a single, isolated, phase-space electron-hole.

In general, an electron-hole can be described by a bell-shaped electric potential $\phi(x)$. As shown in section 2.1.1, in the presence of a phase-space hole, charged particles can be separated into two different trajectories:

Trapped particles follow closed orbits in phase-space, and passing, or free, particles are free of any electrostatic potential due to their large kinetic energy.

Moreover, by definition, we separate these two types of trajectories by the separatrix, which defines the last closed orbit of passing particles. Figure 2.1 in section 2.2.2 show the two types of trajectories and the separatrix.

Particle trajectories in the presence of a single phase-space structure are non-stochastic and can be analytically determined as for the case of a sinusoidal electric potential, as shown in section 2.1.2. Therefore, a different definition of the diffusion coefficient is needed. In this section, we define the diffusion coefficient of a phase-space hole as the rate of change in the velocity variance of trapped and passing particles and show analytically how phase-space structures contribute to a system's particle transport.

6.1.1 Phase-space structure diffusion coefficient

As written in section 3.2.2, the diffusion coefficient is defined to be the linear slope of the standard deviation σ_v^2 as shown in equation 3.7. In the case of phase-space trapped particle trajectories, the velocity standard deviation is defined as,

$$\sigma_{v,h}^2(t) = \frac{1}{N}\sum_{i=1}^{N}\Big[v(t,h_i) - v(0,h_i)\Big]^2 \tag{6.1}$$

where $N \to \infty$ is the total number of trapped particle trajectories, and v is the velocity of a trapped particle. h_i is the elliptic modulus, which defines the ith trajectory orbit

and energy level, defined as,

$$h_i = \sqrt{\frac{H_i + |q\phi_0|}{2|q\phi_0|}} \,, \tag{6.2}$$

which takes values in the interval $[0, 1[$. Here H_i is the particle's total energy, q is the species' electric charge, and ϕ_0 is the amplitude of the phase-space structure's electric potential.

Since we only consider trapped particle orbits, we can replace the sum over all trajectories i with an integral over all energy levels h. Indeed, if we use the following relation:

$$\lim_{N\to\infty} \frac{1}{N} \sum_{i=1}^{N} f(h_i) = \frac{1}{L-l} \int_l^L f(h) dh \tag{6.3}$$

where $f(h)$ is an arbitrary function of the energy level h. L and l are the maximal and minimal values h can takes, in our case $L = 1$ and $l = 0$.

Therefore, we can rewrite equation 6.1 as,

$$\sigma^2_{v,h}(t) = \int_0^1 \Big[v(t,h) - v(0,h)\Big]^2 dh \,. \tag{6.4}$$

If an analytical expression of the trapped particle trajectories velocities can be obtained, and the function is integrable, then equation 6.4 can be solved analytically. Otherwise, the integral can be solved with the use of numerical schemes.

6.1.2 Approximation of the Schamel potential

As shown in chapter 2, one can solve the equations of motion for two different electric potentials: The case of the harmonic oscillator 2.1.3, and the case of a sinusoidal potential 2.1.2. However, these two potentials are qualitatively different from the Schamel electron-hole.

Firstly, the Schamel electron-hole is a single bell-shaped curve with positive convex curvature at its maximum value at the position of the hole $x = x_{h,0}$, with amplitude ϕ_0. Moreover, the Schamel hole is a strictly positive function everywhere in space that approaches zero at $|x| \to \infty$. On the other hand, the harmonic oscillator potential is a quadratic function that goes to infinity as $x \to \infty$, and the pendulum potential is a $2\pi/k$ periodic function with maximum and minimum values of $\pm\varphi_0$. Therefore, to approximate the Schamel electric potential by the harmonic oscillator or the pendulum, we define a piecewise potential, where inside an interval, it takes the values of the approximation $f_{\text{Approx}}(x)$, and outside it is defined to be equal to zero. In other words:

$$\phi(x) = \begin{cases} \phi_0 f_{\text{Approx}}(x) & \frac{-\pi}{k} \leq x - x_{h,0} \leq \frac{\pi}{k} \\ 0 & 0 < |x - x_{h,0}| \end{cases} \tag{6.5}$$

where $\frac{2\pi}{k}$ is the size in the x direction of the electric potential, and k the wavenumber of the potential.

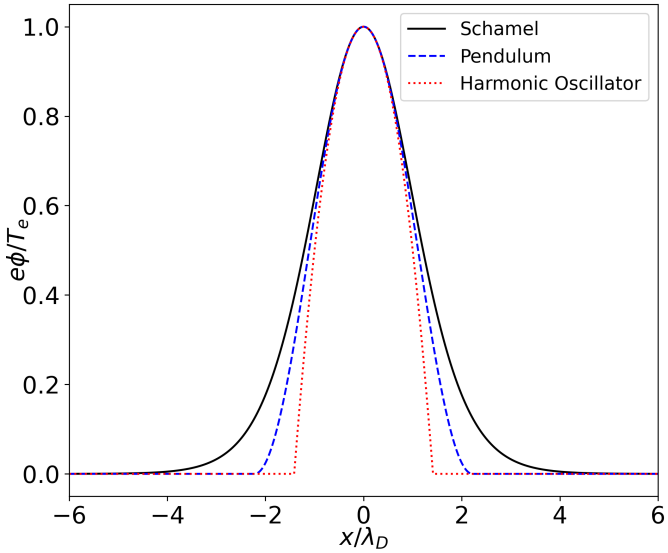

Figure 6.1: Schamel phase-space hole electric potential in black, and the pendulum and harmonic oscillator electric potential approximations in dashed blue and dotted red, respectively. With amplitude $\phi_0 = 1.T_e/e$ and $x_{h,0} = 0$.

Figure 6.1 shows the Schamel electron-hole potential, the piecewise pendulum approximation from equation 6.6, and the piecewise harmonic oscillator approximation from equation 6.11. In the two approximations, the k coefficient was chosen such that the piecewise electric potential correctly approximates the Schamel potential's most deeply trapped particle trajectories. In other words, they must resemble the Schamel potential the most around the maximum, i.e., $x = x_{h,0}$.

Pendulum electric potential

First, we approximate the Schamel electron-hole potential by the piecewise sinusoidal potential of the pendulum,

$$\phi(x) = \begin{cases} \frac{\phi_0}{2}\Big(1 + \cos k(x - x_{h,0})\Big) & -\frac{\pi}{k} \leq x - x_{h,0} \leq \frac{\pi}{k} \\ 0 & \frac{\pi}{k} < |x - x_{h,0}| \end{cases} . \tag{6.6}$$

Here the cos function is shifted upwards so that it resembles a bell-shaped function instead of being asymmetric around the horizontal axis. The wave vector k is defined as

$$k = \frac{2\sqrt{2}}{\Delta x_h} , \tag{6.7}$$

where Δx_h is the structure characteristic length defined in equation 4.8. Figure 6.1 shows this piecewise sinusoidal potential in dashed blue line.

As shown in section 2.1.2, in the case of the pendulum potential, the velocity of trapped particles follows the parametric equation 2.20. For charged trapped particles in the piecewise electric potential of equation 6.6, particle velocities are described through the equation:

$$v(y,h) = \pm\frac{2}{k}h\omega_b\sqrt{1-\mathrm{sn}^2\left[\omega_b t+\alpha_0,h\right]}+v(0,h) \tag{6.8}$$

where $\omega_b = \sqrt{|q\phi_0|k^2/m}$ is the bounce frequency, $v(0,h)$ the particle initial velocity, and α_0 the initial phase, defined by

$$\alpha_0 = K(\pi/2,h) = \int_0^{\pi/2}\frac{dz}{\sqrt{1-h^2\sin^2 z}} \tag{6.9}$$

where $K(\pi/2,h)$ is the complete elliptic integral of the first kind.

By replacing the trapped particle velocity of equation 6.8 in equation 6.4, we can rewrite the standard deviation as,

$$\sigma^2_{v,h}(t) = \frac{4}{k^2}\omega_b^2\int_0^1\left[h^2-h^2\,\mathrm{sn}^2\left[\omega_b t+\alpha_0,h\right]\right]^2 dh\,. \tag{6.10}$$

Unfortunately, as of the writing of this manuscript, equation 6.10 can not be solved analytically. Therefore, this integral needs to be integrated via numerical methods. Once the standard deviation is calculated, the maximum tangent gives the diffusion coefficient generated by one period of a shifted sinusoidal electric potential.

Harmonic oscillator approximation

Since the integral in the standard deviation of the pendulum approximation can not be solved analytically, we opt for a stronger approximation in the form of the shifted Harmonic oscillator with piecewise electric potential:

$$\phi(x) = \begin{cases} \phi_0\left(1-\frac{k^2(x-x_{h,0})^2}{4}\right) & -\frac{2}{k}\leq x-x_{h,0}\leq\frac{2}{k} \\ 0 & \frac{\pi}{k}<|x-x_{h,0}| \end{cases} \tag{6.11}$$

This eclectic potential is plotted in figure 6.1 in a dotted red line. Similarly to the pendulum approximation, the wave vector k is defined to be equal to that of equation 6.7.

Since this shifted electrostatic potential is slightly modified with respect to the Harmonic oscillator of section 2.1.3, the trapped particle's velocity now writes as,

$$v(t) = -x_0\frac{\omega_b}{\sqrt{2}}\sin\left(\frac{\omega_b}{\sqrt{2}}t\right), \tag{6.12}$$

where $\omega_b = \sqrt{|q\phi_0|k^2/m}$. Note the $\sqrt{2}$ term under all the instances of ω_b. This is due to the shifting of the potential, which results in a halving of the amplitude in front of the parabola term with respect to the classical Harmonic oscillator.

By injecting the trapped particle velocity of equation 6.12, into the standard deviation, equation 6.4, an integrating over all initial positions x_0 instead of all energy levels h, we obtain

$$\sigma^2_{v,h}(t) = \frac{k\omega_b^2}{4\pi} \sin^2\left(\frac{\omega_b}{\sqrt{2}}t\right) \int_{-\pi/k}^{\pi/k} x^2 dx \ . \tag{6.13}$$

This gives a simple expression that can be easily integrated over the $2\pi/k$ period, giving the analytic expression of the standard deviation of a shifted section of a harmonic oscillator:

$$\sigma^2_{v,h}(t) = \frac{\omega_b^2\pi^2}{6k^2} \sin^2\left(\frac{\omega_b}{\sqrt{2}}t\right) , \tag{6.14}$$

which is an oscillating function over time, with frequency $\omega_b^2/\sqrt{2}$.

Since the diffusion coefficient is defined to be half of the maximum slope of the standard deviation, the slope, or tangent, is maximum when the second derivative of the standard deviation is equal to zero. In other words, at

$$t_M = \frac{\sqrt{2}\pi}{4\omega_b} \tag{6.15}$$

Therefore, the diffusion coefficient generated by a shifted section of a harmonic oscillator is equal to

$$D_h = \frac{\omega_b^3\pi^2}{12\sqrt{2}k^2} \ . \tag{6.16}$$

which is a function of the electric potential potential, $D_h \propto \phi_0^{3/2}$.

Note that this diffusion coefficient is the diffusion generated only by trapped particles, in other words, the diffusion of particles inside a box corresponding to one period of the electric potential, with length $2\pi/k$. However, in general, the size of a phase-space hole is much smaller than the characteristic length of a plasma. Therefore, the effective diffusion coefficient needs to be multiplied by the ratio between the lengths of the phase-space hole L_{hole} and the plasma L_{Plasma}, namely,

$$D_{h,\text{eff}} = \frac{L_{\text{hole}}}{L_{\text{Plasma}}} \frac{\omega_b^3\pi^2}{12\sqrt{2}k^2} \ . \tag{6.17}$$

Moreover, if particles are assumed to be uniformly distributed on the spatial, x, direction and with initial velocities equal to that of the hole velocity, $v = v_h$ (as in the case of our simulations), this ratio is equal to the ratio between the total number of particles and the number of particles inside the phase-space structure. Note that if the initial velocity is different from the hole velocity, and between $v_h \pm \Delta v_h/2$, the length L_{hole} will be smaller and equal to the distance between the separatrix sides at the particle velocities.

6.1.3 Diffusion coefficient of a solitary hole

For the first study, we compare the analytical and numerical diffusion generated by a single Schamel phase-space hole. For this, we implemented the Schamel hole in the numerical code PERKS and initialized a set of simulations with $N = 48\,000$ particles where their initial position are uniformly distributed in the simulation box, and their initial velocity distributed in a narrow (much narrower than the hole velocity width) Gaussian velocity with mean velocity $< v_{0,i} >= 1.95 v_T$. We varied the amplitude ϕ_0 of the Schamel hole potential and measured the diffusion of particles.

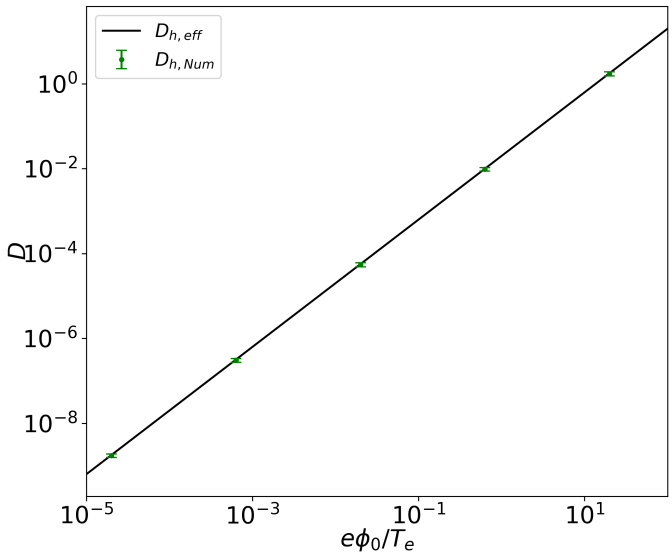

Figure 6.2: Analytical effective diffusion coefficient of a shifted Harmonic oscillator from equation 6.17, in solid black, and numerical diffusion coefficient of a Schamel potential in green dot, as a function of the electric potential amplitude ϕ_0. With wave number $k = \sqrt{2}/\lambda_D$

The results are shown in figure 6.2, where the analytical diffusion coefficient of a shifted harmonic oscillator of equation 6.16, and numerical diffusion coefficient of a Schamel potential are plotted as a function of the hole electric potential amplitude. Note that the theoretical prediction of the diffusion coefficient is overestimated by 3% with respect to the numerical diffusion coefficient, this is due to approximating the Schamel phase-space hole electrostatic potential and trajectories by the harmonic oscillator. Nonetheless, as seen in figure 6.2, despite the extreme hypothesis, there is a strong qualitative and quantitative agreement between both theory and numerical results.

In conclusion, the diffusion of a single Schamel phase-space hole from numerical

simulations can be predicted, with a reasonably good agreement, through theory by considering that particle trajectories are those of a shifted harmonic oscillator.

6.2 Diffusion in the presence of a phase-space hole

In the following section, we aim to study the effects of the diffusion of charged particles in Schamel phase-space holes with a turbulent electric field background. Since we study a Newtonian system, we can make use of the superposition principle on the electric field to include the electric field from a Schamel hole. In other words, we consider a total electric field composed of the prescribed turbulent electric field, previously studied in chapter 3 of this manuscript, and the electric field of a Schamel phase-space hole.

6.2.1 Particle trajectories of a phase-space hole in turbulence

Since the total electric field is a superposition of the turbulent electric field and the one of a Schamel hole, we expect particle trajectories to express characteristics of both dynamics. In particular, near the phase-space hole, we expect particles to experience trapped particle orbits, like those shown in figure 2.1, while far from the hole, we expect them to behave similarly to those shown in figure 3.3.

Figure 6.3 shows charged particle phase-space trajectories for a Schamel phase-space hole of amplitude $\phi_0 = 3.60 \times 10^{-3} T_e/e$, and various turbulent electric fields amplitudes with turbulent Kubo number of $K = 1.40 \times 10^{-2}$, $K = 1.98 \times 10^{-2}$, $K = 2.81 \times 10^{-2}$, and $K = 6.27 \times 10^{-2}$.

As expected, for particles inside the separatrix of the Schamel hole, trajectories are predominantly those of trapped particles, while for those outside the separatrix, trajectories resemble random-walk. Nevertheless, since there is a turbulent background, all particles experience velocity kicks that result in changes of particle's orbits. In the case of particles close to the separatrix, these velocity kicks can lead to particle trapping and detrapping, and for deeply trapped particles inside the hole's separatrix, it leads to changes in the particle's energy (orbit), which can result in the transport of deeply trapped particles to higher energy orbits or vise-versa.

Finally, as the amplitude of the turbulence increases, we observe an increase in the particle velocity variation, which is to be expected from the results of chapter 3. Moreover, as the turbulence amplitude increases, particles' trapping and detrapping near the separatrix increase as observed in figure 6.3.c. And finally, for large amplitude turbulence, figure 6.3.d, we observe that particle trajectories become dominated by turbulence, with only a few deeply trapped particles remaining inside the Schamel hole.

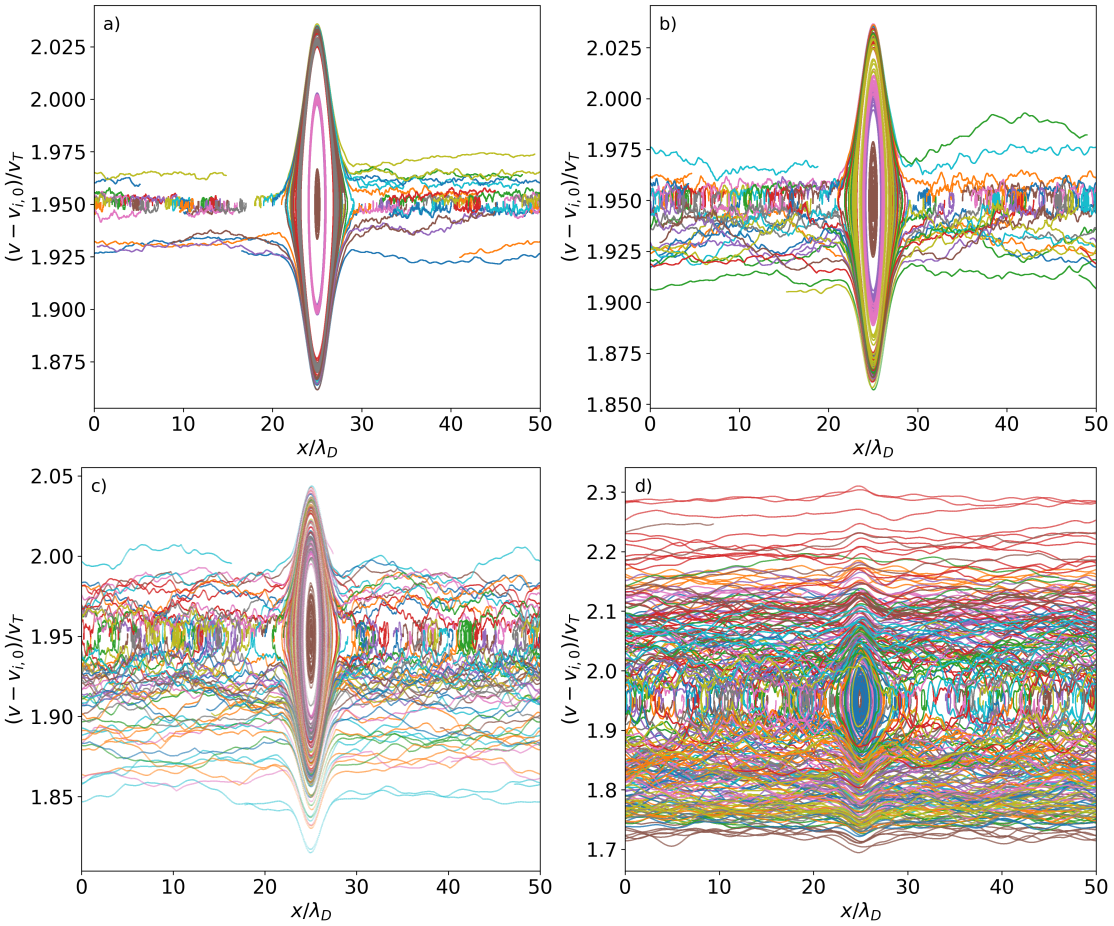

Figure 6.3: Charged particle trajectories in the presence of a background turbulent electric field and a solitary Schamel phase-space hole of amplitude $\phi_0 = 3.60 \times 10^{-3} T_e/e$. In a) for a turbulent Kubo number of $K = 1.40 \times 10^{-2}$, in b) for $K = 1.98 \times 10^{-2}$, in c) for $K = 2.81 \times 10^{-2}$, and in d) for $K = 6.27 \times 10^{-2}$.

6.2.2 Diffusion coefficient of charged particles in a superposition of electric fields

For the second study on Schamel hole diffusion coefficients, we have investigated the diffusion coefficients from numerical simulations of a superposition of electric fields. We performed a series of simulations where we vary the amplitude of turbulence while maintaining the Schamel phase-space hole amplitude ϕ_0 and size Δx_h constant.

Figure 6.4 shows the diffusion coefficient normalized to the characteristic turbulent electric field amplitude against the turbulent Kubo number, K, in the lower horizontal axis, and against the ratio between the characteristic Schamel hole and turbulent

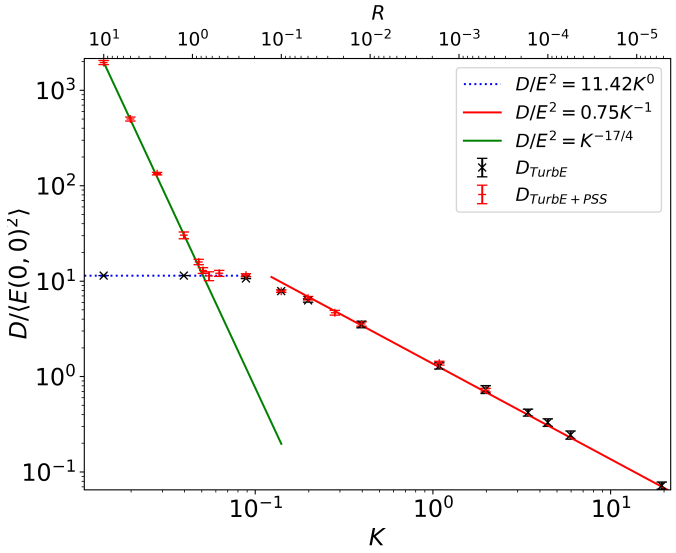

Figure 6.4: Normalized diffusion coefficient against turbulent electric field Kubo number K, and the ratio between a Schamel electron-hole's characteristic electric field amplitude and turbulence R. In black crosses, dotted blue and solid lines are the results from chapter 3 for a turbulent electric field. In red crosses is the diffusion of charged particles for a superposition of electric fields, and in solid green lines is the analytical prediction of a solitary electron-hole from equation 6.17.

electric fields, $\langle E_h^2 \rangle$ and $\langle E_{Turb}^2 \rangle$ respectively,

$$R = \frac{\langle E_h^2 \rangle}{\langle E_{Turb}^2 \rangle} \, . \tag{6.18}$$

In order to better compare the results of this series of simulations, we plotted in figure 6.4, the diffusion coefficient due to a turbulent electric field already presented in 3.11, the numerical diffusion coefficient, the quasi-linear diffusion, and the high Kubo number diffusion. In addition to those results, we have added the diffusion coefficient due to a superposition between the turbulent and hole electric fields and the analytical phase-space hole diffusion presented in section 6.1.2.

We observe that diffusion can be categorized into two distinct regimes: A first regime to the left of figure 6.4, where the dynamics of particles are dominated by the phase-space hole, and a second, to the right of figure 6.4, where the dynamics of particles are dominated by the turbulent electric field. Moreover, we observe that the transition occurs at a characteristic electric field ratio of $R \sim 0.8$. We did not measure a smooth transition between these two regimes, where both dynamics can co-exist, but a sudden transition where particle orbits change from stochastic to deterministic trajectories, or vice versa.

6.3 Conclusion

In summary, we investigated the diffusion of charged particles in a prescribed one-dimensional phase-space Schamel hole electric field by means of analytical theory and numerical simulations. First, we calculated analytically the diffusion generated by a phase-space hole by assuming that the electric potential has the shape of a shifted section of a harmonic oscillator. Secondly, we measured statistical diffusion coefficients at different phase-space hole amplitudes ϕ_0 and found qualitative and quantitative agreement between simulations and theory. Finally, we performed a study of diffusion coefficients of charged particles in a superposition of the Schamel hole and turbulent electric fields where we measured diffusion and observed two regimes of particle dynamics: A first, where the dynamics of the particles are dominated by the phase-space structure, and a second where turbulence dominates the dynamics of the plasma.

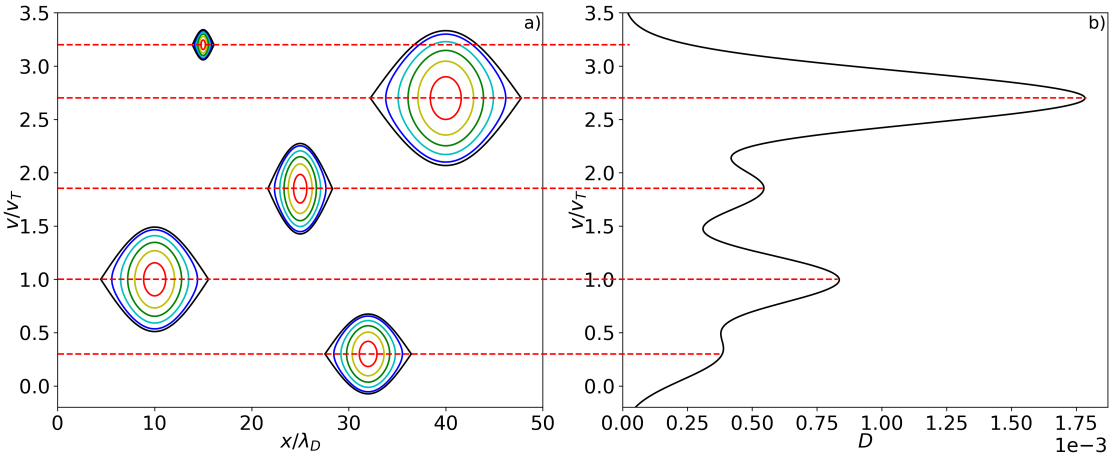

Figure 6.5: Schematic of the expected diffusion for an arbitrary number of electron-holes. In $a)$ trapped orbits in five electron-holes of arbitrary sizes. In $b)$, the schematic of the expected diffusion of a sum of electron-holes as a function of velocity.

In conclusion, we find strong qualitative and quantitative agreement between numerical simulations and the theory developed in this chapter to predict the diffusion of a single phase-space structure. In the presence of a turbulent electric field, we observe that the dynamics of the plasma are dominated by the dominant effect: If turbulence dominates over phase-space structures, then turbulent diffusion is the dominant mechanism. On the other hand, if the amplitude of phase-space structures is large enough, then the behavior of the plasma will be dictated by the dynamics of the structure.

In the case where multiple phase-space structures are present in the plasma, we expect diffusion to be a superposition of the diffusion of individual holes, as schematized

in figure 6.5 where an image of the expected diffusion in the presence of multiple holes of various sizes and velocities is shown. However, further work is required to improve the understanding of turbulence, transport, and diffusion. In particular, integrating the Poisson equation is a crucial step for achieving the complete self-consistent problem, where particle distributions are allowed to modify the electric field, and phase-space structures are inherently present [Bernstein et al., 1957; Berk et al., 1970; Schamel, 1971; Dupree, 1972; Schamel, 1972; Berk et al., 1997; Lesur et al., 2014]. Note that, although we have the tools to study the diffusion of particles in a turbulent electric field generated via self-consistent simulations, we chose to split the problem into small steps to understand the individual effects that will contribute to turbulent transport in plasmas.

Chapter 7

Conclusion

Turbulence and transport of particles and energy are fundamental processes in plasmas. Understanding turbulence and transport can help improve the understanding and control of natural or laboratory plasmas, like those of fusion devices. In one half of this manuscript, we studied one of the many mechanisms of transport, namely the diffusion of charged particles in the presence of turbulent electric fields and in the presence of phase-space structures through analytical theory, including quasi-linear and resonance broadening theories and numerical simulations. On the other hand, we studied the dynamics of phase-space structures, in particular electron-holes. We measure the growth of the structures through two methods, by means of the structure acceleration and by means of the growth-rate of the structure's phasetrophy.

We developed a test particle code to solve the trajectories of charged particles in one-dimensional turbulent electric fields. PERKS verified, qualitatively and quantitatively, the diffusion coefficients in the quasi-linear and resonance broadening regimes at different initial particle velocities for two plasma dispersion relations, namely Langmuir and ion-acoustic turbulence. Moreover, a comprehensive study of diffusion as a function of the Kubo number of turbulence showed that diffusion in turbulent electric fields occurs in three different regimes: Firstly, in the quasi-linear regime, where particles follow random-walk-like trajectories in phase-space and diffusion evolves as the square of the turbulent electric field amplitude. Secondly, diffusion evolves nonlinearly with the electric field in the resonance broadening regime, which occurs for the Kubo number of a few percent. Thirdly, for high Kubo numbers where diffusion increases as the $3/2$ power of the electric field ($E^{3/2}$), which we explain to be a random-walk diffusion of the centers of trapped particle trajectories in the velocity direction. Finally, for times much larger than τ_0 the autocorrelation time of the turbulence and τ_b the bounce time, we measure a second regime of diffusion where this one evolves as a $E^{5/4}$ for low Kubo number and $E^{3/4}$ for high Kubo number.

This manuscript delves deeper into the dynamics of phase-space structures, specifically focusing on Schamel electron-holes within phase-space. When initialized in an

unstable equilibrium of the kinetic Vlasov-Poisson model, these electron-holes undergo acceleration and eventually reach a stable equilibrium. Utilizing the kinetic code COBBLES, we studied these electron-holes acceleration and growth-rate phasetrophy based on various hole parameters. These parameters include initial velocity, electric potential amplitude, and the gradient of both ion and electron equilibrium distribution functions. Notably, our observations revealed discrepancies with theoretical predictions. Specifically, an electron-hole can exhibit growth even in conditions where no growth is theoretically anticipated. Furthermore, we noted that effective gradient effects, which arise from small variations in the equilibrium distribution gradients for holes with a large velocity width, demonstrate more favorable behavior than previously theorized. Nevertheless, as expected from theoretical predictions, we observed an exponential growth of the whole growth-rate and acceleration for different values of hole velocities. Moreover, we observe linear dependence on the equilibrium gradients and a power law on the electric potential amplitude for an initial hole far from the ion distribution. In summary, electron-hole dynamics is a more complex domain than previously thought that needs further research in both numerical simulations and analytical theory.

Finally, we studied the effects phase-space structure has on the diffusion of charged particles. We calculated the analytical diffusion generated by an electron-hole with the shape of a shifted section of a harmonic oscillator and found that diffusion is proportional to the $3/2$ power of the amplitude of the electric potential of the structure. We verified through numerical simulations that the predicted diffusion correctly matches, both qualitatively and quantitatively, the diffusion of a Schamel electron-hole. Finally, we studied the diffusion of charged particles in the presence of both a turbulent electric field and a single Schamel electron-hole. We observed two regimes of particle dynamics: A first, where the dynamics of particles are dominated by the phase-space structure. In this regime, particles near the structure follow trapped particle trajectories, while those far from it follow random-walk-like trajectories. The diffusion of particles is dominated by that generated by the structure. On the other hand, when turbulence dominates the structure, particles behave as if there is no structure in the plasma, and diffusion is given by turbulence. In the case of multiple phase-space structures, we expect diffusion to be a superposition of the diffusion of individual structures. However, further work is required to verify this assumption.

In conclusion, we showed that charge particle diffusion is a function of the amplitude of the turbulent electric field, in particular for large Kubo numbers where it increases slower than what is predicted by quasi-linear and resonance broadening theories. Moreover, we showed that in the regime of granulation where phase-space structures are present in turbulence, the structures can dominate the behavior of the plasma by generating a stronger diffusion than the turbulent background. Finally, we showed that the acceleration and growth of these phase-space structures dependent

on the different hole parameters is more complex than previously thought. By taking into account all the results from this thesis, we can expect that in the presence of large enough accelerating phase-space structures, charged particle dynamics, diffusion, and transport will be dominated by the behavior of the structure, with minimal effects coming from the turbulent background. A more in-depth study on hole dynamics needs to be performed, particularly for the case where multiple electron-holes are present in phase-space, which has been shown [Ghizzo et al., 1987; Lesur et al., 2014] to interact attractively between each other and merging into one larger structure after an asymptotically long time. In addition, the study of test particles should be continued in the presence of a self-consistent electric field like those generated from Vlasov-Poisson simulations.

Appendix A

Effective collisional operator

A.0.1 Effects of numerical collisions on hole growth-rate

As for any numerical code, the COBBLES code introduces errors originating from numerical operations performed during the calculations of new distribution functions. This numerical error can be modeled in the form of an effective collision rate $\gamma_{COBBLES}$. A paper by M. Lesur [Lesur, 2016] studies the effects of numerical errors in particle distribution, using the COBBLES code.

The effective collision rate exhibits an inverse relationship with phase-space resolution in COBBLES. In other words, as the number of grid points in the velocity direction N_v decreases, the effective collision rate increases accordingly. Practically, an effective collision operator leads to smoothing both the ion and electron distribution functions, which has the consequences of destroying small phase-space structures and flattening or smoothing large phase-space structures.

We performed two series of simulations with a single Schamel phase-space hole at varying velocity grid points N_v, one series for an electron drift velocity of $v_d = 1v_T$ and the other for $v_d = 0.25v_T$. The base parameters of the simulations are a spacial resolution $N_x = 4096$ and simulation box length $L_x = 10\pi\lambda_D$. And for the Schamel electron-hole: Relative hole-phase velocity $\delta v_h = -0.15v_T$, Schamel electric potential amplitude $\phi_0 = 0.05T_e/e$, and trapping parameter $\beta_h = -7.21$.

Figure A.1 shows the relative phase-space hole growth-rate with respect to the simulation at $N_v = 8192$,

$$\varepsilon_{\gamma_h} = \frac{|\gamma_h^{N_v} - \gamma_h^{8192}|}{\gamma_h^{8192}} \,, \tag{A.1}$$

and the same electron drift velocity as a function of the number of grid points N_v in the velocity direction. Where $\gamma_h^{8192}(vd = 1v_T) = 8.505 \times 10^{-8}\omega_P$ and $\gamma_h^{8192}(vd = 0.25v_T) = 5.095 \times 10^{-5}\omega_P$. In both series of simulations, we observe that the growth-rate increases inversely proportional to the number of grid points, implying that the phase-space hole growth-rate increases with the effective collision rate. Note that on

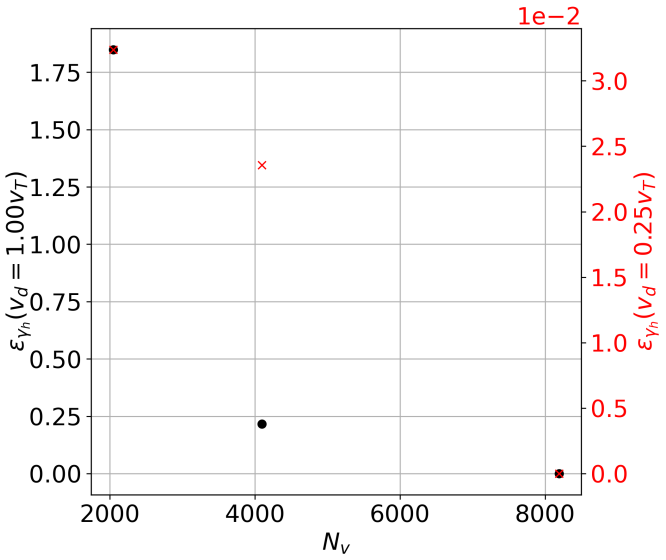

Figure A.1: Relative phase-space hole growth-rate $|\gamma_h^{N_v} - \gamma_h^{8192}|/\gamma_h^{8192}$ as a function of the number of grid points in the velocity direction N_v. Where $\gamma_h^{8192}(vd = 1v_T) = 8.505 \times 10^{-8}\omega_P$ and $\gamma_h^{8192}(vd = 0.25v_T) = 5.095 \times 10^{-5}\omega_P$. In black dots, for an initial electron drift velocity $v_d = 1v_T$, and in red crosses for $v_d = 0.25v_T$.

the simulations at $v_d = 1v_T$, we observe an increase of almost 200% for $N_v = 2048$. This increase, while big, the growth-rate of this simulation is still of the order of 10^{-7}, which in our simulations is negligible with respect to larger increases at lower hole velocities. In other words, the error originating from effective collisions, at $N_v = 2048$, is acceptable for the simulation times we chose.

Moreover, in figure A.1, we observe that this growth-rate gain increases with the electron drift velocity value. We observe that the relative growth-rate is smaller amplitude than for the simulations at $v_f = 2v_T$. This is due to the already large acceleration felt by the electron-hole due to the interactions with the ion distribution. Indeed, as shown in section 5, the gradients of particle distributions are an important parameter of a phase-space hole growth-rate. Therefore, the position of the hole with respect to the ion and electron distributions is significant. Thus, the increase in growth-rate due to the effective collision rate is non-linearly related to the velocity of a hole. For more information on the effects of distribution gradients on the phasetrophy growth-rate, an in-depth study is performed in section 5.3.2 and section 5.3.3.

In conclusion, we observed that the discretization of the phase-space results in an effective collisional operator, which increases the amplitude of the phase-space electron-hole growth-rate. Furthermore, we observed that this increase in the hole's growth-rate depends on both the number of grid points in the velocity direction and

the hole's velocity with respect to the ion and electron distribution maxima. During all the other simulations of phase-space holes via the COBBLES code, we arbitrarily chose $N_v = 4096$ since it is a compromise between numerical accuracy and simulation time.

Bibliography

Abiteboul, J., Garbet, X., Grandgirard, V., Allfrey, S. J., Ghendrih, P., Latu, G., Sarazin, Y., and Strugarek, A. (2011). Conservation equations and calculation of mean flows in gyrokinetics. *Physics of Plasmas*, 18(8).

Adam, J. C., Laval, G., and Pesme, D. (1981). Effets des interactions résonnantes ondes-particules en turbulence faible des plasmas. *Annals of Physics*, 6:319–420.

Arnold, V. I. (1963). Proof of a theorem of A. N. Kolmogorov on the invariance of quasi-periodic motions under small perturbations of the Hamiltonian. *Russian Mathematical Surveys*, 18(5):9–36.

Balescu, R. (1963). Statistical Mechanics of Charged Particles. *Interscience*.

Bégué, M. L., Ghizzo, A., and Bertrand, P. (1999). Two-Dimensional Vlasov Simulation of Raman Scattering and Plasma Beatwave Acceleration on Parallel Computers. *Journal of Computational Physics*, 151:458–478.

Benettin, G., Galgani, L., and Strelcyn, J. M. (1976). Kolmogorov entropy and numerical experiments. *Physical Review A*, 14(6):2338–2345.

Bénisti, D. and Escande, D. F. (1997). Origin of diffusion in Hamiltonian dynamics. *Physics of Plasmas*, 4(5):1576–1581.

Bénisti, D. and Escande, D. F. (1998). Finite range of large perturbations in Hamiltonian dynamics. *Journal of Statistical Physics*, 92(5-6):909–972.

Berk, H. L., Breizman, B., and Petviashvili, N. (1997). Spontaneous hole-clump pair creation in weakly unstable plasmas. *Physics Letters A*, 234(3):213–218.

Berk, H. L., Nielsen, C. E., and Roberts, K. V. (1970). Phase space hydrodynamics of equivalent nonlinear systems: Experimental and computational observations. *Physics of Fluids*, 13(4):980–995.

Berman, R. H., Tetreault, D. J., and Dupree, T. H. (1985). Simulaton of phase space hole growth and the development of intermittent plasma turbulence. *Physics of Fluids*, 28(1).

Berman, R. H., Tetreault, D. J., Dupree, T. H., and Boutros-Ghali, T. (1982). Computer Simulation of Nonlinear Ion-Electron Instability. *Physical Review Letters*, 48(18):1249–1252.

Bernstein, I. B., Greene, J. M., and Kruskal, M. D. (1957). Exact Nonlinear Plasma Oscillations. *Physical Review Letters*, 108.

Besse, N., Elskens, Y., Escande, D. F., and Bertrand, P. (2011). Validity of quasilinear theory: Refutations and new numerical confirmation. *Plasma Physics and Controlled Fusion*, 53(2).

Boltzmann, L. (1895). *Lectures on Gas Theory*. Dover Publications, first publ edition.

Boström, R., Gustafsson, G., Holback, B., Holmgren, G., Koskinen, H., and Kintner, P. (1988). Characteristics of solitary waves and weak double layers in the magnetospheric plasma. *Physical Review Letters*, 61(1):82–85.

Boutros-Ghali, T. and Dupree, T. H. (1982). Theory of nonlinear ion-electron instability. *Physics of Fluids*, 25(5):874–883.

Brandon, J., Lichtenberg, A. J., and Lieberman, M. A. (1995). *Regular and Chaotic Dynamics*, volume 79.

Bychenkov, V. Y. (2018). Ion acoustic turbulence driven by return current leads to hot electrons in laser-produced plasma. *Physics of Plasmas*, 25(10).

Cary, J. R., Escande, D. F., and Verga, A. D. (1990). Nonquasilinear diffusion far from the chaotic threshold. *Physical Review Letters*, 65(25):3132–3135.

Chirikov, B. V. (1960). Resonance processes in magnetic traps. *The Soviet Journal of Atomic Energy*, 6(6):464–470.

Chirikov, B. V. (1969). Reseach concerning the theory of non-linear resonance and stochasticity. *Nuclear Physics Institute of SIberian Academy of Sciences*.

Chirikov, B. V. (1979). A universal instability of many-dimensional oscillator systems. *Physics Reports*, 52(5):263–379.

Crews, D. W. and Shumlak, U. (2022). On the validity of quasilinear theory applied to the electron bump-on-tail instability. *Physics of Plasmas*, 29(4).

Davidson, R. C., Krall, N. A., Papadopoulos, K., and Shanny, R. (1970). Electron heating by Electron-Ion beam instability. *Physical Review Letters*, 24(11):160.

Depret, G., Garbet, X., Bertrand, P., and Ghizzo, A. (2000). Trapped-ion driven turbulence in tokamak plasmas. *Plasma Physics and Controlled Fusion*, 42(9):949–971.

Diamond, P. H., Itoh, S.-I., and Itoh, K. (2010). *Modern Plasma Physics*, volume 9780521869. Cambridge University Press.

Diamond, P. H., Kosuga, Y., and Lesur, M. (2011). Dynamics of Structures in Configuration Space and Phase Space: An Introductory Tutorial. In *Rotation and Momentum Transport in Magnetized Plasmas*, number June 2011, pages 81–113. WORLD SCIENTIFIC.

Doveil, F. and Grésillon, D. (1982). Statistics of charged particles in external random longitudinal electric fields. *Physics of Fluids*, 25(8):1396–1402.

Drummond, W. and Pines, D. (1962). Nonlinear stability of plasma oscillations. *Nuclear Fusion (Austria)*, Vol: Suppl:1049–1057.

Dupree, T. H. (1966). A Perturbation Theory for Strong Plasma Turbulence. *Physics of Fluids*, 9(9):1773.

Dupree, T. H. (1967). Nonlinear theory of drift-wave turbulence and enhanced diffusion. *Physics of Fluids*, 10(5):1049–1055.

Dupree, T. H. (1972). Theory of phase space density granulation in plasma. *Physics of Fluids*, 15(2):334–344.

Dupree, T. H. (1982). Theory of phase-space density holes. *Physics of Fluids*, 25(2):277–289.

Dupree, T. H. (1983). Growth of phase-space density holes. *Physics of Fluids*, 26(9).

Durran, D. R. (1999). Semi-Lagrangian Methods. pages 303–333.

Ergun, R. E., Carlson, C. W., McFadden, J. P., Mozer, F. S., Delory, G. T., Peria, W., Chaston, C. C., Temerin, M., Roth, I., Muschietti, L., Elphic, R., Strangeway, R., Pfaff, R., Cattell, C. A., Klumpar, D., Shelley, E., Peterson, W., Moebius, E., and Kistler, L. (1998). FAST satellite observations of large-amplitude solitary structures. *Geophysical Research Letters*, 25(12):2041–2044.

Escande, D. F. (1982). Renormalization for stochastic layers. *Physica D: Nonlinear Phenomena*, 6(1):119–125.

Escande, D. F. and Doveil, F. (1981). Renormalization method for computing the threshold of the large-scale stochastic instability in two degrees of freedom Hamiltonian systems. *Journal of Statistical Physics*, 26(2):257–284.

Escande, D. F. and Sattin, F. (2007). When can the Fokker-Planck equation describe anomalous or chaotic transport? *Physical Review Letters*, 99(18):1–4.

Falessi, M. V., Pegoraro, F., and Schep, T. J. (2015). Lagrangian coherent structures and plasma transport processes. *Journal of Plasma Physics*, 81(5):1–15.

Fox, W., Porkolab, M., Egedal, J., Katz, N., and Le, A. (2012). Observations of electron phase-space holes driven during magnetic reconnection in a laboratory plasma. *Physics of Plasmas*, 19(3).

Ghizzo, A. (1987). *Apport des codes euleriens à la simulation numérique en physique des plasmas : Application à l'étude des structures de Bernstein - Greene - Kruskal*. PhD thesis, Université Henri Poincaré, Nancy.

Ghizzo, A., Izrar, B., and Bertrand, P. (1987). BGK STRUCTURES AS QUASI-PARTICLES. *Physics Letters*, 120(4).

Gorbunov, L. M. (1973). Hydrodynamics of plasma in a strong high- frequency field. *Soviet Physics Uspekhi*, 16:19.

Grandgirard, V. (2016). *The GYSELA project: A semi-Lagrangian code addressing gyrokinetic full-f global simulations of flux driven tokamak plasmas*. PhD thesis, Université de Strasbourg.

Guillevic, A., Lesur, M., Garbet, X., Diamond, P. H., Lo-Cascio, G., Kosuga, Y., Gravier, E., Mandal, D., Ghizzo, A., and Réveillé, T. (2023). Particle dynamics in a turbulent electric field. *Physics of Plasmas*, 30(5).

Hamilton, R. J. and Petrosian, V. (1992). Stochastic acceleration of electrons. I - Effects of collisions in solar flares. *The Astrophysical Journal*, 398:350.

Hasegawa, A. (1974). Instabilities and nonlinear processes in geophysics and astrophysics. *Reviews of Geophysics*, 12(2):273.

Hirose, A. and Ishihara, O. (1999). On plasma diffusion in strong turbulence. *Canadian Journal of Physics*, 77(10):829–833.

Hosseini-Jenab, S. M. and Brodin, G. (2019). Head-on collision of nonlinear solitary solutions to Vlasov-Poisson equations. *Physics of Plasmas*, 26(2).

Hosseini-Jenab, S. M. and Spanier, F. (2016). Study of trapping effect on ion-acoustic solitary waves based on a fully kinetic simulation approach. *Physics of Plasmas*, 23(10).

Ishihara, O., Xia, H., and Hirose, A. (1992). Resonance broadening theory of plasma turbulence. *Physics of Fluids B*, 4(2):349–362.

Kamaletdinov, S. R., Hutchinson, I. H., Vasko, I. Y., Artemyev, A. V., Lotekar, A., and Mozer, F. (2021). Spacecraft Observations and Theoretical Understanding of Slow Electron Holes. *Physical Review Letters*, 127(16):165101.

Khotyaintsev, Y. V., Vaivads, A., André, M., Fujimoto, M., Retinò, A., and Owen, C. J. (2010). Observations of slow electron holes at a magnetic reconnection site. *Physical Review Letters*, 105(16):1–4.

Kindel, J. M. and Kennel, C. F. (1971). Topside current instabilities. *Journal of Geophysical Research*, 76(13):3055–3078.

Kolmogorov, A. N. (1941). The Local Structure of Turbulence in Incompressible Viscous Fluid for Very Large Reynolds Numbers. *Akademiia Nauk SSSR Doklady*, 30:301–305.

Kolmogorov, A. N. (1954). On conservation of conditionally periodic motions for a small change in Hamilton's function. *Dokl. Akad. Nauk SSSR*, (98):527–530.

Kubo, R. (1963). Stochastic Liouville Equations. *Journal of Mathematical Physics*, 4(2):174–183.

Laval, G. and Pesme, D. (1983). Breakdown of quasilinear theory for incoherent 1-D Langmuir waves. *Physics of Fluids*, 26(1):52–65.

Lenard, A. (1960). On Bogoliubov's kinetic equation for a spatially homogeneous plasma. *Annals of Physics*, 10(3):390–400.

Lesur, M. (2010). *The Berk-Breizman Model as a Paradigm for Energetic Particle-driven Alfvén Eigenmodes*. PhD thesis.

Lesur, M. (2016). Method- and scheme-independent entropy production in turbulent kinetic simulations. *Computer Physics Communications*, 200:182–189.

Lesur, M., Diamond, P. H., and Kosuga, Y. (2014). Nonlinear current-driven ion-acoustic instability driven by phase-space structures. *Plasma Physics and Controlled Fusion*, 56(7).

Lesur, M., Idomura, Y., and Tokuda, S. (2006a). Kinetic Simulations of Electrostatic Waves using Cubic-Interpolated-Propagation Scheme. *JAEA-Research*, 89.

Lesur, M., Idomura, Y., and Tokuda, S. (2006b). Kinetic Simulations of Electrostatic Waves using Cubic-Interpolated-Propagation Scheme with Errata. *JAEA-Research*, 89.

Lim, K., Gravier, E., Lesur, M., Garbet, X., Sarazin, Y., and Médina, J. (2020). Impurity pinch generated by trapped particle driven turbulence. *Plasma Physics and Controlled Fusion*, 62(9).

Liu, W., Petrosian, V., Dennis, B. R., and Jiang, Y. W. (2008). Double Coronal Hard and Soft X-Ray Source Observed by RHESSI : Evidence for Magnetic Reconnection and Particle Acceleration in Solar Flares . *The Astrophysical Journal*, 676(1):704–716.

Luque, A. and Schamel, H. (2005). Electrostatic trapping as a key to the dynamics of plasmas, fluids and other collective systems.

Mandal, D., Sharma, D., and Schamel, H. (2020). Ultra slow electron holes in collisionless plasmas: Stability at high ion temperature. *Physics of Plasmas*, 27(2).

Mcbride, J. B., Edward, O. T., Boris, J. P., and Orens, J. H. (1972). Theory and simulation of turbulent heating by the modified two-stream instability. *Physics of Fluids*, 15(12):2367–2382.

Mcwilliams, J. C. (1984). The emergence of isolated coherent vortices in turbulent flow. *Journal of Fluid Mechanics*, 146:21–43.

Médina, J., Lesur, M., Gravier, E., Réveillé, T., Idouakass, M., Drouot, T., Bertrand, P., Cartier-Michaud, T., Garbet, X., and Diamond, P. H. (2018). Radial density and heat fluxes description in the velocity space: Nonlinear simulations and quasi-linear calculations. *Physics of Plasmas*, 25(12).

Möser, J. (1962). On invariant curves of area-preserving mappings of an annulus. *Nachr. Akad. Wiss. Göttingen*, 2:1–20.

Mozer, F. S., Ergun, R., Temerin, M., Cattell, C., Dombeck, J., and Wygant, J. (1997). New features of time domain electric-field structures in the auroral acceleration region. *Physical Review Letters*, 79(7):1281–1284.

Nakamura, T., Tanaka, R., Yabe, T., and Takizawa, K. (2001). Exactly Conservative Semi-Lagrangian Scheme for Multi-dimensional Hyperbolic Equations with Directional Splitting Technique. *Journal of Computatuinal Physics*, 174.

Papadopoulos, K. (1977). A Review of Anomalous Resistivity for the Ionosphere. *Reviews of Geophysics and Space Physics*, 15(1).

Rechester, A. B., Rosenbluth, M. N., and White, R. B. (1981). Fourier-space paths applied to the calculation of diffusion for the Chirikov-Taylor model. *Physical Review A*, 23(5):2664–2672.

Roberts, K. V. and Berk, H. L. (1967). NonLinear Evolution of a two-Stream Instability. *Physical Review Letters*, 19(6):853.

Romanov, Y. and Filippov, G. F. (1961). The interaction of fast electron beams with longitudinal plasma waves. *Soviet Physics JETP*, 13(1):87–92.

Sagdeev, R. Z. (1966). *Reviews of Plasma Physics*, volume 4. New York.

Sarazin, Y., Grandgirard, V., Fleurence, E., Garbet, X., Ghendrih, P., Bertrand, P., and Depret, G. (2005). Kinetic features of interchange turbulence. *Plasma Physics and Controlled Fusion*, 47(10):1817–1839.

Schamel, H. (1971). Stationary solutions of the electrostatic Vlasov equation. *Plasma Physics*, 13(6):491–505.

Schamel, H. (1972). Non-linear electrostatic plasma waves. *Journal of Plasma Physics*, 7(1):1–12.

Schamel, H. (2000). Hole equilibria in Vlasov–Poisson systems: A challenge to wave theories of ideal plasmas. *Physics of Plasmas*, 7(12):4831–4844.

Schamel, H., Mandal, D., and Sharma, D. (2020). Evidence of a new class of cnoidal electron holes exhibiting intrinsic substructures, its impact on linear (and nonlinear) Vlasov theories and role in anomalous transport. *Physica Scripta*, 95(5).

Sonnendrücker, E., Roche, J., Bertrand, P., and Ghizzo, A. (1999). The Semi-Lagrangian Method for the Numerical Resolution of the Vlasov Equation. *Journal of Computational Physics*, 149(2):201–220.

Tetreault, D. J. (1983). Growth rate of the clump instability. *Physics of Fluids*, 26(11):3247.

Tsunoda, S. I., Doveil, F., and Malmberg, J. H. (1987a). Experimental test of the quasilinear theory of the interaction between a weak warm electron beam and a spectrum of waves. *Physical Review Letters*, 58(11):1112–1115.

Tsunoda, S. I., Doveil, F., and Malmberg, J. H. (1987b). Nonlinear Interaction between a Warm Electron Beam and a Single Wave. *Physical Review Letters*, 59(24):2752–2755.

Tsunoda, S. I., Doveil, F., and Malmberg, J. H. (1991). Experimental test of quasilinear theory. *Physics of Fluids B: Plasma Physics*, 3(10):2747–2757.

Vedenov, A. A., Velikhov, E. P., and Sagdeev, R. Z. (1962). Quasilinear theory of plasma oscillations. *Nuclear Fusion Suppl. 2: 465-475.*

Vlad, M. and Spineanu, F. (2017). Random and quasi-coherent aspects in particle motion and their effects on transport and turbulence evolution. *New Journal of Physics*, 19(2).

Vlad, M., Spineanu, F., Misguich, J. H., Reuss, J. D., Balescu, R., Itoh, K., and Itoh, S. I. (2004). Lagrangian versus Eulerian correlations and transport scaling. *Plasma Physics and Controlled Fusion*, 46(7):1051–1063.

Weinstock, J. (1968). Turbulent diffusion, particle orbits, and field fluctuations in a plasma in a magnetic field. *Physics of Fluids*, 11(9):1977–1981.

Zhou, C. and Hutchinson, I. H. (2016). Plasma electron hole kinematics. II. Hole tracking Particle-In-Cell simulation. *Physics of Plasmas*, 23(8).

Summary in french

1. Plasmas

Les concepts théoriques fondamentaux de la physique des plasmas ont été développés dans la première moitié du 20e siècle. Cependant, en raison de l'absence de technologies, la température des plasmas expérimentaux était généralement basse, de l'ordre de quelques électronvolts. Dans le régime des plasmas à "basse température", de nombreuses applications pratiques ont été envisagées et développées dans plusieurs domaines dont l'industriel, de la médecine ou de la communication. Ce n'est qu'au milieu du siècle que l'utilisation des plasmas pour la production d'énergie par des réactions de fusion nucléaire a été considère. Ce nouvel objectif a déplacé les niveaux d'énergie pertinents de plusieurs ordres de grandeur (des dizaines de kiloélectronvolts) et a accéléré le développement de la physique moderne des plasmas.

À des niveaux d'énergie aussi élevés, la plupart des particules du plasma sont ionisées, ce que l'on appelle un plasma à haute température ou hautement ionisé. Dans ce cas, le plasma peut être considéré comme un ensemble de particules chargées librement avec une très petite fraction de particules neutres. Le comportement d'un tel état de la matière devient collectif par nature, dicté par des forces électromagnétiques à longue portée : Le mouvement d'une particule typique est régi par des interactions électromagnétiques avec une collection de particules distantes au lieu d'interactions binaires entre particules voisines, contrairement au couplage fort entre particules individuelles qui régit les fluides neutres.

Outre l'importance pratique potentielle des plasmas, les recherches sur la dynamique des plasmas présentent un intérêt inhérent pour les physiciens sur de multiples fronts. À l'échelle macroscopique, le couplage entre divers mouvements et les champs électromagnétiques fluctuants donne lieu à des études considérables sur les instabilités du plasma. Au niveau microscopique, le plasma est constitué d'une collection de particules interagissant par le biais de forces à longue portée, présentant ainsi un problème à N corps d'un immense intérêt académique. Enfin, il pourrait conduire à des progrès significatifs dans la compréhension et la connexion entre la description microscopique et macroscopique d'un plasma, comme le transport des particules et de l'énergie.

Dans la littérature, différents termes peuvent être rencontrés en fonction de la na-

ture du plasma, tels que : "haute température", "faiblement couplé", "Vlasov" ou "sans collision". Dans les plasmas astrophysiques et interplanétaires, qui sont des plasmas de faible densité, la température absolue atteint des niveaux où l'énergie cinétique thermique dépasse considérablement l'énergie potentielle des interactions entre les particules chargées. En revanche, dans les plasmas à confinement magnétique, la température des ions et des électrons est de l'ordre de quelques millions de degrés. Ces plasmas sont confinés dans des champs magnétiques puissants, où la fréquence des collisions (ou le libre parcours moyen) est supérieure de plusieurs ordres à la taille de la machine.

L'un des défis de l'étude des plasmas à haute température réside dans la dynamique complexe que présentent les paramètres du plasma, tels que les densités de particules, les températures ou les champs magnétiques, à différentes échelles de temps. À court terme, des instabilités ou des fluctuations de ces quantités apparaissent. Parmi les causes, on peut citer les résonances onde-particule, les espèces à évolution rapide comme les électrons, ou les effets non linéaires. À moyen terme, le plasma connaît une croissance des instabilités linéaires et des transitions vers l'équilibre. Cela inclut le développement, la croissance et la dissipation de structures cohérentes dans l'espace des phases ou la génération de turbulences dans le plasma. Et pour les grandes échelles de temps, un état quasi-stationnaire est caractérisé par une forte saturation non linéaire et une stabilisation des fluctuations du plasma. La compréhension et le contrôle de tous les mécanismes impliqués dans la dynamique des plasmas par la modélisation théorique et numérique présentent un intérêt scientifique considérable, qui se traduira par des progrès significatifs pour l'humanité, comme la production d'énergie par fusion a confinement magnétique, ou des systèmes de propulsion spatiale.

2. Structures de l'espace des phases

Les structures de l'espace des phases sont des arrangements spécifiques de la distribution des particules de la densité de l'espace des phases. Elles sont connues dans divers contextes de turbulence du plasma, tels que le Bump-on-tail, les instabilités à deux faisceaux, sur des ondes acoustiques-ioniques, l'amortissement de Landau, les plasmas atmosphériques, la reconnexion magnétique ou les dispositifs a confinement magnétique.

2.1 Types de structures

Une variété de structures de l'espace des phases est décrite dans la littérature, notamment une structure de type vortex de fluctuation négative localisée de la densité de l'espace des phases, $\delta f < 0$, qui conduit à un fort piégeage local des particules, qui est appelé un trou de l'espace des phases. D'autres structures, appelées "bums" ou

"plateaux" de l'espace des phases, présentent respectivement une fluctuation positive de la densité de l'espace des phases $\delta f <> 0$ ou une fluctuation nulle de la densité de l'espace des phases $\delta f = 0$.

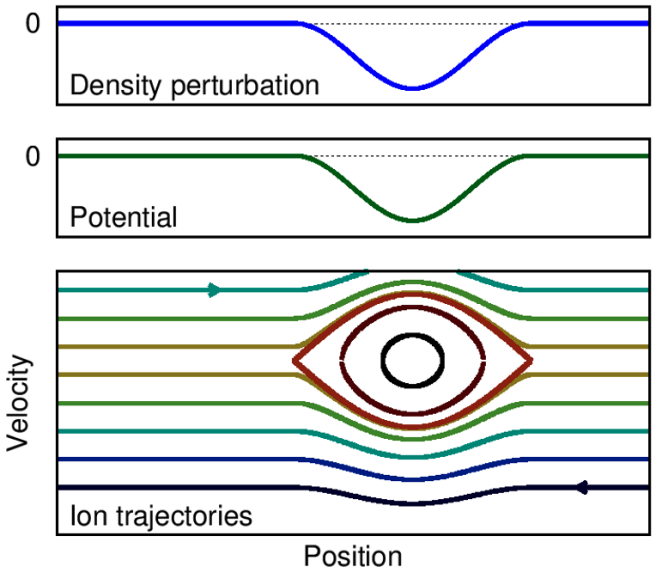

Figure 1: Schéma des différentes grandeurs électrostatiques pour un trou d'électron dans l'espace des phases. En bleu, la perturbation de la densité de charge, en noir, le champ électrique et en vert, le potentiel électrique. Enfin, l'espace des phases des trajectoires des électrons : orange pour les électrons libres, marron pour les électrons piégés et rouge pour la séparatrice.

Les trous de l'espace des phases sont le résultat d'un piégeage cinétique non linéaire localisé de particules par leur propre potentiel électrostatique ; la figure 1 montre la relation entre une structure de l'espaces des phases (dans ce cas, un trou d'électron), la densité et la perturbation du potentiel. Les trous de l'espace des phases ont été observés par simulation numérique [Roberts and Berk, 1967], puis analysés par la théorie [Bernstein et al., 1957; Schamel, 1971; Ghizzo, 1987], et observés dans divers plasmas stellaires et de laboratoire [Boström et al., 1988; Ergun et al., 1998; Khotyaintsev et al., 2010; Kamaletdinov et al., 2021].

2.2 Dynamique des structures

Des études ont permis d'observer que l'espaces des phases présente une dynamique riche et complexe : Les trous peuvent explorer l'espace-phase en accélérant et en décélérant, croître en taille et en profondeur, être dispersés ou détruits, et interagir

ou fusionner les uns avec les autres. Cependant, la dynamique des trous dans l'espace des phases est quantitativement et qualitativement peu connue, à l'exception du taux de croissance non linéaire d'un trou isolé [Boutros-Ghali and Dupree, 1982; Berman et al., 1985], et de l'interaction attractive entre différentes structures [Ghizzo et al., 1987].

Ce travail tente d'étudier quantitativement la dynamique des trous isolés dans l'espace des phases à l'aide de simulations cinétiques numériques et de la théorie analytique. En outre, un effort a été fait pour étudier les interactions binaires entre les structures de l'espace-phase dans le but de prédire la dynamique des structures impliquées.

3. Diffusion de particules charge dans des champs électriques

Dans un premier temps, nous avons étudié la diffusion de particules chargées dans un champ électrique turbulent unidimensionnel prescrit à l'aide de simulations numériques et de la théorie quasi-linéaire. Nous avons mesuré les coefficients de diffusion statistique à différentes valeurs du nombre de Kubo en utilisant un spectre d'amplitude Gaussienne et des relations de dispersion plasma réalistes : dispersions de Langmuir et ion-acoustiques. Et deuxièmement, nous avons étudié la diffusion de particules chargées dans un champ électrique de trou de Schamel unidimensionnel prescrit dans l'espace-phase au moyen d'une théorie analytique et de simulations numériques. Nous avons calculé analytiquement la diffusion générée par un trou dans l'espace-phase en supposant que le potentiel électrique a la forme d'une section décalée d'un oscillateur harmonique. Ensuite, nous avons mesuré les coefficients de diffusion statistique à différentes amplitudes du trou de l'espace-phase ϕ_0 et nous avons trouvé un accord qualitatif et quantitatif entre les simulations et la théorie.

En résume, nous avons fait une étude approfondie sur les coefficients de diffusion en dehors du régime quasi-linéaire, à de grands nombres de Kubo. Nous avons mesuré la diffusion évolue sous la forme d'une loi d'échelle de puissance, $K^3 \propto E^{3/2}$, que nous expliquons être une diffusion aléatoire des centres des trajectoires des particules piégées dans la direction de la vitesse. Également, nous avons réalisé une étude des coefficients de diffusion de particules chargées dans une superposition du trou de Schamel et de champs électriques turbulents? Ici nous avons mesuré la diffusion et observé deux régimes de dynamique des particules : Un premier, où la dynamique des particules est dominée par la structure de l'espace des phases, et un second où la turbulence domine la dynamique du plasma. Ces résultats sont affiche dans la figure 2

Finalement, nous avons étudie les processus d'accélération et de croissance des trous électroniques dans l'espace des phases. Nous avons mesuré les effets de la dis-

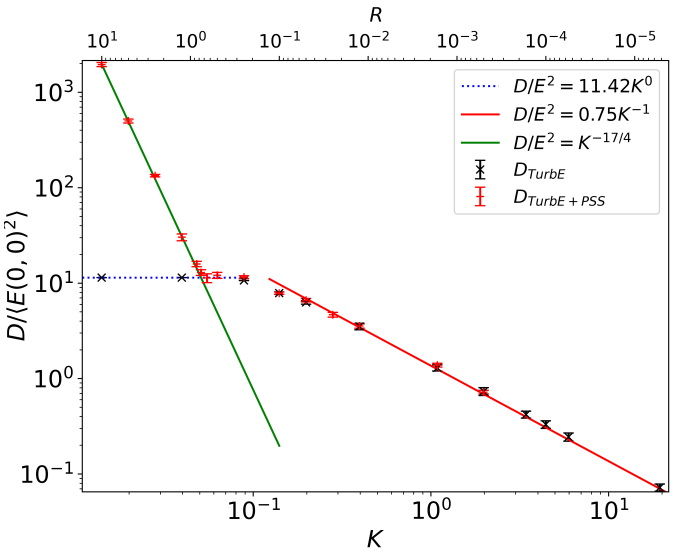

Figure 2: Coefficient de diffusion normalisé en fonction du champ électrique turbulent, nombre de Kubo K, et rapport entre l'amplitude du champ électrique caractéristique d'un électron-trou de Schamel et la turbulence R. Les croix noires se sont les simulations avec uniquement un champ turbulent, les croix rouges représentent la diffusion dans un champ turbulent avec trou de Schamel, les lignes bleues pointillées la théorie quasi lineaire, les lignes rouge le regime haut nombre de kubo, et la ligne verte la prédiction analytique d'un trou d'électron.

crétisation de l'espace des phases, qui se traduit par un opérateur collisionnel effectif qui accélère et lisse les trous de l'espace des phases. Nous avons observé des similitudes entre les dynamiques numériques et analytiques des trous. Cependant, des divergences entre les résultats numériques et analytiques ont été observées. En conclusion, nous avons montré les limites des théories analytiques dans la prédiction de la croissance des trous à l'aide de simulations numériques. En particulier, les effets marqués de la distribution ionique sur la dynamique d'un trou d'électrons. De plus, nous avons trouvé une approximation correcte de la croissance du trou pour prendre en compte les fortes déviations résultant de la variation des gradients de distribution sur la largeur du trou.